ATOMISTIC MODELLING OF MAGNETISATION REVERSAL PROCESSES IN RECORDING MEDIA

WEIJIA FAN

A Thesis submitted for the degree of Doctor of Philosophy

University of York

PHYSICS

SEPTEMBER 2013

Abstract

Magnetic materials used in the magnetic recording industry have been developed for several decades. However, since the areal recording desity is increased to around 1 $Tbit/in^2$, some new physical challenges have become clear: particularly the need of using high magnetic anisotropy materials to overcome the superparamagnetic effect. The requirement of acceptable signal to noise ratio leads to a reduction in grain size. In order to maintain thermal stability it is necessary to increase the magnetic anisotropy K. This leads to unrealistically high write fields. The main challenge is to reduce the write field, which is being met by advanced design and the potential use of Heat Assisted Magnetic Recording. In the meantime, the research on the reversal processes has also attracted much attention because of the use of ultra-fast technology and also the high speed of writing and reading processes in recording media. From the theoretical point of view, an atomistic model can obtain detailed information which is difficult to obtain from experiments. Also it can break through the limitation of micromagnetic calculations in ultra-fast processes and thermal effects because of using a Heisenberg direct exchange model and at the atomic level, especially studying the interface between two coupled materials. In this thesis, an atomistic model is used to simulate the properties of magnetic recording media studying the reversal processes, as well as the exchange coupling, anisotropy and thermal effects of small magnetic particles. First of all, the inter-granular exchange coupling is calculated by doping magnetic atoms into the spacing between magnetic recording grains, and indirectly by adding a capping layer onto the granular recording layer, to control the exchange coupling and further the switching field of the magnetic media. This result shows that an optimised interface exchange parameter is important to reduce the coercivity. Secondly, the reversal processes of many independent single domain particles is studied, determining several important parameters such as field, temperature and time scale, to better understand some critical physical problems in the heat assisted magnetic recording process. Furthermore, a larger scale atomistic model is used to simulate the whole heat assisted magnetic recording process in a granular recording media with grain size distribution, demonstrating the full atomistic model is capable to simulate a realistic system. Finally, an exchange coupled composite media is simulated to develop the potential application of this material in recording media.

Table of Contents

Table of Contents 3

1. Introduction 12
- 1.1 Origin of Magnetism 12
- 1.2 Properties of Ferromagnetic Materials 14
  - 1.2.1 Hysteresis Loop 14
  - 1.2.2 Magnetic Anisotropy 15
  - 1.2.3 Exchange Interaction 16
  - 1.2.4 Temperature Dependence 17
  - 1.2.5 Single Domain Particles 17
- 1.3 Research Motivation 18
- 1.4 Thesis Outline 19

2. Atomistic Modelling Methods 21
- 2.1 Heisenberg Exchange Model 21
- 2.2 Spin Dynamics 22
- 2.3 Spin Hamiltonian 24
  - 2.3.1 Exchange Coupling 24
  - 2.3.2 Magnetocrystalline Anisotropy 25
  - 2.3.3 Applied Field Term 26
  - 2.3.4 Dipolar Term 27
  - 2.3.5 Thermal Field 27
- 2.4 Hamiltonian of $L1_0$ FePt 29
- 2.5 Hamiltonian of CoPt 30
- 2.6 Integration Solution 31
- 2.7 Conclusion 31

3. Control of the Exchange Coupling in Granular CoPt Magnetic Recording Media 32
- 3.1 Control of the exchange coupling in CoPt/Co Bilayers 32
  - 3.1.1 Introduction 32
  - 3.1.2 Reversal Processes 34
  - 3.1.3 Control of the Exchange Coupling 37
  - 3.1.4 Conclusion 41
- 3.2 Study of the Direct Intergranular Exchange Coupling 41
  - 3.2.1 Monte Carlo Calculation of Exchange Coupling Between two ferromagnetic grains 41
  - 3.2.2 Atomistic modelling of CoPt grains with doping magnetic atoms in the intergranular layer 46
  - 3.2.3 summary 51
- 3.3 Conclusion 51

4. Atomistic Modelling of Ultrafast Field Cooling Processes of Magnetic Recording Media . . . 52
- 4.1 Introduction . . . 52
- 4.2 Ultrafast field cooling processes of a heat assisted magnetic recording medium . . . 53
  - 4.2.1 Applied Field . . . 56
  - 4.2.2 Cooling Rate . . . 59
  - 4.2.3 Peak Temperature . . . 61
  - 4.2.4 Grain Size . . . 64
  - 4.2.5 Angular Dependent Reversal Probability . . . 65
  - 4.2.6 Semi-analytical Model . . . 66
- 4.3 Full HAMR process on a realistic granular recording media . . . 68
- 4.4 Conclusion . . . 69

5. Heat Assisted Magnetic Recording Processes of Exchange Coupled Composite Media . . . 72
- 5.1 Introduction . . . 72
- 5.2 Reversal Processes of an ECC FePt/Fe Bilayer . . . 73
  - 5.2.1 Interface Exchange Constant Dependent Switching Field of FePt/Fe bilayers . . . 73
  - 5.2.2 Free Energy Calculated by Constrained Monte Carlo Method 81
  - 5.2.3 Effect of the Thickness of Soft Layer in ECC Bilayers . . . 82
  - 5.2.4 Room Temperature . . . 87
- 5.3 Temperature Dependent Reversal Probability in a HAMR process of ECC media . . . 92
  - 5.3.1 Cooling Rate Dependent Reversal Probability . . . 92
  - 5.3.2 Effect of Interface Exchange Coupling and the thickness of soft layer on the Reversal Probability . . . 94
- 5.4 Conclusion . . . 95

6. Conclusions . . . 97

References . . . 102

List of Figures

1.1 Sketches of different types of magnetism. 13

1.2 Hysteresis loop of a typical ferromagnetic material: magnetisation (M) as a function of applied field (H). 15

1.3 Bethe-Slater curve[4]: the exchange paramter as a function of the ratio of interatomic distance over the radius of 3d electron shells. The element with a positve exchange parameter is ferromagentic and a negative exchange parameter refers to antiferromagnetic. . . 17

2.1 (a):Spin precession around the effective field, $-\mathbf{S} \times \mathbf{H}_{\text{eff}}$ is perpendicular to the $\mathbf{S} - \mathbf{H}$ plane. (b): Spin relaxation, $-\mathbf{S} \times (\mathbf{S} \times \mathbf{H}_{\text{eff}})$ points from $\mathbf{S}$ to $\mathbf{H}$. 22

2.2 Pre-factors in Eq. 2.2, $\mathbf{f}_1 = \gamma/(1+\alpha^2)$ and $\mathbf{f}_2 = \alpha\gamma/(1+\alpha^2)$, as a function of damping constant α. 23

2.3 Spin relaxation at different damping constant 24

2.4 Hysteresis loops of a single spin with different K_u values at zero Kelvin. An external field is applied along the direction of the magnetocrystalline anisotropy, which is the easy axis. The applied field and magnetization are both normalized. 25

2.5 Sketch of energy barrier without (a) and with an applied field (b) . 26

2.6 Temperature dependent magnetization dynamics in x-y plane. . . . 28

2.7 Temperature dependent magnetization of a single FePt grain, grainsize=5 nm. 29

2.8 (a): schematic diagram of an $L1_0$ FePt unit cell. Fe atoms (red) locate on 8 corners and centres of top and bottom faces. Pt atoms (blue) are on the middle level. (b): schematic diagram of an effective spin model of FePt, using uniform FePt atoms over all the FCT sites. 30

3.1 The schematic diagram of the CoPt grains coupled with a continuous Co layer. The "larger system" in this chapter means the CoPt grains are hexagonal columns with 5 nm diagonal in the hexagonal plane and 5 nm thickness; the spacer between the grains is 1 nm. The "smaller system" refers to the 3 nm diagonal and 5 nm thickness CoPt grains, and the spacer is 0.5 nm. 33

3.2 Hysteresis loops of CoPt/Co bilayers for different grain sizes. Fig. 3.2(a) shows the hysteresis loops of both coupled (black) and non-coupled (red) system with 5 nm grain size and 1 nm spacer. Fig. 3.2(b) presents the hysteresis loops of both coupled (black) and non-coupled (red) system with 3 nm grain size and 0.5 nm spacer. . 35

3.3 Reversal processes of CoPt/Co bilayers, grain size=3 nm, with no interface interaction. 36

3.4 Reversal processes of CoPt/Co bilayers, grain size=3 nm, with an interface interaction of Jij=2.2e-21 Joules. 38

3.5 Coercivity at Room Temperature as a function of interfacial exchange coupling constant Jij, for grain size of 5 nm (black) and 3 nm (red) . 39

3.6 Coercivity at Room Temperature as a function of the number of Co monolayers, for different interfacial exchange coupling constants. . 40

3.7 Visualization figure of two cubic ferromagnetic grains coupled by doping ferromagnetic atoms in the spacer. All the spins in Magnetic layer 1 are constrained to the +z direction. Magnetic layer 2 is constrained at the direction with an angle $\theta = 0^\circ$ to 180° from the +z direction. The doping atoms are randomly added into the spacer between the two layers, and the density of the doping atoms can be varied from 0% to 100%. 42

3.8 Restoring Torque as a function of the constrained angle of Magnetic layer 2 in Fig. 3.7, for different density of the doping atoms between two layers. 43

3.9 Exchange energy as a function of the number of the monolayer of the spacer between Magnetic Layer 1 and Magnetic Layer 2 in Fig. 3.7, the curves in different colours referring to varying density from 10% to 100% of the doping atoms within the spacer. 44

3.10 Exchange energy as a function of temperature, for different number of monolayers of the spacer, varying from 1 to 6 monolayers. 45

3.11 The schematic diagram of the CoPt grains with doping magnetic atoms in the spacer. 47

3.12 Coercivity at Zero Temperature as a function of the density of the doping atoms in the spacer between grains, for different magnetocrystalline anisotropy constants. 47

3.13 Hysteresis Loops for different density and anisotropy of the doping atoms. (a): $K_\mathrm{u} = 0$; (b): $K_\mathrm{u} = 2.322 \times 10^{-23}$ Joules 49

3.14 Coercivity at Room Temperature (300 Kelvin) as a function of the density of the doping atoms in the spacer between grains, for different magnetocrystalline anisotropy constants of the doping atoms. 50

4.1 Hysteresis loops of a single grain at three different temperatures: 0 K (black), 300 K (blue) and 650 K (red). 54
4.2 The temperature dependent magnetisation M and magnetocrystalline anisotropy K of a 5nm single grain. Points: simulations results; Dashed lines: fitting curves 54
4.3 Visualisation of the whole system. 55
4.4 Temperature performance for different cooling rates, according to Eq. 4.4. 56
4.5 The time dependent z component of the magnetisation with fixed $\tau = 100ps$, varying H_{app}, for different peak temperatures: 630K (a), 660K (b), and 800K (c). 57
4.6 The time dependent z component of the magnetisation with fixed $H_{applied} = 0.8T$, varying τ, for different peak temperatures. 60
4.7 The time dependent z component of the magnetisation with fixed $H_{applied} = 0.8T$, varying T_{max}, for different cooling times: (a) $\tau = 10ps$; (b) $\tau = 100ps$; (c) $\tau = 500ps$. 62
4.8 Reversal time for grains when the temperature is kept at peak temperature 630 K, under varied applied fields. 63
4.9 Reversal time for grains when the temperature is kept at peak temperature 660 K, under varied applied fields. 64
4.10 Probability of reversal as a function of the diameter of the grains. $\tau = 100ps$, $H_{applied} = 0.8T$. 65
4.11 Probability of reversal as a function of the angle between applied field and the easy axis, for different peak temperatures.$\tau = 100ps$ $H_{applied} = 0.8T$. 66
4.12 Probability of reversal after equilibration as a function of applied field, for different cooling times. 67
4.13 Sketch of the magnetic field and laser areas in a hamr head: the blue square is the uniform magnetic field area, and the read round is the laser heating area. 68
4.14 Visualisation of a full HAMR processes to a realistic granular recording medium 70

5.1 Interface exchange constant dependent coercivity of a 5nm FePt layer coupled with 1 nm Fe layer at zero temperature. 73

5.2 Hysteresis loops of a 5nm FePt coupled with 1 nm Fe bilayers at zero temperature.J_{int}=0 (black line), 5% (red line), and 100% (blue line) of J_H . . . 74
5.3 Angle between the magnetic moment and easy axis of the hard layers (the solid lines) and the soft layers (the dashed lines). J_{int}=0 (black line), 5% (red line), and 100% (blue line) of J_H . . . 75
5.4 Layer resolved magnetisation of the FePt/Fe bilayers:$J_{int} = 0$ . . . 76
5.5 Layer resolved magnetisation of the FePt/Fe bilayers:$J_{int} = 5\% J_H$. 77
5.6 Layer resolved magnetisation of the FePt/Fe bilayers:$J_{int} = 100\% J_H$ 78
5.7 Layer resolved magnetisation reversal of the 5nm FePt coupled with 1nm Fe: $J_{int} = 0\% J_H$ . . . 79
5.8 Layer resolved magnetisation reversal of the 5nm FePt coupled with 1nm Fe: $J_{int} = 5\% J_H$ . . . 80
5.9 Layer resolved magnetisation reversal of the 5nm FePt coupled with 1nm Fe: $J_{int} = 100\% J_H$ . . . 80
5.10 The free energy of 5 nm FePt coupled with 1 nm Fe: the interface exchange coupling is $J_{int} = 100\% J_H$. . . . 82
5.11 The gradient free energy of 5 nm FePt coupled with 1 nm Fe: the interface exchange coupling is $J_{int} = 100\% J_H$. . . . 83
5.12 The coercivity of 5 nm FePt/2 nm Fe bilayers as a function of the interface exchange coupling J_{int}. . . . 83
5.13 The hysteresis loops of 5 nm FePt/2 nm Fe bilayers with different interface exchange coupling J_{int}. . . . 84
5.14 The coercivity of 5 nm FePt/3 nm Fe bilayers as a function of the interface exchange coupling J_{int}. . . . 85
5.15 The hysteresis loops of 5 nm FePt/3 nm Fe bilayers with different interface exchange coupling J_{int}. . . . 86
5.16 The coercivity of FePt/Fe bilayers as a function of the thickness of Fe layer. . . . 88
5.17 The hysteresis loops of FePt/Fe bilayers for different thickness of Fe layer. . . . 88
5.18 Interface exchange constant dependent coercivity of a 5nm FePt coupled with 1 nm Fe bilayers at room temperature. . . . 89
5.19 Hysteresis loops of a 5nm FePt coupled with 1 nm Fe bilayers at room temperature.J_{int}=0 (black line), 5% (red line), and 100% (blue line) of J_H . . . 90
5.20 The coercivity of FePt/Fe bilayers as a function of the thickness of Fe layer at room temperature. . . . 91

5.21 The coercivity of FePt/Fe bilayers as a function of the thickness of Fe layer at room temperature, $J_{int} = 100\% J_H$. 91
5.22 Time dependent temperature: the peak temperature $T_{max} = 420K$, the cooling time $\tau = 100ps$. 93
5.23 5 nm FePt/2 nm Fe ECC structured recording media: temperature dependent reversal probability at different cooling time. 94
5.24 5 nm FePt/5 nm Fe ECC structured recording media: temperature dependent reversal probability at different cooling time. 95

Acknowledgement

I would like to take this opportunity to thank as many people as possible who have supported me for the research I have done during the past four years.

First of all, I would like to express my gratitude to my supervisor, Professor Roy Chantrell, who is an intelligent scientist and and also a kind advisor. From him I did not only study the mysteries of physics world but also enjoyed collaborating with many people. Without his enlightening and supervising, I could not finish this work. Without his encouraging and supporting, I could not go to so many conferences, workshops, summer schools, to present my work and communicate with other scientists. It is more than honoured and grateful to be his student and work with him.

I also would like to thank another mentor, Dr Richard Evans, who is very generous to teach me all the details about computer programming, physics problems and even article writing. Because of his patience and kindness, I succeeded to transfer from experimental to theoretical researching. His willingness and attitude to do research and designing of life as a physicist is a good example for me to follow.

In addition, I will mention a co-worker and my best friend in York, Phanwadee Chureemart. We spent a lot of good time together in York and will continue this precious friendship to make our life better. I also have to thank other co-workers in York: Jerome Jackson, Tom Ostler, Joe Barker, Cecilia Aas, Ondrej Hovorka, Ramon Cuadrado, for their helpful discussion and assistance in researching, and two summer students, Simon Devos, Quentin Coopman for the pleasure collaboration. Three more people from Seagate Technology, Kaizhong Gao, Gangping Ju, and Xi Chen, are also appreciated for the delighted collaboration.

I would like to thank my parents, for everything, and my husband Lei, accompanying with whom my life becomes so nice. Last but not the least, I want to mention my daughter, who is not born yet, but stays with me and gives me huge courage to finish this thesis.

Finally, I would like to say, it is one of the best choices I have ever made to come to York, doing research and meeting so many nice people. The past four years is a wonderful and remarkable period of time in my life.

Declaration

Hereby I declare this thesis submitted for the Philosophy Doctor degree at University of York is my own work, excepting the previous acknowledged contribution. The following lists specific research which was done in collaboration with others, but is presented as part of the thesis for clarity and completeness.

The constrained Monte Carlo simulation of the direct exchange coupling between two FePt particles was done in collaboration with Richard Evans, Simon Devos and Quentin Coopman. The Free energy of the exchange coupled composite bilayers calculated by constrained Monte Carlo method is performed by Richard Evans.

The rest main part of the thesis is done by the author herself and most of the work has been presented at many meetings and conferences, and the work in Chapter 3 Section 3.1 has been published at Journal of Applied Physics 109, 07B752 (2011) [1].

1. Introduction

Magnetism is an important property of nature, and it has been deeply studied and widely applied for dozens of centuries since it was first recorded by ancient Greek philosopher Aristotle in 600 BC [2]. In 1819 Oersted found that an electric current could effect a compass needle [3], which started an understanding of the relationship between electricity and magnetism. Later, magnetism applied mostly in electric and magnetic motors. However, nowadays, magnetic materials are attracting more attention because of application in digital information storage, such as hard disks. In this chapter, the origin of magnetism will be introduced, discussing the circular current model of electrons in atoms and also the concept of spin. Furthermore, the exchange, the anisotropy and other magnetic properties are discussed. Additionally, ferromagnetism, especially the perpendicular magnetic materials will be considered because of their important properties and applications.

1.1 Origin of Magnetism

Magnetism has been studied and used for thousands of years, since people first discovered the attraction and repulsion between magnetic materials, with the aim to understand the origin of magnetism [4]. For the atomic magnetism, there are two sources of magnetism: the orbital angular motion of electrons around nuclei, and the intrinsic spin moment. The magnetisation is defined as the sum of all the spin moments. For materials, how the magnetic or spin moments interact with each other depends on the coupling between atomic spins. Therefore, materials have different magnetic properties, which can be classified in the following types [5]: diamagnetism, paramagnetism, ferromagnetism, antiferromagnetism, ferrimagnetism. Diamagnetism appears in all materials, and is characterised by the tendency to align opposite to an applied magnetic field. For materials having uncompensated orbital and spin angular momentums, if these atomic moments are independent of each other, or the interaction is very weak, such materials exhibit paramagnetism as shown in Fig. 1.1(a). Such materials do not have a magnetisation in the absence of an applied magnetic field, but when the field is on, all the spin moments have the tendency to align in the same direction as the field. If the intra-atom interaction is strong, the material can be ferromagnetic, antiferromagnetic, or ferrimagnetic, which depends on the interaction coefficient. If the interaction parameter is positive, all the spin moments align in parallel to lower the energy and the material is ferromagnetic, as shown in Fig. 1.1(b). Ferromagnetic materials usually have strong spontaneous magnetisation in the absence of an applied field. It also has many other interesting properties which will be discussed in the following section.

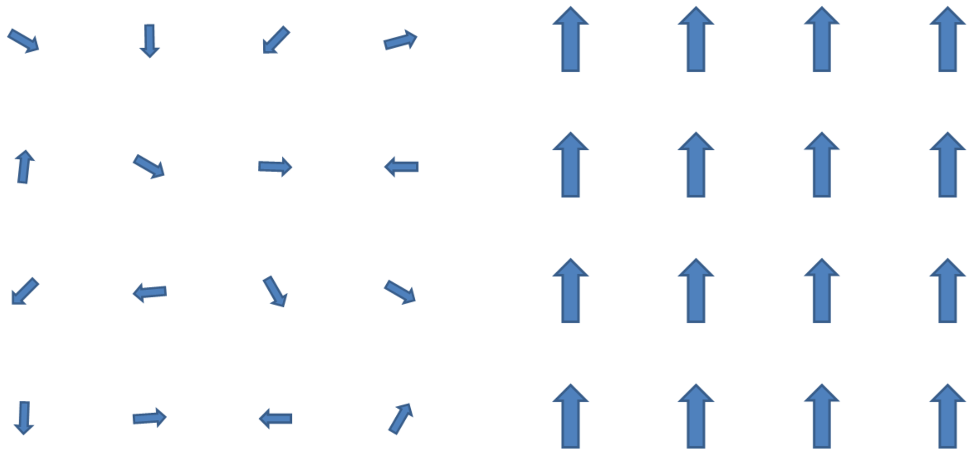

(a) paramagnetism (b) ferromagnetism

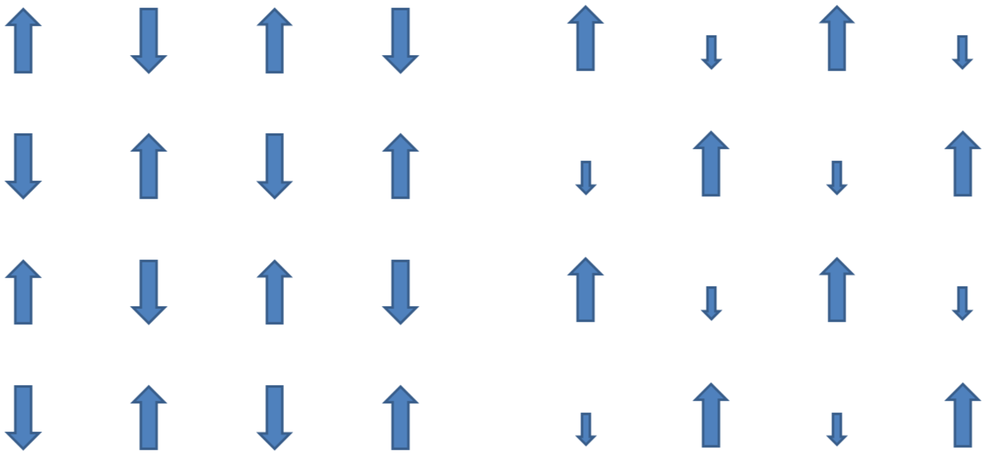

(c) antiferromagnetism (d) ferrimagnetism

Figure. 1.1: Sketches of different types of magnetism.

If the interaction constant is negative, the spin moments would like to align anti-parallel to maintain the lowered-energy state, which is called antiferromagnetism shown in Fig. 1.1(c). Antiferromagntic materials do not have net magnetisation except in a large applied field. If the interaction is negative but the net magnetic moment is not zero, this is called ferrimagnetism, shown in Fig. 1.1(d). From the magnetisation point of view, ferrimagnetic materials are like ferromagnetic materials because both of them have strong spontaneous magnetisation without an applied field. However, from the origination of the magnetic property, ferrimagnetism is more like antiferromagnetism, because the interaction parameter is negative and the spin moments tend to align anti-parallel to each other. In some rare-earth transition-metal alloys, such as GdFeCo[6, 7], the magnetisation can be described by two-sublattice model. In GdFeCo, Gd-Gd interaction and FeCo-FeCo interaction are positive, but the Gd-FeCo interaction is negative. Therefore, the rare-earth Gd atoms are aligning parallel and the transition-metal FeCo atoms are also parallel aligned. These two sublattice are antiparallel to each other, so the GdFeCo alloy has a ferrimagnetic spin configuration.

1.2 Properties of Ferromagnetic Materials

1.2.1 Hysteresis Loop

Ferromagnetism typically appears in Iron, Cobalt, Nickel and their alloys, also in some rare earth metals. Ferromagnetic materials have several properties in common: high saturation magnetisation, Curie Temperature, hysteresis and magnetic anisotropy [8]. Fig. 4.1 shows a typical hysteresis loop of a ferromagnetic material. Y-axis indicates the magnetisation of the ferromagnetic materials, and the X-axis is the applied external field. This M-H curve presents how the magnetisation is reacting to a varied applied field. Generally, the applied field is started from the positive maximum value, and then is reduced to zero and increased in the opposite direction to the negative maximum. Then the field is recovered to complete the whole loop. Hysteresis means the reaction of magnetisation of a ferromagnetic material is always slower than the applied field. There are several critical parameters in a hysteresis loop. M_s is the saturation magnetisation which is the maximum of the magnetisation, mainly depended on the number of magnetic moments of the measured sample, M_r is the remanence which is the value of magnetisation when the applied field is reduced to zero, and H_C is the coercivity which is the field required to reduce the magnetisation back to zero after it has been pulled to saturation by the applied field, H_C is mainly effected by the magnetic anisotropy. The hysteresis loop describes many important magnetic properties, as well as some magnetic dynamics processes, therefore it is the basic magnetic curve studied during the researching of magnetic materials. In ferromagnetic materials, the hysteresis is effected by the rotation of magnetisation and the changes in size or number of magnetic domains. In a single domain particle, the magnetisation rotates in response to the applied field. Large magnetic particles are devided into small domains which are magnetised in different directions. Between the domians there are domain walls, within which the direction of magnetisation rotates from one domain to another domain. The magnetisation within a domain does not change, but the wall moves corresponding to the applied field, and this can relatively change the domain size.

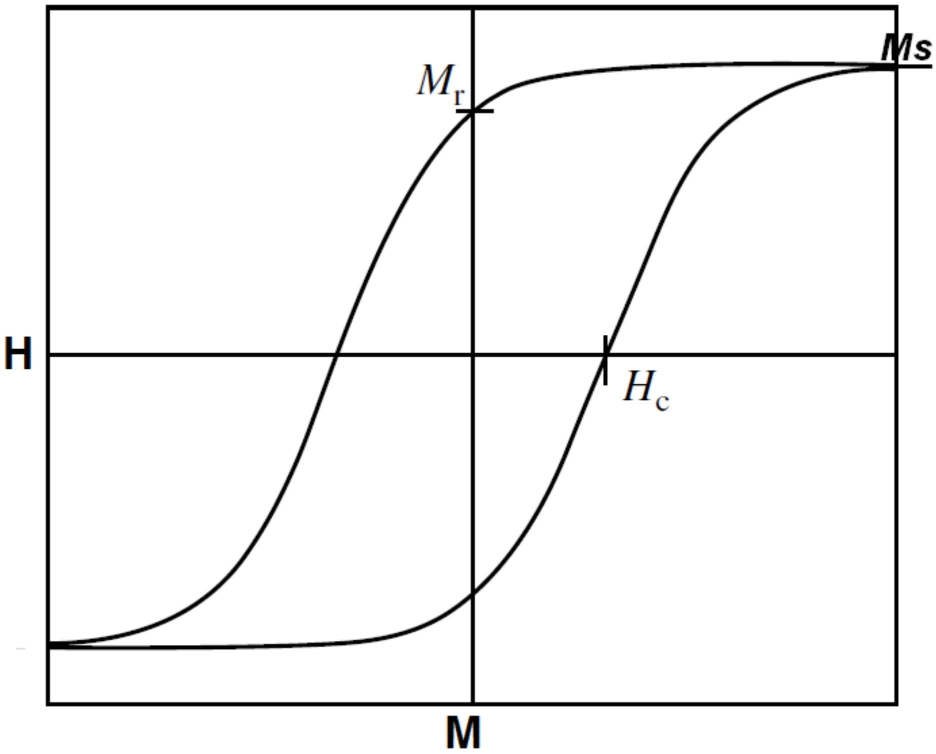

Figure. 1.2: Hysteresis loop of a typical ferromagnetic material: magnetisation (M) as a function of applied field (H).

1.2.2 *Magnetic Anisotropy*

The coercivity is mainly depending on the anisotropy, based upon which the ferromagnetic materials can be distinguished into soft and hard magnetic materials. Soft ferrromagnetic materials are used in transformers, inductor cores and microwave devices because of their low coercivity. Hard materials are more widely used in magnetic recording media due to their large coercivities. The magnetic anisotropy is a directional dependence of a ferromagnetic material, along which the magnetic moments tend to align, also called easy axis. There are several sources of the magnetic anisotropy: magnetocrystalline anisotropy, shape anisotropy, exchange anisotropy, surface anisotropy and anisotropy created by the magnetoelasticity. For a hard magnetic material, magnetocrystalline anisotropy gives the most contribution to the total anisotropy.

The magnetocrystalline anisotropy involves crystal-field interaction and spin-orbit coupling. The crystal-field interaction originates from the effect of a magnetic ion from the electric field of the surrounding neighbouring ions in a crystal. Because the crystal structure is not spherically symmetric, the electric field generated by the surrounding neighbouring ions is not spherically symmetric, either. This type of electric field is called crystal field, because of which the energy has a minimum only when the uncoupled electrons occupy specific positions. Therefore the magnetisation is anisotropic depending on different orientations through spin-orbit coupling. Spin-orbit coupling is the dipole interaction between the spin of an electron and the magnetic field generated by the electron's orbit motion. For 3d magnets, the orbital moments are largely quenched, and spin-orbit coupling gives a small distribution to the leading crystal-field. In rare-earth materials, the orbital moments are usually unquenched, and 4f charge cloud is strongly coupled with the spin. Heavy transition-metal atoms combine strong crystal-field interaction and are intermediate between 3d and 4f atoms.

In ferromagnets, lowest-order or second-order uniaxial anisotropy is usually used to describe the phenomenological anisotropy. For uniaxial anisotropy, the anisotropy energy density is defined as following:

$$\frac{E_a}{V} = K_1 sin^2\theta + K_2 sin^4\theta + K_3 sin^6\theta \tag{1.1}$$

Where E_a is the anisotropy energy and V is the volume of the magnet. θ is the angle between magnetisation and the symmetry axis. K_1 is the lowest-order uniaxial anisotropy constant, and K_2 and K_3 are the second-order and third-order uniaxial anisotropy constants, respectively. The first, or the lowest-order term describes the anisotropy energy has minimum value along the symmetric axis, and maximum if perpendicular to the axis. This axis is called easy axis in ferromagnets.

1.2.3 Exchange Interaction

The origins of the exchange interaction is a quantum mechanical effect, depended on the overlap of the wave functions of electrons. Due to Pauli principle, the grand-state spin structure is ↑↓. The exchange constant J is defined as half the energy difference between ↑↓ and ↑↑ states. This is depended on the distance of two electrons from different atoms and the number of electrons of each atom. Fig. 1.3 shows the exchange parameter as a function of the ratio of interatomic distance over the radius of 3d electron shell[4]. It summarised some materials such as Fe, Co and Ni are ferromagnetic, and some others such as Mn are antiferromagnetic. The alloys of Fe, Co and Ni are also ferromagnetic. In ferromagnetic materials, the exchange interaction parameter is positive. In order to achieve a lowest energy state, the atomic spins in a ferromagnet are aligned parallel to each other, as shown in Fig. 1.1(b). In this thesis, a Heisenberg direct exchange model is used, which only considers the short range exchange–the

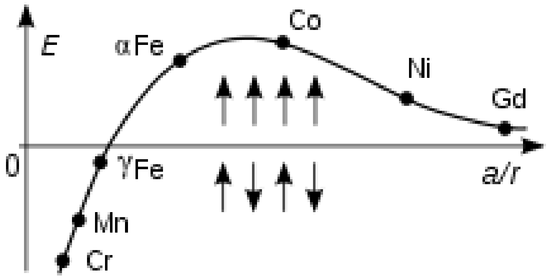

Figure. 1.3: Bethe-Slater curve[4]: the exchange paramter as a function of the ratio of interatomic distance over the radius of 3d electron shells. The element with a positve exchange parameter is ferromagentic and a negative exchange parameter refers to antiferromagnetic.

exchange between nearest neighbours.

1.2.4 Temperature Dependence

At zero temperature, all the atomic magnetic moments are aligned in the easy axis and thus form the spontaneous magnetisation. When the temperature is increasing, the atomic magnetic moments will become increasingly disordered because of the thermal fluctuations and thus the total magnetisation is reduced. When the temperature reaches a certain point, the magnetisation approaches zero. This critical temperature point is defined as the Curie Temperature. Curie Temperature is mainly depending on the intrinsic exchange coupling of ferromagnetic materials. The thermal fluctuations do not only effect on the magnetisation, but also reduce the magnetic anisotropy. Therefore, the coercivity is decreased when the temperature is increasing.

1.2.5 Single Domain Particles

Large magnetic materials can be broken into small domains because of the magnetostatic energy, which is also called de-magnetising energy. This de-magnetising field is the field which always tries to opposite the magnetisation in a magnetic particle. In each domain, the magnetic moments all align in the same direction while the magnetisation of each domain has different easy axis from each other and there are domain walls between the domains. Domain walls can be distinguished into two types according to the way how magnetisation changes within the wall: Bloch wall, over which the magnetisation is parallel to the domain wall when changes from one domain to the next one; and Neel wall, over which the magnetisation rotates within the plane of the domain wall. The energy of the domain wall involves exchange energy and anisotropy energy in the wall. However, when the magnetic material size is small, it can not support domains structure because of the domain walls energy. Such particles are called single domain particles, which have high anisotropy and saturated magnetisation. The critical size of a single domain particle is determined by the competition between the magnetostatic energy which is depending on the saturation magnetisation and the domain wall energy. Single domain particles are ideal materials for magnetic recording media because of their high thermal stability.

1.3 Research Motivation

One of the important applications of magnetic materials is magnetic recording, which has been developed and attracted much attention for many years. However, there are still several crucial physical problems unsolved. The first one is the so-called trilemma in magnetic recording media: readability, writeability and stability[9]. The coercivity of the single domain particles used as magnetic recording media is as high as 2-3 Tesla, which is beyond the magnetic field of the existing magnetic heads. Therefore, to reduce the switching field of the recording material is a major aim. Additionally, the magnetic moments can random flip the direction if the magnetic particle is small enough due to the thermal fluctuations. The time between two random flips is caused by the thermal fluctuations, according to the Nel-Arrhenius equation:

$$\tau_N = \tau_0 \exp(\frac{KV}{k_B T}) \tag{1.2}$$

where τ_N is the time between two flips, τ_0 is the attempt time which depends on the material but is often taken as $10^{-11}\ s$, K is the magnetic anisotropy and V is the particle volume, k_B is the Boltzmann constant and T is the temperature in Kelvin. In order to keep the written information thermally stable up to 10 years time, KV/k_BT must be at least 60 which requires a high anisotropy. Meanwhile, another important aim is to increase the recording density which requires smaller particle size. It is a huge challenge to research the competition between these problems. Moreover, the critical physics behind these problems is still unclear and worthy of study.

From the point view of theoretical research, there are many works on recording media by using micromagnetic calculation. However, this method has its limitations in simulating the small mesh size of nanoparticles, ultrafast spin dynamics process and thermal effects. Therefore, in this thesis, an atomistic method is used, based on the Heisenberg exchange model and Landau-Lifshitz-Gilbert (LLG) equation. By using this method, the dynamics of each atomic spin moment can be calculated according to an atomic level LLG equation. The time scale can also be reduced as short as 10^{-16}s, so some ultrafast reversal processes can be observed at femtosecond level. The interaction between atoms is calculated by the Heisenberg exchange model, thus many complex crystal structures can be modeled rather than only simple cubic crystal. In the meanwhile, the interface interaction can also been considered into the simulation, which is a large advantage that micromagnetic calculation is lack of. Direct physical parameters gained from ab-initio calculation can also be used in the atomic model to get a more accurate and reasonable result. Furthermore, thermal effects are also taken into account by using Langevin dynamics, assuming an effective thermal field into the LLG equation. More importantly, time dependent temperature effect can be taken account into the calculation, thus an accurate temperture dependence of magnetic properties can be investigated in this atomistic model.

1.4 Thesis Outline

In the following chapters, first of all, Chapter 2 will introduce the detailed method of atomistic modelling, including the method to integrate the LLG equation, the spin Hamiltonian including exchange, anisotropy, applied field, and thermal effect. The Hamiltonian of the materials used as recording media is also discussed later. Following this, we use the atomistic model to calculate the dynamics of magnetic recording media, focusing on the exchange coupling, the heat assisted magnetic recording process and exchange coupled composite media.

In a recording media, since the grain size is reduced to very small and so is the spacer between the grains, the exchange coupling between the small grains cannot be neglected. In fact, exchange coupling is important in the design of magnetic media, since it can compensate to some extent for the effects of the demagnetising field. Chapter 3 studies the exchange coupling in granular CoPt recording media, both the indirect exchange coupling between the CoPt grains and a capping Co layer, and the direct exchange coupling between the CoPt grains via intermixing CoPt atoms among the spacer between grains.

Chapter 4 describes the heat assisted magnetic recording (HAMR) process of FePt grains which aims to solve the trilemma in a recording media by lowing the coercivity by laser heating. We focus on the field cooling process, to study several critical factors effecting the reversal process: the temperature, the cooling time, the applied field, and the grain size.

Chapter 5 is about the reversal processes of exchange coupled composite FePt/Fe bilayers, as well as a heat assisted magnetic recording process on the exchange coupled composite bilayers.

Finally a conclusion is given, summarising the research results and physics we studied through the thesis.

2. Atomistic Modelling Methods

In the previous chapter, we outlined the origin of magnetism and the basic properties of magnetic materials, as well as the application and aim of magnetic films with perpendicular anisotropy. This chapter will discuss the detailed modelling methods, including mathematical and computational methods.

In order to better understand the detailed magnetic properties and behaviour of magnetic materials which have present or potential application in data storage industry, a frame of atomistic magnetic modelling has been developed and is advancing rapidly due to improved methodology and improved computational power. In the last couple of decades, micromagnetic simulation has given a general frame of magnetic dynamics [10]. However, the micromagnetic method has several limitations originating in its phenomenological assumption of a continuum vector magnetic field, as well as limiting the resolution to a lengthscale of several nm: much longer than the lattice spacing. As a result, the exchange energy cannot be calculated exactly, and a continuum approximation is applied. An atomistic spin model can overcome these limitations by treating the spin moments in magnetic solids, so as to give the detailed magnetic properties and to be able to simulate ultrafast spin dynamics, with finite temperature and complicated spin structures such as antiferromagnet and spin glass.

2.1 Heisenberg Exchange Model

The basic background of atomistic modelling is assumption of one spin on each crystal atom site. The exchange coupling between spins is taken into account by using a Heisenberg exchange model [11], which takes into account the direct exchange interaction between one spin and its nearest neighbouring spins. The Heisenberg model is derived from the Heitler-London quantum theory [12] calculating the total energy of two interacting electrons on neighbouring atom sites. The Heitler-London approach assumes the wave function of two electrons can be obtained by a linear combination of the wave functions of the two electrons, respectively. Heisenberg took this approximation and applied to two interacting atomic spins on neighbouring sites in a solid. The Heisenberg Hamiltonian of two interacting spins has the following form:

$$\mathcal{H}_{Heisenberg} = -2J_{ij}\mathbf{S}_i \cdot \mathbf{S}_j \tag{2.1}$$

Where J_{ij} is the Heisenberg exchange constant between a spin i and its nearest neighbouring spin j. S_i and S_j are the spin moments of the spins i and j. The exchange constant J_{ij} is mainly depending on the distance between atoms.

2.2 Spin Dynamics

The spin dynamic is described by the Landau-Lifshitz-Gilbert equation [13, 14], which takes the form:

$$\frac{\partial \mathbf{S}}{\partial t} = -\frac{\gamma}{(1+\alpha^2)}[\mathbf{S} \times \mathbf{H}_{\text{eff}} + \alpha \mathbf{S} \times (\mathbf{S} \times \mathbf{H}_{\text{eff}})] \tag{2.2}$$

Where $\mathbf{S}$ is the normalised spin moment of an atom, and $\mathbf{H}_{\text{eff}}$ is the effective field acting on the spin moment. γ is the gyromagnetic ratio, and α is the Gilbert damping constant. Eq. 2.2 describes the movement of a spin moment around the effective field. There are two parts of the motion in the right side of Eq. 2.2: the first part $-\mathbf{S} \times \mathbf{H}_{\text{eff}}$ describes the precessional motion of a spin around an axis which points to the direction of the effective field, and the direction of this torque is perpendicular to the $\mathbf{S} - \mathbf{H}$ plane to force the precession of the spin, shown in Fig. 2.1(a). The second part $-\mathbf{S} \times (\mathbf{S} \times \mathbf{H}_{\text{eff}})$ stands for the spin relaxation, and the direction of this torque points from $\mathbf{S}$ to $\mathbf{H}$, pulling the spin into the direction of the effective field, shown in Fig. 2.1(b).

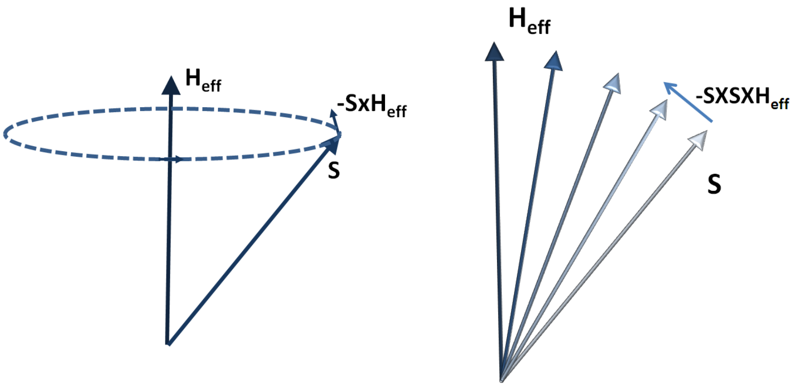

(a) Sketch of spin precession

(b) Sketch of spin relaxation

Figure. 2.1: (a):Spin precession around the effective field, $-\mathbf{S} \times \mathbf{H}_{\text{eff}}$ is perpendicular to the $\mathbf{S} - \mathbf{H}$ plane. (b): Spin relaxation, $-\mathbf{S} \times (\mathbf{S} \times \mathbf{H}_{\text{eff}})$ points from $\mathbf{S}$ to $\mathbf{H}$.

The Gilbert damping constant was proposed by T.L.Gilbert in 1955 [14], to replace the previous phenomenological damping constant in Landau-Lifshitz equation. The dimensionless damping constant is a characteristic material parameter. For experimental measurements by such as ferromagnetic resonance

(FMR), the damping constant is not well understood by theory research. Mo. et al [15] mentioned several factors giving contribution to the damping constant: inhomogeneity line broadening and two magnon grain boundary scattering have large contribution to the standard half power linewidth. A relatively small and materials consistent magnon electron scattering term and the corresponding α value only give a small back-ground intrinsic contribution to the damping.

In Eq. 2.2, the pre-factor of two torque terms are $\mathbf{f}_1 = \gamma/(1+\alpha^2)$ and $\mathbf{f}_2 = \alpha\gamma/(1+\alpha^2)$, where γ is a constant. These two pre-factors effect the different two parts of motion of a spin. Fig. 2.2 shows the changing of these two pre-factors with a varying α. According to Fig. 2.2, it can be seen when α increases, $\mathbf{f}_1$ decreases, causing the precessional motion of the spin slow down. While $\mathbf{f}_2$ increases with the increasing damping, and this results the relaxation of the spin faster to the effective field. Fig. 2.3 shows a test of a single spin relaxation at different damping constant. The spin is initially aligned in x-y plane at $\mathbf{S}_0$(0.707, 0.707, 0.0). An applied field is along z-direction. Anisotropy and exchange are not considered. Therefore the spin precesses around the z axis. For very small damping $\alpha = 0.01$ in Fig. 2.3(a), the spin components in x-y plane relax very slowly, up to 0.1 nanosecond the spin still has not approached the z direction. Fig. 2.3(b) shows a larger damping $\alpha = 0.1$, with which the spin relaxation finished in tens of picoseconds. For very large damping, such as $\alpha = 1.0$ in

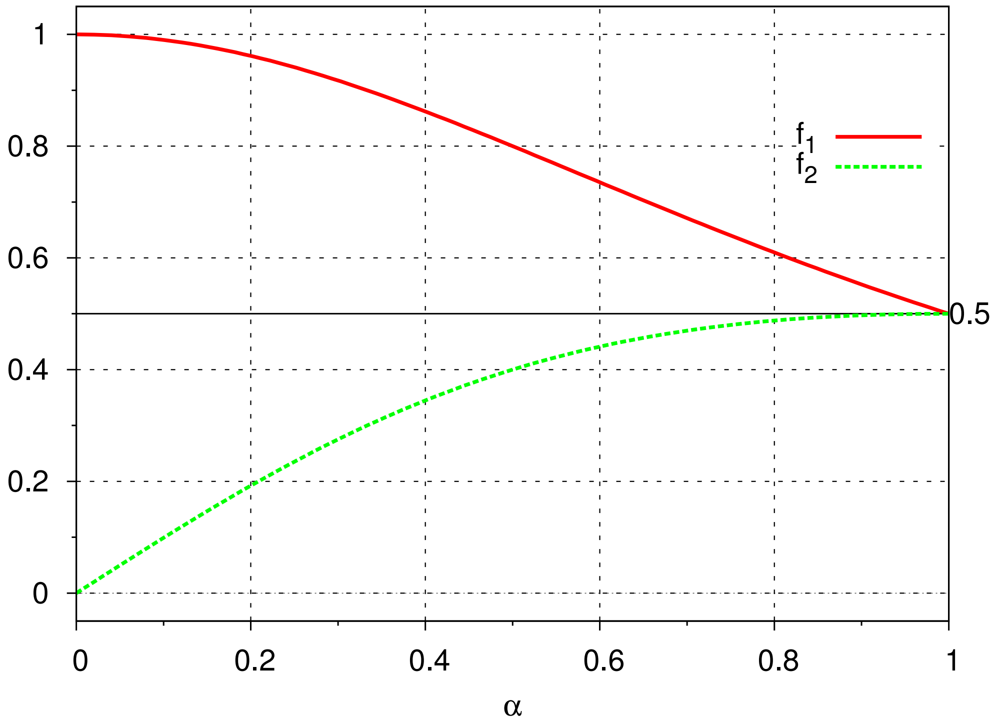

Figure. 2.2: Pre-factors in Eq. 2.2, $\mathbf{f}_1 = \gamma/(1+\alpha^2)$ and $\mathbf{f}_2 = \alpha\gamma/(1+\alpha^2)$, as a function of damping constant α.

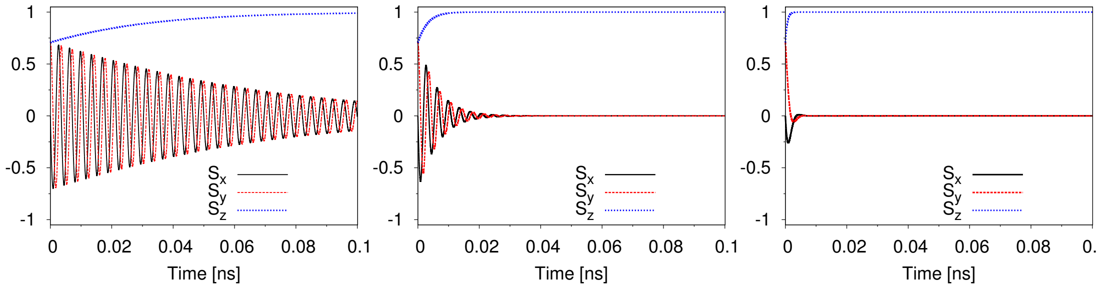

(a) damping=0.01 (b) damping=0.1 (c) damping=1.0

Figure. 2.3: Spin relaxation at different damping constant

Fig. 2.3(c), the spin relaxes extremely fast, around several picoseconds. If the damping continuous to increase, the relaxation will reduce eventually because of the Gilbert damping term in the LLG equation. The optimal reversal speed is for $\alpha = 1.0$. In this thesis, the damping constant is taken as 0.1, which is appropriate for hard materials[16].

2.3 Spin Hamiltonian

The effective field $\mathbf{H}_{\text{eff}}$ in Eq. 2.2 is the negative first order differential of a classic spin Hamiltonian $\mathcal{H}$ plus a thermal term $\mathbf{H}_{\text{th}}$:

$$\mathbf{H}_{\text{eff}} = -\frac{\partial \mathcal{H}}{\partial \mathbf{S}} + \mathbf{H}_{\text{th}} \tag{2.3}$$

The spin Hamiltonian contains the exchange term, the anisotropy term, the applied term, and the demagnetic term. The spin Hamiltonian has the form:

$$\mathcal{H} = \mathcal{H}_{ex} + \mathcal{H}_{anis} + \mathcal{H}_{applied} + \mathcal{H}_{dipolar} \tag{2.4}$$

2.3.1 Exchange Coupling

The first term in Eq. 2.4 is the exchange term, which uses the Heisenberg direct exchange model, having the form:

$$\mathcal{H}_{ex} = -\sum_{j \in N_i} J_{ij} \mathbf{S}_i \cdot \mathbf{S}_j \tag{2.5}$$

Where $\mathbf{S}_i$ is the spin moment on site i, $\mathbf{S}_j$ is the spin moment on site j, N_i are the nearest neighbours of site i. J_{ij} is the exchange coupling constant. In a ferromagnetic material, J_{ij} is a positive value, so that the two spins on neighbouring sites will align parallel to minimize the exchange energy. In an antiferromagnetic material, J_{ij} is a negative value and the exchange energy will approach the minimum when neighbouring spins are anti-parallel. For different crystal structures, the number of nearest neighbours of each spin is different. For a simple cubic (SC) structure, the number of nearest neighbours is 6, body centre cubic (BCC) 8 and face centre cubic (FCC) 12.

2.3.2 *Magnetocrystalline Anisotropy*

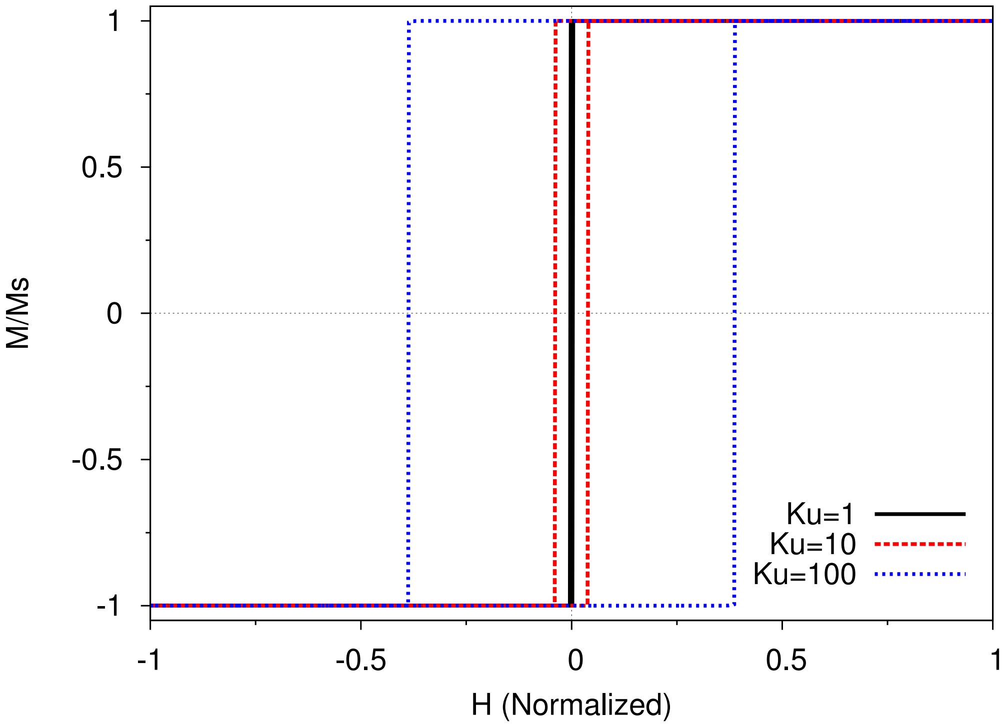

Figure. 2.4: Hysteresis loops of a single spin with different K_u values at zero Kelvin. An external field is applied along the direction of the magnetocrystalline anisotropy, which is the easy axis. The applied field and magnetization are both normalized.

The magnetocrystalline anisotropy used in this thesis is single ion uniaxial anisotropy, which makes spins preferring to align along a certain magnetocrystalline axis, the easy axis. Along the easy axis, each of the two opposite directions is the minimum of energy, therefore the spins will align in either direction. The anisotropy Hamiltonian has the form:

$$\mathcal{H}_{anis} = -\sum K_u(\mathbf{S_i} \cdot \mathbf{e})^2 \tag{2.6}$$

Where K_u is the single-ion anisotropy constant per atom, $\mathbf{S_i}$ is the spin moment, and $\mathbf{e}$ the easy axis. For magnetic recording media such as $L1_0$ FePt, the magnetocrystalline anisotropy is perpendicular to the film plane, and has a very large value. The effect of the magnetocrystalline anisotropy is to give a so-called hysteresis in a M-H loop. A simple example of a single spin is shown in Fig: 2.4. The magnetocrystalline anisotropy constant K_u increases the coercivity in a hysteresis loop which represents the field where spin moment switches from one minimum energy direction to the opposite one. The effect of anisotropy is to increase the energy barrier between easy and hard axes and make it difficult to switch the spin moments.

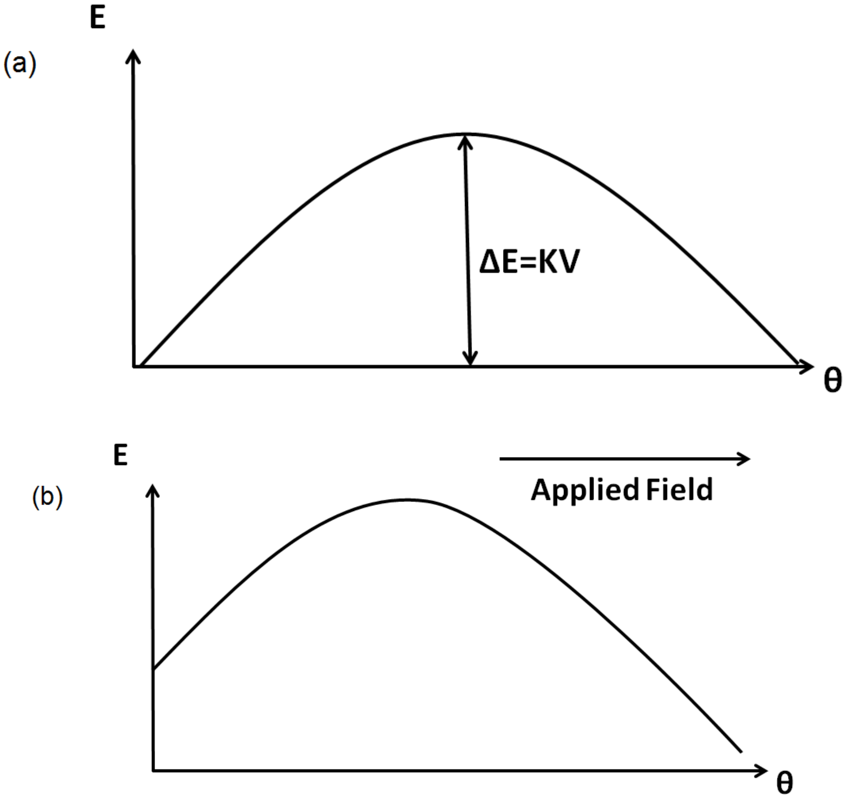

Figure. 2.5: Sketch of energy barrier without (a) and with an applied field (b)

2.3.3 *Applied Field Term*

The applied energy, or called Zeeman energy, is the effect of external magnetic field $\mathbf{H}_{applied}$ acting on the magnetic moment $\mathbf{S}$. The applied Hamiltonian has the form:

$$\mathcal{H}_{applied} = \mathbf{H}_{applied} \cdot \mathbf{S} \tag{2.7}$$

Where $\mathbf{H}_{applied}$ is applied field. In a classic energy barrier of a magnetic materials, the effect of applied field is to reduce the energy barrier, to align the spins in the same direction of the external applied field.

From the point view of energy barrier, the magnetocrystalline anisotropy gives a symmetric energy barrier because along the easy axis the energy is the minimum, and perpendicular to the easy axis is the maximum value of energy, shown in Fig. 2.5(a). In the meantime, if an external magnetic field is applied, its effect is to break the symmetry leading to a preferred orientation in the field direction.

2.3.4 Dipolar Term

The magnetic dipolar-dipolar coupling is a long range interaction between two magnetic dipoles, or in an atomistic modelling system, between two spins. The dipolar coupling energy between a moment $\mathbf{m}_j$ and $\mathbf{m}_k$ has the form:

$$\mathcal{H}_{dipolar} = -\frac{\mu_0}{4\pi r_{jk}^3}[3(\mathbf{m}_j \cdot \mathbf{r}_{jk})(\mathbf{m}_k \cdot \mathbf{r}_{kj}) - (\mathbf{m}_j \cdot \mathbf{m}_k)] \tag{2.8}$$

Where $\mathbf{r}_{jk}$ and $\mathbf{r}_{kj}$ are the unit vectors pointing from moment j to k, or from k to j, respectively. r_{jk} is the distance between the two moments. The effect of the dipolar interaction is to demagnetize the magnetic system, therefore it also can be called the demagnetization term. For a thin film or bulk magnetic material, the magnetic material will be split into small volumes called magnetic domains, to reduce the demagnetizing energy. The size of the magnetic domain is determined by the competition between the domain wall energy and the demagnetizing energy. In this thesis, we consider recording media, which generally consists of single domain magnetic particles. Because the large values of anisotropy considered, the internal demagnetisation field of individual particles is neglected.

2.3.5 Thermal Field

Thermal effects are taken into account by using Langevin Dynamics [17, 18], which introduces an effective thermal field H_{th} into the effective field in the effective field:

$$\mathbf{H}_{th} = \Gamma(t)\sqrt{\frac{2\alpha k_B T}{\gamma \mu_s \Delta t}} \tag{2.9}$$

where $\Gamma(t)$ is a Gaussian distribution with a mean value of zero. α is the damping constant, k_B is the Boltzmann constant, and T is the system temperature in Kelvin. γ is the gyromagnetic ratio, μ_s is the magnitude of the spin moment, and Δt is the integration time step [19].

The thermal field has an effect on the spin dynamics. Fig. 2.6 presents the magnetization rotation of a single Co grain which has 5 nm in diameter and 5 nm thickness, in the x-y plane at different temperatures. The magnetization of the single grain is initialized at x axis, and an external field as large as 1 Tesla is applied at z axis. It can be seen from the in-plane magnetization at zero temperature, the magnetization rotates coherently, while at room temperature 300 K, the magnetization rotates coherently but has some fluctuations. When the temperature is up to 800 K, the magnetization has larger fluctuations, while at 1000 K, the magnetization is random.

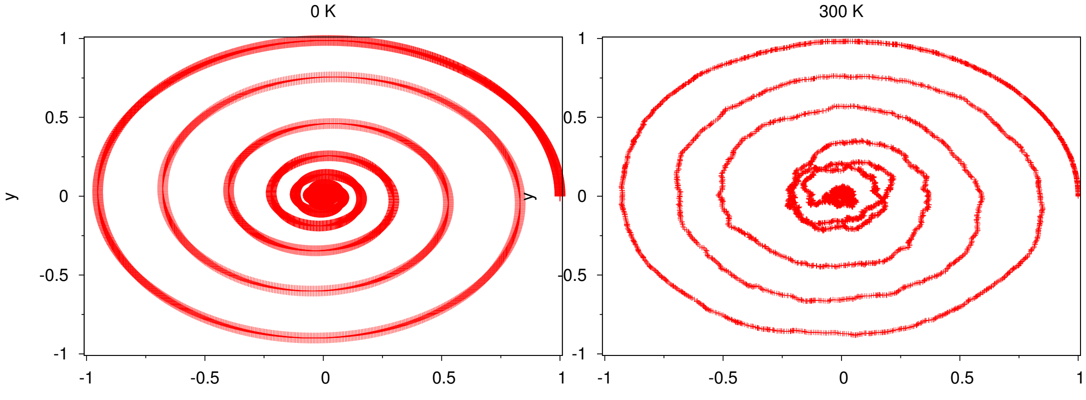

(a) 0 K (b) 300K

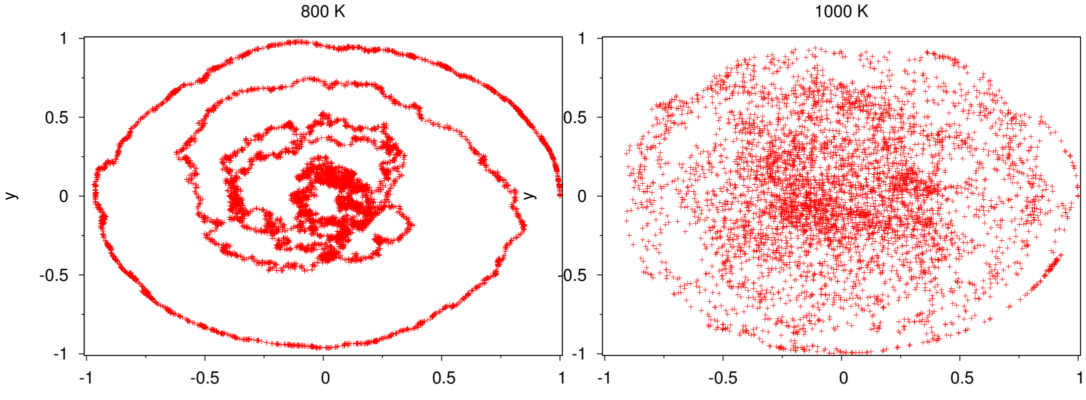

(c) 800 K (d) 1000 K

Figure. 2.6: Temperature dependent magnetization dynamics in x-y plane.

In addition, the thermal effect also plays a role on the magnitude of the magnetization. Fig. 2.7 shows the temperature dependent magnetization of a single FePt grain, which is 5 nm in diameter and 5 nm thickness. The magnetization reduces with increasing temperature and approaches zero at some temperature, which is called the Curie Temperature, i.e. 690 K in Fig. 2.7. The reduction of the magnetization originates from the disordering of the spins arising from the increasing temperature, resulting in the reduction of total magnetization which is the vector sum of all the spin moments.

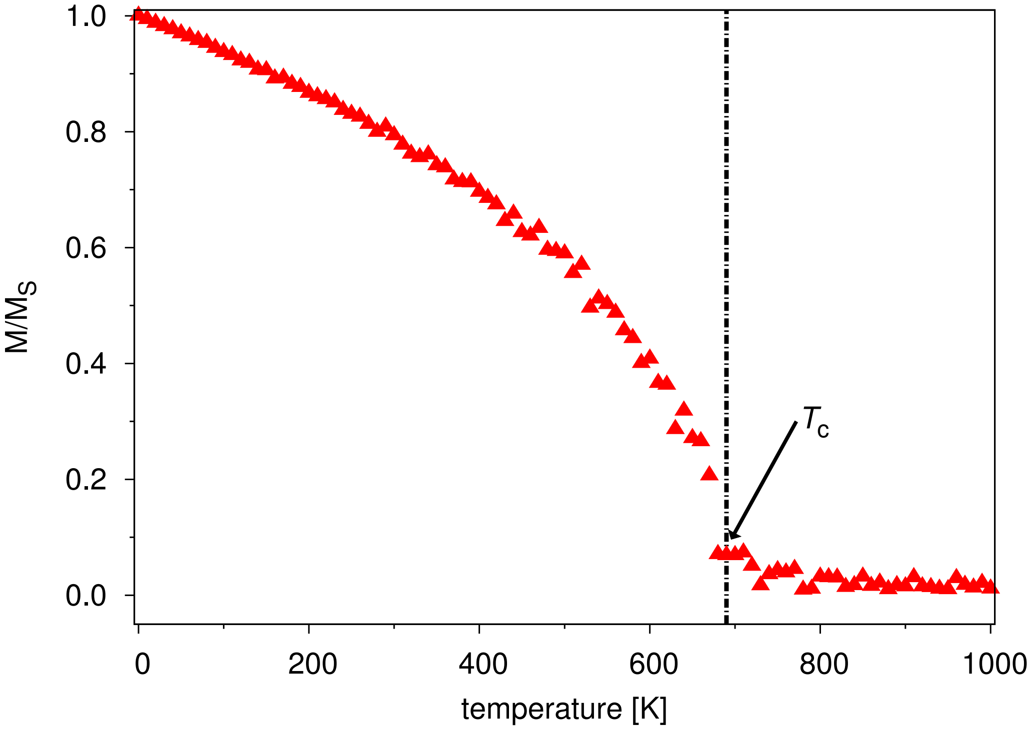

Figure. 2.7: Temperature dependent magnetization of a single FePt grain, grainsize=5 nm.

2.4 Hamiltonian of $L1_0$ FePt

Effective Spin Hamiltonian Model

The chemically ordered $L1_0$ phase of FePt has attracted much attention because of its high potential application in perpendicular magnetic recording media, and it's therefore the main magnetic material used thorough this thesis. An $L1_0$ ordered FePt is face centred tetragonal (FCT), with Fe atoms located on 8 corners and centres of top and bottom faces, and Pt atoms on the middle level (Fig. 2.8(a)), and this makes the chemical composition to be Fe:Pt=1:1.

An effective spin Hamiltonian model [20] based on first principles calculations is used thorough this thesis, which effectively assumes uniform FePt atoms all over the FCT sites with unit vector magnetic moment and anisotropy constant. Therefore the atomic structure of FePt in Fig. 2.8(a) can be transferred to Fig. 2.8(b), using uniform FePt atoms instead of Fe, Pt atoms on the FCT crystal sites. The detailed magnetic parameters used for this uniform FePt atoms are shown in Fig. 2.8.

The Hamiltonian of this generic model of FePt is as follows:

$$\mathcal{H} = -\sum_{j\in N_i} J_{ij}\mathbf{S}_i \cdot \mathbf{S}_j - \sum K_u(\mathbf{S_i} \cdot \mathbf{e})^2 + \mathbf{H}_{applied} \cdot \mathbf{S} \tag{2.10}$$

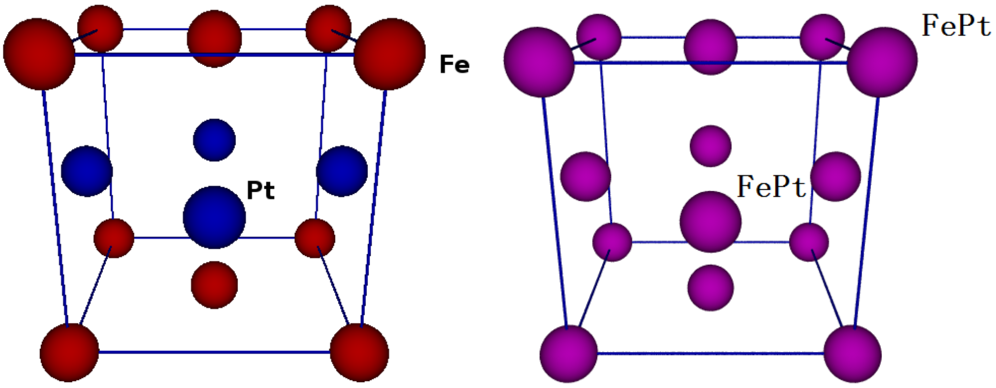

(a) $L1_0$ ordered FePt (b) Effective spin model FePt

Figure. 2.8: (a): schematic diagram of an $L1_0$ FePt unit cell. Fe atoms (red) locate on 8 corners and centres of top and bottom faces. Pt atoms (blue) are on the middle level. (b): schematic diagram of an effective spin model of FePt, using uniform FePt atoms over all the FCT sites.

where the first term stands for the exchange term, the second term is the anisotropy term and the third one is the applied field.

The thermal effect is also taken into account by using the Langevin dynamics which is discussed previously. The magnetostatic term is also considered in several calculations by using the mentioned dipolar-dipolar interaction. The magnetic moment of a Fe atom is $2.38 \pm 0.26\mu_B$, and $0.41 \pm 0.04\mu_B$ for Pt in a $L1_0$ FePt [21]. For atomistic scaling modelling, we assume uniform atoms on each FCT sites with a mean value of magnetic moment of $1.458\mu_B$, where μ_B is the Bohr magneton.

The exchange coupling model used in $L1_0$ FePt is also a Heisenberg model, which takes account the direct exchange coupling between nearest neighbouring atoms. For a typical FCT structure, each atom in FePt has 12 nearest neighbours. The exchange interaction parameter $J_{ij} = 3.0 \times 10^{-21}$ Joules per link [21].

The $L1_0$ ordered FePt has a very strong perpendicular magnetocrystalline anisotropy, which is a key factor for the perpendicular magnetic recording media. The anisotropy constant used in our calculation is 4.94×10^{-23} Joules per atom.

2.5 Hamiltonian of CoPt

The spin Hamiltonian of CoPt is similar as FePt, also an effective spin mode, assuming uniform CoPt atoms on the FCT sites, instead of individual Co, Pt atoms in a $L1_0$ ordered CoPt. The magnetic moment of CoPt is $1.5\mu_B$, the exchange constant $J_{ij} = 4.8 \times 10^{-21}$ Joules, and the anisotropy constant $K_u = 4.644 \times 10^{-23}$ Joules [22]. The number of nearest neighbours for one CoPt atom is 12 in a FCT structure.

2.6 Integration Solution

The computational numerical method to solve the LLG equation is the Heun method, which is modified from a Euler method to a two stage second order Runge-Kutta method [23]. Firstly, Eq. 2.2 is rewritten:

$$\frac{\partial \mathbf{S}}{\partial t}(\mathbf{S},t) = -\frac{\gamma}{1+\alpha^2}[\mathbf{S}\times\mathbf{H}_{eff} + \alpha\mathbf{S}\times(\mathbf{S}\times\mathbf{H}_{eff})] \tag{2.11}$$

An Euler step is then defined:

$$\mathbf{S}_{euler} = \mathbf{S}_t + \frac{\partial \mathbf{S}}{\partial t}(\mathbf{S},t)\Delta t \tag{2.12}$$

Where Δt is the integration time step. The Euler method assumes linear value of an ordinary differential equation at each integrated time step. At a Heun corrected step:

$$\mathbf{S}_{t+1} = \mathbf{S}_t + \frac{1}{2}[\frac{\partial \mathbf{S}}{\partial t}(\mathbf{S},t) + \frac{\partial \mathbf{S}}{\partial t}(\mathbf{S}_{euler},t+1)]\Delta t \tag{2.13}$$

All the spins are integrated by using this Heun method, to perform a completed time process.

In the integration, the time step Δt is a fundamental parameter. On one hand, smaller time step will give a more accurate solution of the differential equation. On the other hand, using smaller time step will extend the total calculation time. This value is related to the precession frequency which is determined by the magnitude of the effective field $\mathbf{H}_{\text{eff}}$. For a larger $\mathbf{H}_{\text{eff}}$, the precession is faster and a smaller time step is required. In this atomistic model, a time step of $\Delta t = 10^{-15}$ second is used, to approach the spin dynamics more accurately and also to simulate the ultra-fast spin dynamics processes.

2.7 Conclusion

This chapter introduces the computational method used in this thesis. An atomistic spin model is applied to calculate the spin dynamics by using the LLG equation. A spin Hamiltonian based on Heisenberg model and Langevin dynamics is also described. Furthermore, an effective spin model of $L1_0$ ordered FePt is given to refer the parameters used thorough the calculations in this thesis. In the following chapters, we use the atomistic model described in this chapter to calculate the dynamics of magnetic recording media, focusing on the exchange coupling, the heat assisted magnetic recording process and exchange coupled composite media.

3. Control of the Exchange Coupling in Granular CoPt Magnetic Recording Media

The exchange coupling between magnetic grains has an impact on the grain reversal process and the coercive field of a magnetic recording media. In this chapter, this inter-granular exchange coupling is studied. In the most common situation, this exchange coupling can be varied by controlling the oxide thickness between the grains. However, as the grain size is decreased, it is harder to control the oxide thickness. One possible solution is to totally decouple the grains with very thick oxide and apply a capping layer to get uniform coupling. In the first section, a system of seven CoPt grains coupled with a continuous Co layer is investigated using the atomistic model. There is no exchange coupling between the CoPt grains which are just coupled by the Co layer. In the second section, in order to directly study the inter-granular exchange coupling, a constrained Monte Carlo method is used to study the intergranular exchange coupling by varying the density of the atoms in the spacer between two grains and also the size of the spacer. Furthermore, in the final section, seven CoPt grains with some doping CoPt atoms in the oxide spacer between the grains is simulated. The coercivity of this system is also calculated as a function of the density of the doping atoms. This study on inter-granular exchange coupling might help to understand the reversal process of the magnetic grains, and how such controllable exchange coupling can also achieve long term thermal stability of data in high density magnetic recording media.

3.1 Control of the exchange coupling in CoPt/Co Bilayers

3.1.1 Introduction

In recent years, CoPt granular materials have attracted much attention because of their strong (perpendicular) magnetic anisotropy and their application in magnetic recording media [24, 25, 26, 27, 28, 29]. The magnetic properties of CoPt films are affected by the exchange coupling between the grains, which is generally controlled by varying the thickness of the oxide that is applied as a spacer between the grains. Along with the rapidly increasing density of magnetic recording at present, the CoPt grain-size decreases, which makes it harder to control the thickness of the oxide spacer between the grains. This can lead to fully coupled and decoupled grains, which creates a wider dispersion of magnetic properties and worsening of the signal to noise ratio. One possible solution to this problem is to totally decouple the grains with a very thick oxide and apply an exchange capping layer to achieve uniform exchange coupling. So far, experimental work has been carried out in granular CoPt/Co[22] and FePt/Fe [30, 31, 32] bilayers with perpendicular anisotropy, which has also reported the impact of exchange coupling on coercivity and reversal processes. In particular, theoretical work has been done by Goto *et al*.[33] and Asti *et al* [34] by micromagnetic calculation. In this Chapter we study the granular CoPt/Co bilayers using an atomistic spin model, which is able to show the detailed reversal processes of the system, focusing on the impact of the exchange coupling on the reversal processes and the coercivity of the system.

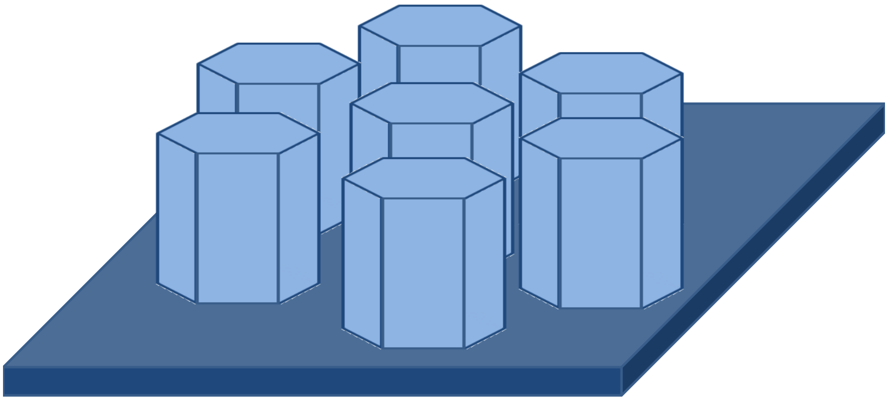

Figure. 3.1: The schematic diagram of the CoPt grains coupled with a continuous Co layer. The "larger system" in this chapter means the CoPt grains are hexagonal columns with 5 nm diagonal in the hexagonal plane and 5 nm thickness; the spacer between the grains is 1 nm. The "smaller system" refers to the 3 nm diagonal and 5 nm thickness CoPt grains, and the spacer is 0.5 nm.

Fig. 3.1 shows a schematic diagram of the coupled granular continuous CoPt/Co bilayers. The granular layer contains 7 hexagonal grains, whose thickness is 5 nm. The "larger system" studied in this chapter means the diagonal of the grains is 5 nm, and the spacer between the grains is 1 nm. The "smaller system" contains grains with 3 nm diagonal and 0.5 nm spacer between the grains. The spacer between the grains is assumed to be SiO_2 with no magnetic moment in this section. In the later sections, doping magnetic atoms in the spacer will be considered, therefore this figure will also be used again in the later section. The material of the grains is $L1_0$ ordered CoPt, with high uniaxial anisotropy $K_u = 4.644 \times 10^{-23}$ Joules/atom and exchange parameter $J_{CoPt} = 4.8 \times 10^{-21}$ Joules. The continuous layer is Co, whose uniaxial anisotropy is much lower: $K_u = 4.644 \times 10^{-25}$ Joules/atom, and the exchange parameter $J_{Co} = 4.2 \times 10^{-21}$ Joules. The simulation uses the atomistic model. The spin dynamics is calculated by using the Landau-Lifshitz-Gilbert equation, the Hamiltonian is the effective spin Hamiltonian discussed in Chapter 2. The saturated magnetic moment of the effective CoPt is 1.5 μ_b, and the magnetic moment of Co is also 1.5 μ_b. According to the Heisenberg nearest neighbouring model, the spins will only be coupled with the ones on the nearest neighbouring sites. So the 7 CoPt grains are totally decoupled with each other since there is a spacer larger than lattice constant between the grains. The continuous Co layer is directly contacted to the grains, so the exchange coupling between the grains and the continuous layer depends on the interface exchange parameter J_{ij}, which varies from 0 to 2.2×10^{-21} Joules.

3.1.2 Reversal Processes

Fig. 3.2(a) shows typical hysteresis loops of the larger system with 5 nm grain-size and 1nm spacer. The black-colour line presents the exchange coupled case, with the interface exchange coupling parameter $J_{ij} = 2.2 \times 10^{-21}$ J. As a comparison, the red-colour line shows the non-exchange coupled case where the interface exchange coupling parameter is zero. For the non-exchange coupled case, two obvious steps, left branch of the red line from -0.5 Tesla to -4 Tesla, and the right branch from 0.5 Tesla to 4 Tesla, can be observed. In the meantime, several smaller steps can also be found after the main large step. While for the exchange coupled case (black line in Fig. 3.2(a)), there are no such obvious steps. The first large step in the non-exchange coupled case originates from the reversal of the Co layer, because the Co has a lower anisotropy and smaller coercivity. The remaining smaller steps demonstrate the independent reversal of the CoPt grains, which have no exchange coupling between each other or the Co layer. Furthermore, a reduction in the coercive field has also been found: the coercive field is reduced from around 4 Tesla to 2.6 Tesla.

Hysteresis loops of the smaller system have also been calculated, in Fig. 3.2(b). Again, the black-colour line is the exchange coupled case, and the red-colour line presents the non-exchange coupled case. More steps can be observed in the non-exchange coupled case and the coercivity has also been reduced to 2.5 Tesla, compared to the larger system in Fig. 3.2(a). This result shows the impact of thermal effects on the reversal processes and coercivity: the thermal

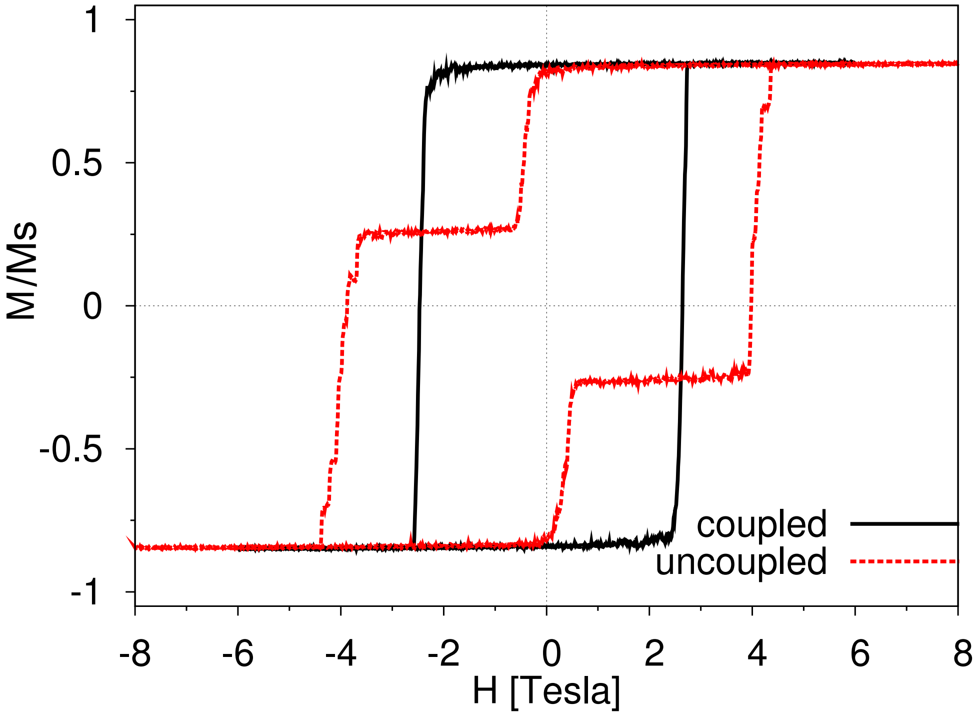

(a) grain size 5 nm

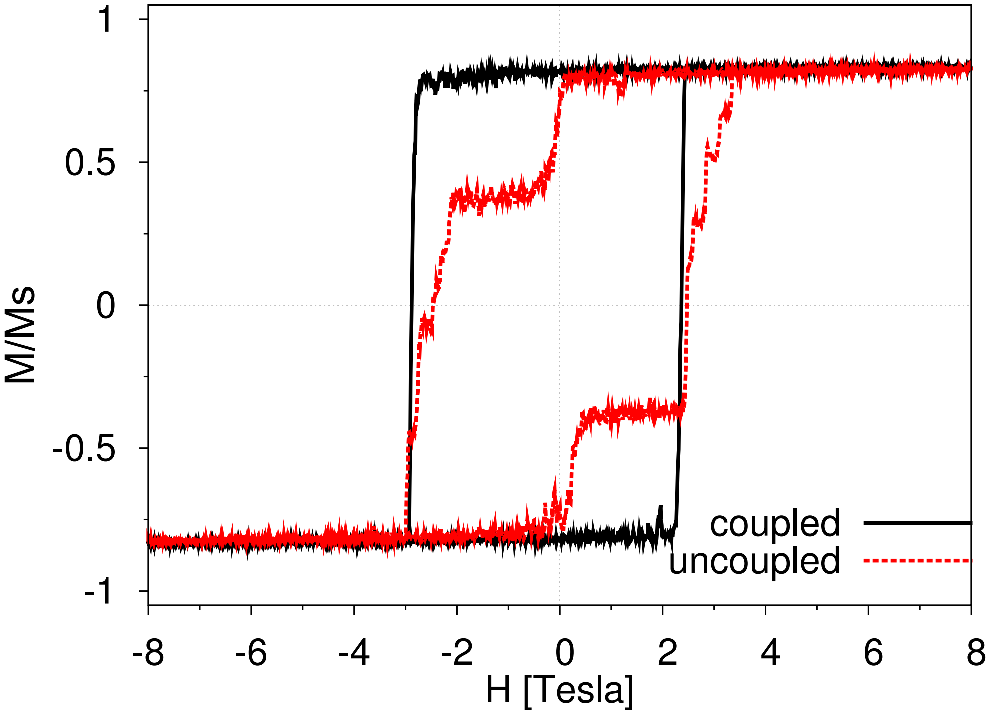

(b) grain size 3 nm

Figure. 3.2: Hysteresis loops of CoPt/Co bilayers for different grain sizes. Fig. 3.2(a) shows the hysteresis loops of both coupled (black) and non-coupled (red) system with 5 nm grain size and 1 nm spacer. Fig. 3.2(b) presents the hysteresis loops of both coupled (black) and non-coupled (red) system with 3 nm grain size and 0.5 nm spacer.

energy reduces the coercivity of the whole system and increases the dispersion of the reversal field of each single grain. Furthermore, the hysteresis loop of the exchange coupled case, the black line, is much more square and no steps can be seen on the loop. The coercivity of the exchange coupled case is almost the same as that in the larger system, around 2.6 Tesla. This is mainly because when the grains are strongly coupled with a large continuous layer, the difference in the grain size will not effect the coercivity too much, or in other words, the thermal effect is not pronounced.

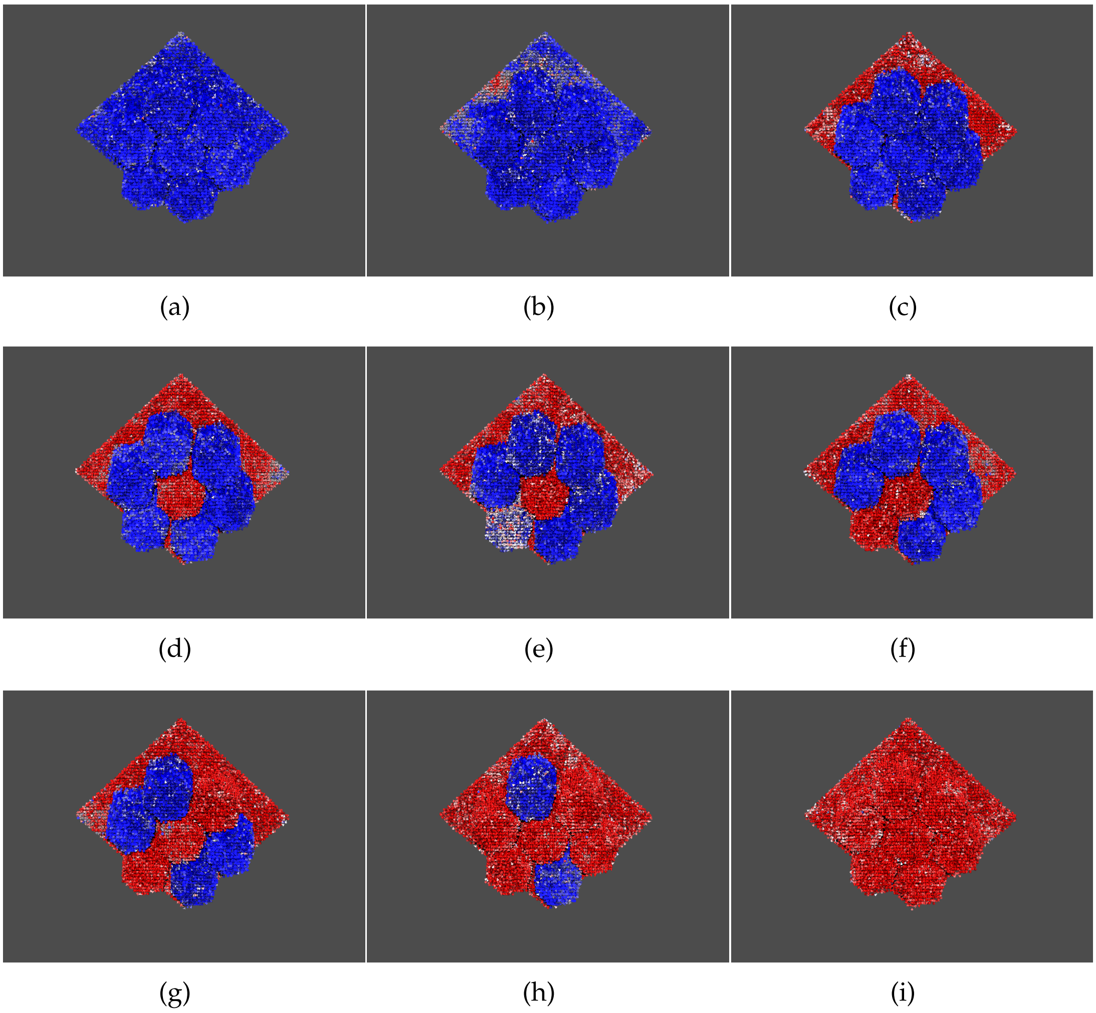
(a) (b) (c)
(d) (e) (f)
(g) (h) (i)

Figure. 3.3: Reversal processes of CoPt/Co bilayers, grain size=3 nm, with no interface interaction.

In order to analyse the reversal process, a series of visualization figures of the spin structures of the smaller system are created in Fig. 3.3 and Fig. 3.4. The direction of the spins are presented by different colours. Blue means spin up and red is spin down, while the lighter colour shows the intermediate states between up and down. Fig. 3.3 shows the figures around the switching field on the hysteresis loop the smaller system without interface exchange coupling. Fig. 3.3(a) is the spin structure before reversal, so we can only see blue colour which means all the spins are in the +z direction. Fig. 3.3(b) presents nucleated reversal in the continuous layer, which is the starting point of the reversal of the continuous Co layer. Essentially the red areas indicate to the nucleation of some domains. In Fig. 3.3(c) we can see a large red continuous layer, which means the Co layer has reversed at this point. This point is also the starting point of the large step on left branch of the red hysteresis loop in Fig. 3.2(b). Fig. 3.3(d) has one red grain in the middle, demonstrating one of the FePt grains has reversed. Afterwards, in Fig. 3.3(e) to Fig. 3.3(h), more and more grains turn to more red areas, indicating reversal, corresponding to the smaller steps on the left branch of the red hysteresis loop in Fig. 3.2(b). By Fig. 3.3(i), the reversal process of the whole system has finished. It can be clearly observed in Fig. 3.3 that the Co layer reverses initially and then the CoPt grains reverse independently when there is no exchange coupling between the grains and the Co layer.

Fig. 3.4 shows the figures before and after the left switching field on the black hysteresis loop in Fig. 3.2(b) of the smaller system with interface exchange coupling $J_{ij} = 2.2 \times 10^{-21}$ J between the CoPt grains and the continuous Co layer. The reversal process is very different from that of the non exchange coupled case in Fig. 3.3. From Fig. 3.4(a) to Fig. 3.4(f), only some little red and lighter colour spots can be seen in the blue system, referring to the nucleation of some domains. In Fig. 3.4(g), we can see a very clear domain wall on the upper corner of the system. Afterwards this domain propagates rapidly; in Fig. 3.4(h), five of the seven CoPt grains have reversed, in the meantime, the Co layer is also partly reversed. This domain propagates further until finishing the whole reversal process in Fig. 3.4(i). In this case, the grains reverse almost simultaneously and domain walls also appear in the Co layer. This phenomenon shows that the exchange coupling between one grain and the Co layer can be transmitted to its neighbouring grains.

3.1.3 Control of the Exchange Coupling

Varying the Interfacial Exchange Constant

As seen in Fig. 3.2, Fig. 3.3 and Fig. 3.4, the exchange coupling between the CoPt grains and the Co layer has an impact on the coercivity of the whole system and the reversal processes of the grains. However a detailed analysis of the effect of the exchange coupling parameter on the coercivity is still lacking. Therefore, in order to study the impact of exchange coupling thoroughly, the coercivities of both the larger and smaller systems as a function of the exchange coupling parameter J_{ij} between the grains and the Co layer have been calculated. The interface exchange coupling parameter between the CoPt atoms and the Co atoms

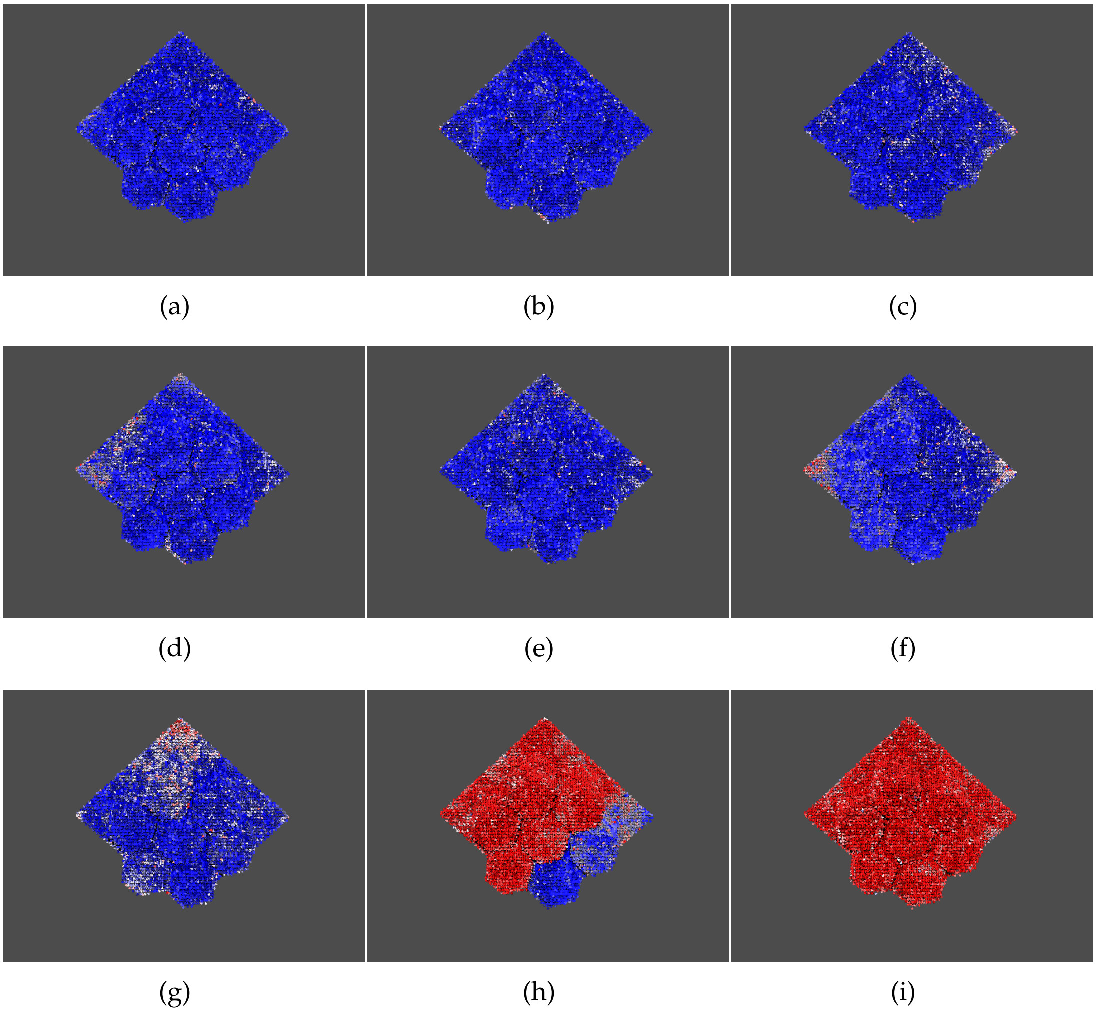

Figure. 3.4: Reversal processes of CoPt/Co bilayers, grain size=3 nm, with an interface interaction of Jij=2.2e-21 Joules.

J_{ij} varies from 0 to 2.2×10^{-21} Joules. The results are shown in Fig. 3.5 for both systems. Consider first the larger grain system. A very sharp decrease in coercivity is found for relatively small values of the exchange leading to a minimum in the coercivity which increases to a constant value as J_{ij} tends to the bulk value. Similar behaviour was observed by Garcia-Sanchez et al [35] in studies of soft/hard layers. The soft Co layer is too thin to support a perpendicular domain wall, and as a result an exchange-spring mechanism is unlikely [36]. This is supported by the fact that the coercivity minimum seen in Ref[35] is also predicted by two-spin models such as that of Victora and Shen [37]. In our case the reversal starts with the nucleation of an in-plane domain which propagates causing reversal of the CoPt grains. At higher values of the exchange the propagation of this domain wall is inhibited by the CoPt grains, and so the coercivity reduction is less pronounced. In the case of the smaller grain-size system, the change of coercivity with J_{ij} is much less pronounced. This is attributed to the effects of thermal activation, which is not considered in the previous models. Even for $J_{ij} = 0$, H_c is reduced relative to the larger grain system due to thermal effects.

As J_{ij} increases the behaviour tends to that of the larger grain system, presumably because the stronger exchange coupling is increasing the energy barrier to thermally activated reversal.

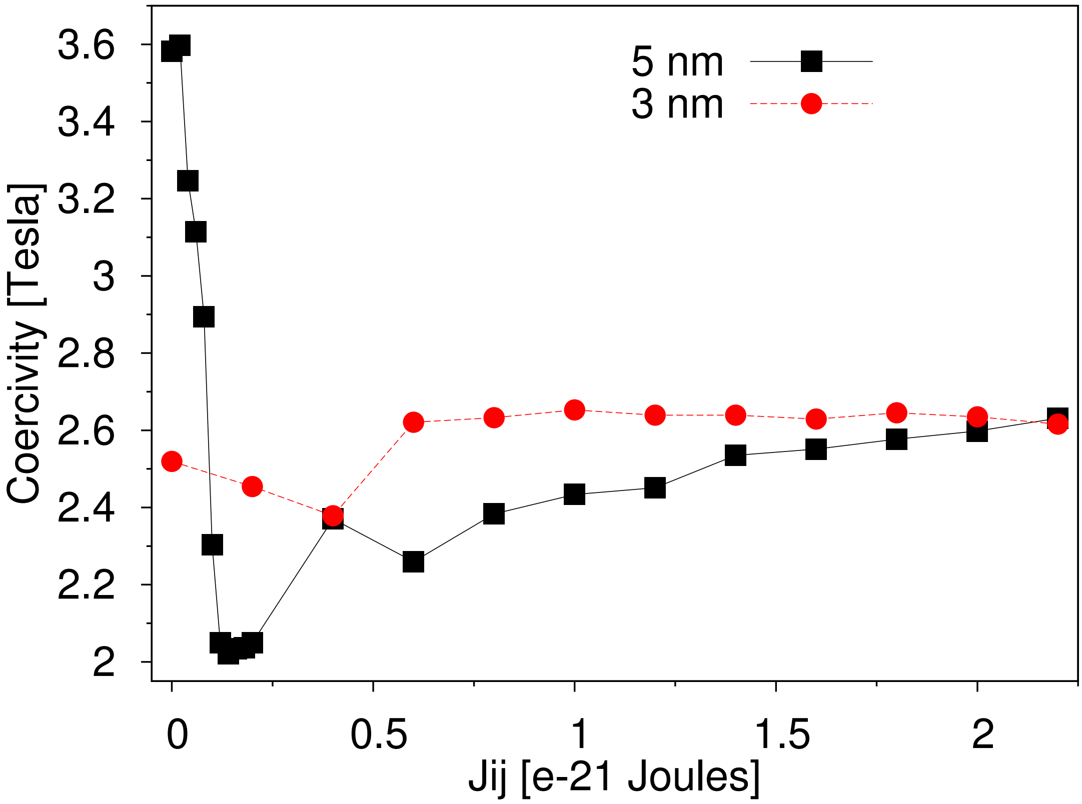

Figure. 3.5: Coercivity at Room Temperature as a function of interfacial exchange coupling constant Jij, for grain size of 5 nm (black) and 3 nm (red)

Varying the Capping Layer Thickness

Although the magnetic properties of a granular CoPt/Co bilayer can be controlled by varying the interface exchange coupling parameters, in practice it is not so easy to change the exchange coupling parameter. It is much easier to control the thickness of the exchange coupling layer (Co layer in our system). Therefore, studying the impact of the thickness of the exchange layer also becomes important. The coercivity as a function of the layer thickness of Co has also been calculated for different values of J_{ij} for the larger system, as shown in Fig. 3.6. For larger values of the exchange coupling, the decrease in the coercivity as a function of layer thickness converges to a maximum rate. For weaker exchange coupling, the effects are generally weaker, with a smaller overall reduction in the coercivity and the reduction reaching a plateau at a thickness of 4 layers. The reversal mechanism involves the nucleation of a perpendicular domain wall, followed by a propagation of the reversed volume.

For weak interlayer exchange coupling the insertion of a domain wall does not significantly contribute to a coercivity reduction in the hard layer. Given sufficient interfacial exchange any reversed domain in the capping layer can penetrate the hard layer and initiate the reversal. The contribution of the layer thickness to the reversal process is therefore determined by the ease with which a domain wall is inserted into the capping layer. Given the low coercivity and domain wall width of 20 nm (56 ML), this explains the limited reduction seen in our calculations. We would expect a high-exchange plateau in the coercivity reduction at the intrinsic coercivity of the soft layer (0.5 T). Nevertheless, a decrease in the coercivity for larger layer thickness is expected, since once the capping layer thickness is greater than the DW width, the non-collinear reversal will show a further reduced coercivity. For the strongly coupled case, it is intriguing that the coercivity of the system can be so easily controlled simply by varying the thickness of the capping layer.

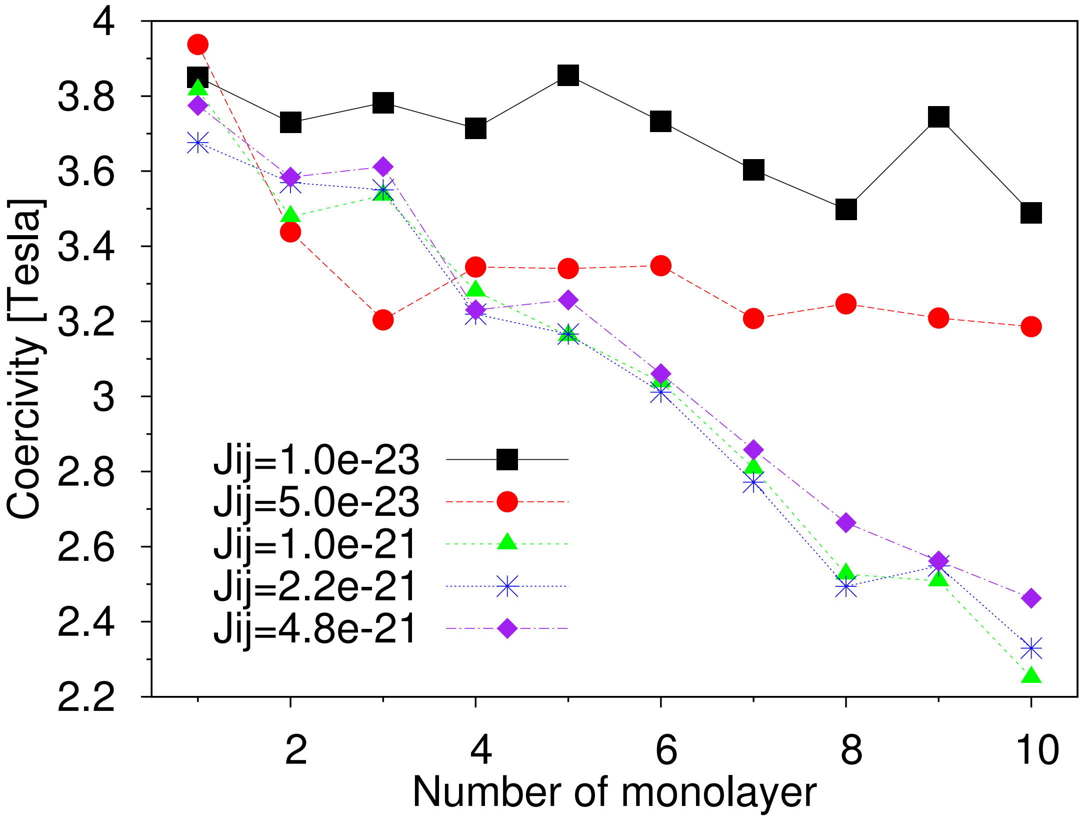

Figure. 3.6: Coercivity at Room Temperature as a function of the number of Co monolayers, for different interfacial exchange coupling constants.

3.1.4 Conclusion

In summary, an atomistic model has been used to simulate the effects of a soft capping layer on the reversal process of CoPt grains. We have found that the addition of a coupling layer reduces the coercivity of the system, and that smaller grain-sizes show a lesser decrease of the coercivity due to greater thermal fluctuations. Furthermore, we have demonstrated the effect of capping layer thickness on the coercivity of the system, and its ability to easily control the coercivity of the system.

3.2 Study of the Direct Intergranular Exchange Coupling

In previous study, we have assumed the CoPt grains are decoupled with each other by using a very thick non-magnetic oxide spacer and study the indirect inter-granular exchange coupling via the capping ferromagnetic layer. While in more realistic situation, there is always inter-granular exchange coupling and this effects the magnetic properties a lot. In this section, a direct inter-granular exchange coupling is studied by randomly doping some ferromagnetic atoms into the non-magnetic spacer. The density of the doping ferromagnetic atoms can be varied to change the effect of the inter-granular exchange coupling.

3.2.1 Monte Carlo Calculation of Exchange Coupling Between two ferromagnetic grains

In order to study the exchange coupling between two ferromagnetic grains, a Constrained Monte Carlo method is used to simulate the exchange torque and the exchange energy of the interlayer atoms between two grains. Fig. 3.7 shows a visualization figure of two constrained layers, one of which is fixed in the +z direction (Magnetic Layer 1 in Fig. 3.7), another is constrained at an angle θ varying from 0° to 180° (Magnetic Layer 2 in Fig. 3.7). Some free ferromagnetic atoms are added randomly into the spacer between these two layers, both of the density of the doping atoms and the thickness of the spacer can be varied. According to the Heisenberg Exchange Model, the exchange field will only arise from the nearest neighbouring atoms, so the interlayer exchange coupling can be controlled by varying the density and thickness of the spacer. The two magnetic layers are constrained at a fixed angle. The doping atoms within the spacer are free, their anisotropy is assumed to be zero. The Monte Carlo method has no external field applied. For the calculations in Fig. 3.8 and Fig. 3.9, thermal effect is not taken account into, so temperature in these two figures is also zero.

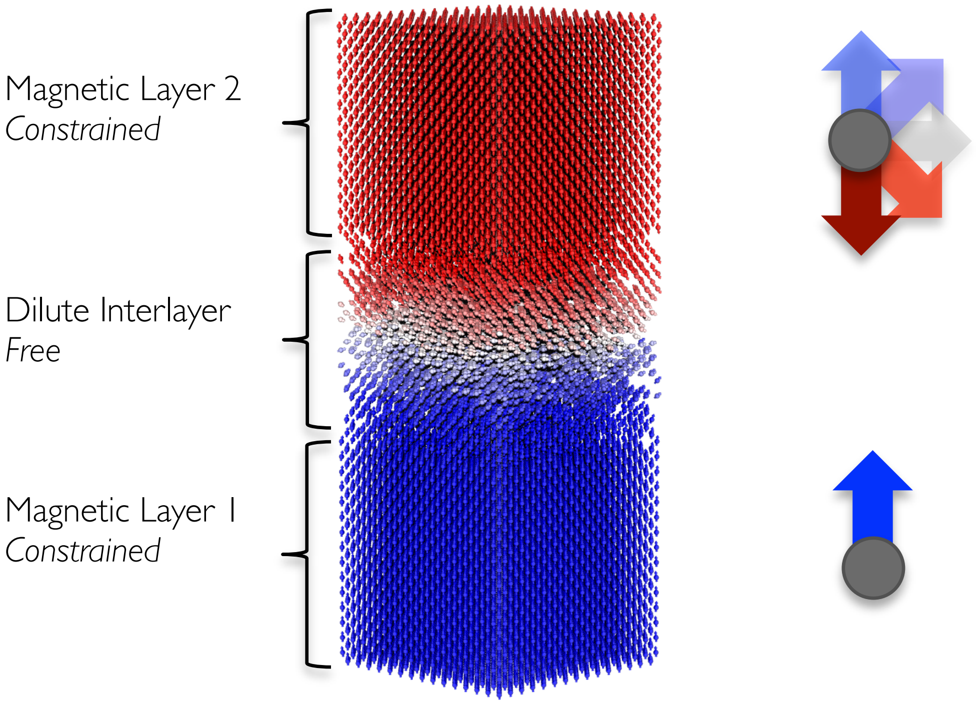

Figure. 3.7: Visualization figure of two cubic ferromagnetic grains coupled by doping ferromagnetic atoms in the spacer. All the spins in Magnetic layer 1 are constrained to the +z direction. Magnetic layer 2 is constrained at the direction with an angle $\theta = 0^\circ$ to 180° from the +z direction. The doping atoms are randomly added into the spacer between the two layers, and the density of the doping atoms can be varied from 0% to 100%.

A constrained Monte Carlo [38, 39, 40, 41, 42] is used to calculate the exchange energy of the doping atoms between the two layers. In a Monte Carlo algorithm, it is generally assumed one spin $\mathbf{S}_i$ having a random tiny move δ, causing the new spin $\mathbf{S}_i' = \mathbf{S}_i + \delta_i$. The change is accepted with a probability according to:

$$\mathcal{P} = max\left(1, exp\left[-\frac{\Delta E}{k_B T}\right]\right) \tag{3.1}$$

Additionally, move another spin $\mathbf{S}_j' = \mathbf{S}_j + \delta_j$, chosen such that there is no change in the overall magnetisation direction and calculate the energy change:

$$\Delta E_{i,j} = \Delta E(\mathbf{S}_i, \mathbf{S}_i') + \Delta E(\mathbf{S}_j, \mathbf{S}_j') \tag{3.2}$$

Furthermore, in a constrained Monte Carlo calculation, as the two layers are constrained at some angle, only the impurity atoms between the two layers can rotate, the free energy of the free atoms can be calculated from the restoring torque, which is written as follows:

$$\tau = \sum_i \mathbf{S}_i \times \mathbf{H}^i_{\text{ex}} \tag{3.3}$$

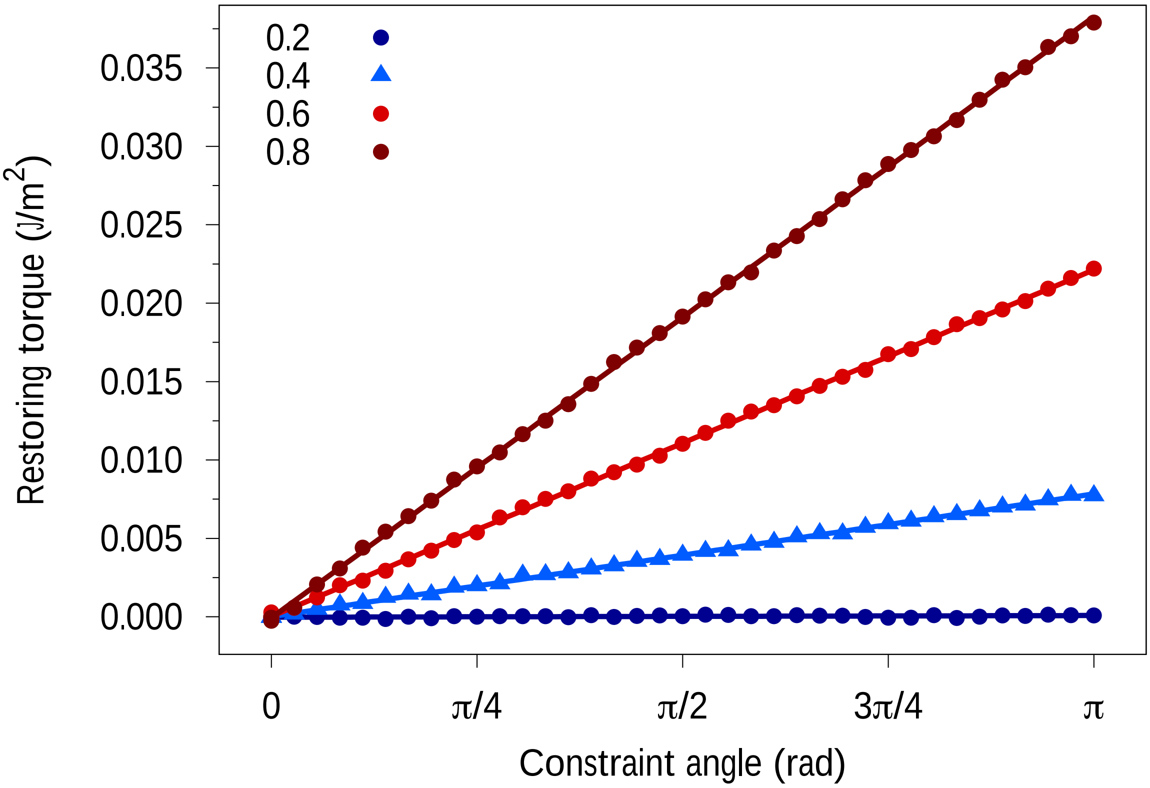

Figure. 3.8: Restoring Torque as a function of the constrained angle of Magnetic layer 2 in Fig. 3.7, for different density of the doping atoms between two layers.

Fig. 3.8 presents the restoring torque as a function of the constrained angle of Magnetic Layer 2 in Fig. 3.7, for different density of the doping atoms between two layers. The thickness of the spacer between the two layers (Fig. 3.7) is 5 nm. It can be seen for lower density of the doping atoms between the two layers, such as 20% or less, the restoring torque is zero for all the angles varying from $\theta = 0^\circ$ to 180°. This is because of the Heisenberg direct exchange mode, only the exchange interaction from the nearest neighbours are taken account into the calculation. We can interpret the data in terms of 'exchange chains' although the density of atoms my be below the 3D percolation limit, the intergranular layers are so thin that it is possible that a number of chians will exist which connect the grains via exchange coupling. When the density of the doping atoms is low, such exchange chains crossing the thickness of the film are unlikely, so that the effective exchange coupling between the two layers is weak. For higher density, it can be seen that the restoring torque increases linearly with the angle of Magnetic Layer 2, and the rate of increase depends on the density of the free atoms. In other words, the higher the density, the larger the gradient. This can also be explained by the effective exchange coupling between the two layers: if the exchange is strong, the restoring torque should be proportional to the angle between the two layers, which is θ of Magnetic Layer 2 in Fig. 3.7.

The free energy of the system is an integration of the restoring torque over all the angles. From Fig. 3.8, it can be seen that the restoring torque depends on the density of the doping atoms for certain thickness of the spacer. Naturally we would like to know how the spacer thickness effects the exchange coupling. In order to understand the thickness effect, the exchange energy has been calculated by integrating the restoring torque of all the doping atoms in the spacer as a function of the thickness of the spacer layer:

$$\mathcal{F} = \int_{\theta} \tau d\theta = \int_{\theta} \sum_{i} \mathbf{S}_i \times \mathbf{H}^i_{\mathrm{ex}} d\theta \tag{3.4}$$

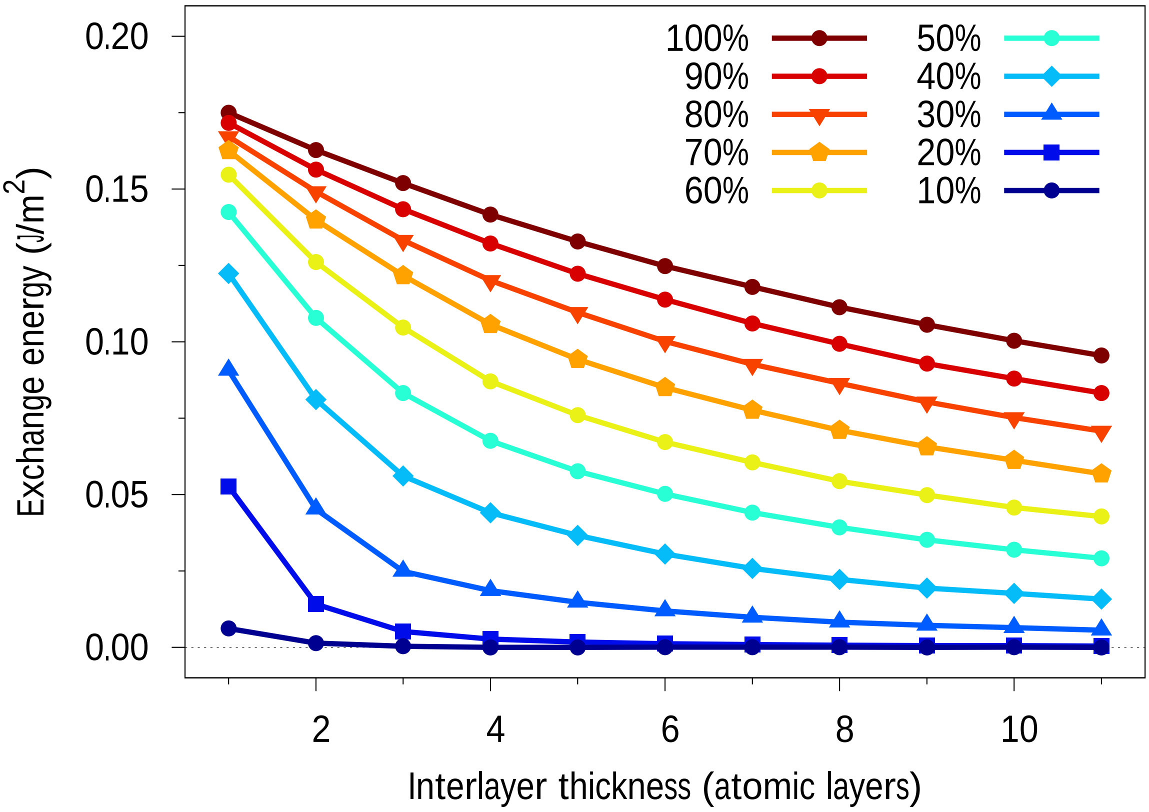

Figure. 3.9: Exchange energy as a function of the number of the monolayer of the spacer between Magnetic Layer 1 and Magnetic Layer 2 in Fig. 3.7, the curves in different colours referring to varying density from 10% to 100% of the doping atoms within the spacer.

Fig. 3.9 shows the exchange energy as a function of thickness, for density of the atoms varying from 10% to 100%. Again, for very low density of the doping atoms such as 10%, only when the spacer is one monolayer, there is exchange coupling. We can interpret the results in terms of 'exchange chains' which represent a percolation across the thickness of the film. Because the film is thin, percolation might be expected to occur at densities lower than 3-D percolation limit. This can be understood for one monolayer spacer, if some atoms are added, the exchange chains coupling the two grains can be established and therefore the exchange coupling is not zero. However, when the spacer thickness is increased, the exchange chains are too short to link the grains. So the darkest blue curve in Fig. 3.9 only has the non zero data at 1 monolayer and all the values of exchange energy for more monolayers are all zero. This exchange chains theory can also be used to explain the decrease of the exchange coupling with increasing thickness of the spacer for higher density. We can interpret the result s of Fig. 3.8 in terms of the development of exchange chains, which will be more prevalent at high densities.

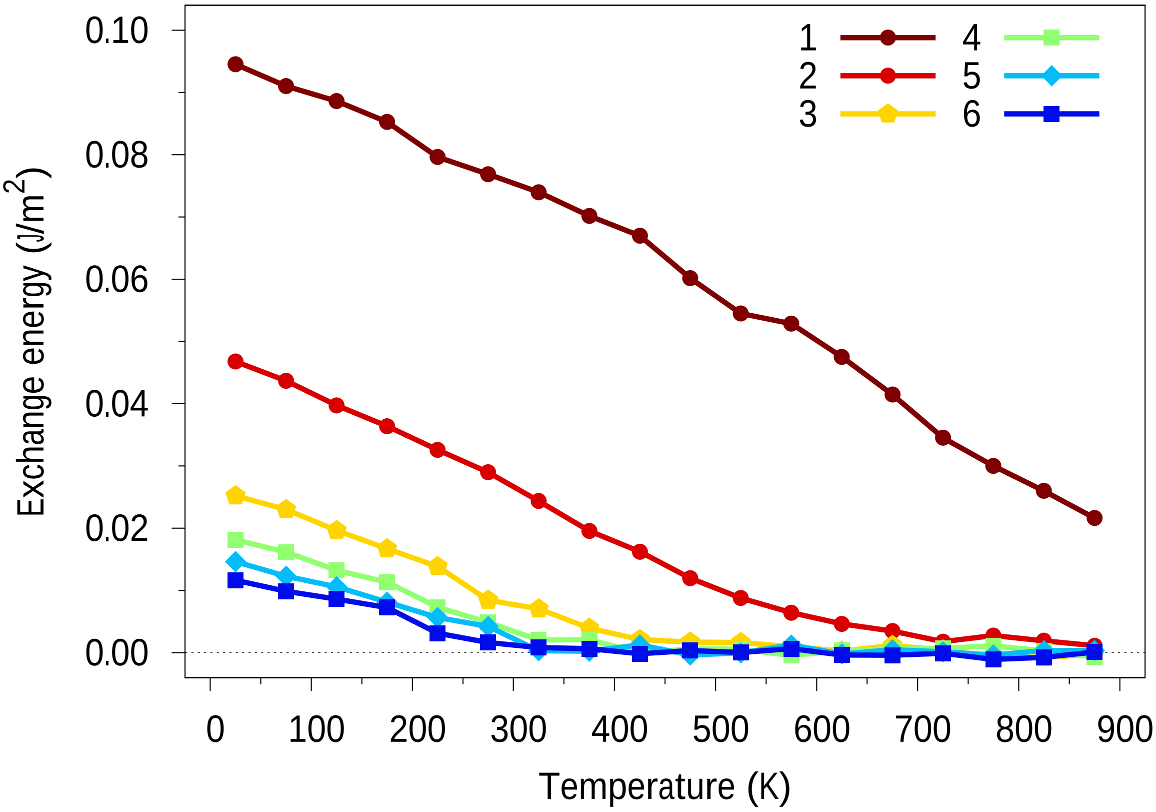

Figure. 3.10: Exchange energy as a function of temperature, for different number of monolayers of the spacer, varying from 1 to 6 monolayers.

Last but not least, thermal effects are introduced into the exchange energy calculation. Fig. 3.10 shows the temperature dependent exchange energy for different thickness of the spacer. For very thin spacer such as 1 monolayer, the exchange energy decreases almost linearly from 0.095 J/m^2 at zero Kelvin to 0.025 J/m^2 at 900 Kelvin. While for thicker spacer, for 2 monolayers to 6 monolayers, the exchange energy will decrease along with the increasing temperature, and approaches zero at a particular temperature. The thicker the spacer, the lower this particular temperature which always is lower than Tc. The temperature dependent exchange energy illustrates the thermal effects on the doping atoms within the spacer. The number of the nearest neighbours of the doping atoms is less than those in the bulk because of the missing atoms. Therefore the exchange is weaker within the spacer and so is the thermal stability. For thicker spacer, the exchange chains do not couple the grains effectively relative to those in a thinner spacer, so the exchange energy is lower at the same temperature and approaches zero at lower temperature, compared to the thinner spacer.

3.2.2 *Atomistic modelling of CoPt grains with doping magnetic atoms in the intergranular layer*

The Monte Carlo calculation gives a way to study the exchange energy between two magnetic grains coupled by doping atoms within the spacer between them. Furthermore, in order to understand how the inter-granular exchange coupling effects the reversal processes and the coercive fields, an atomistic model is used to calculate the spin dynamics of a granular system as shown in Fig. 3.11: 7 CoPt grains are considered as in Fig. 3.1, however the oxide spacer is doped by some ferromagnetic atoms. The grain size is 5 nm and 5 nm thickness, and the spacer is 1 nm. The density of the doping atoms varies from 0% to 100%. A LLG equation is used to calculate the spin dynamics, using the Heisenberg exchange model to calculate the exchange coupling, and also the thermal effect is taken account into by using the Langevin dynamics.

Fig. 3.12 presents the coercivity as a function of the density of the doping atoms at zero temperature. The magnetocrystalline anisotropy K_u of the doping atoms varies from 0 to the bulk value. It can be seen that when the K_u of the doping atoms is very small, such as zero, and those less than of 1×10^{-23} Joules, the coercivity curve shows a decrease to a value determined by the anisotropy of the impurity atoms. While when the anisotropy of the doping atoms is increased to 2.3×10^{-23} Joules, the coercivity as a function of density curve decreases quickly to a minimum value at 30% and then increases slightly with the increasing density of the doping atoms. For very high value of $K_\mathrm{u} = 4.6 \times 10^{-23}$ Joules, the coercivity maintains a very high value, larger than 7 Tesla and does not vary with the density.

In order to look at the dynamics of the reversal processes of this system, we

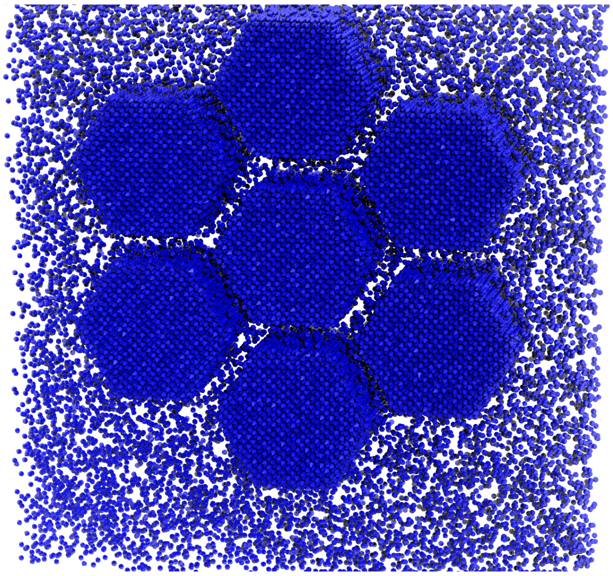

Figure. 3.11: The schematic diagram of the CoPt grains with doping magnetic atoms in the spacer.

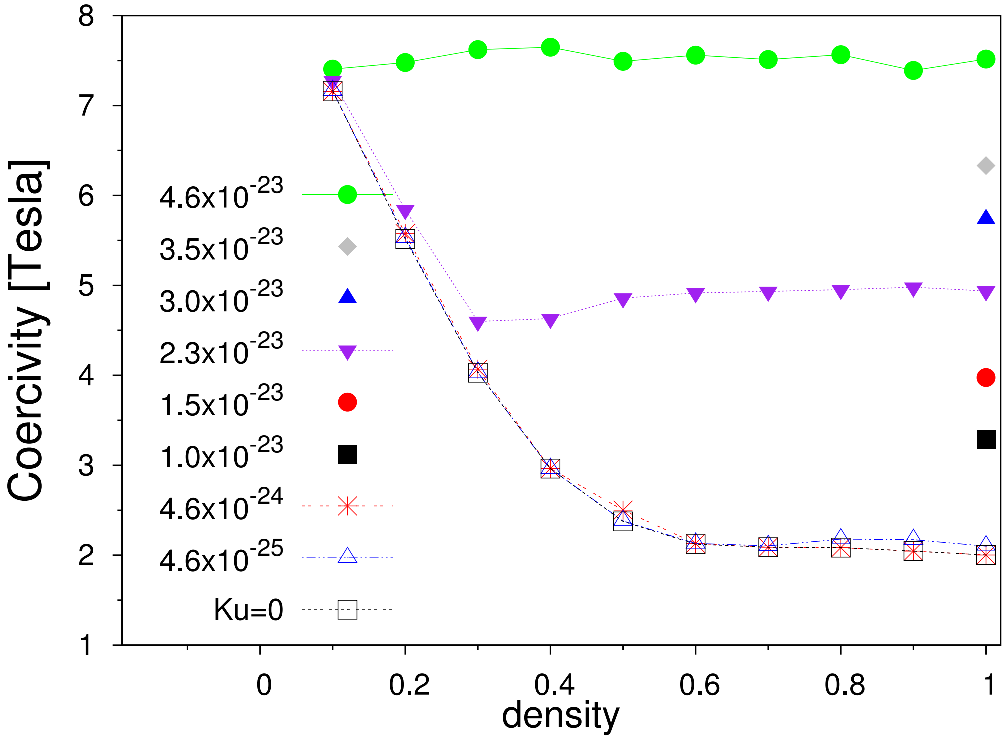

Figure. 3.12: Coercivity at Zero Temperature as a function of the density of the doping atoms in the spacer between grains, for different magnetocrystalline anisotropy constants.

choose (a): $K_\mathrm{u} = 0$ and (b): $K_\mathrm{u} = 2.322 \times 10^{-23}$ Joules (Fig. 3.13) to plot the hysteresis loops. In Fig. 3.13(a), when the inter-granular exchange coupling is weak (10%) since the density of the doping atoms is small (10%), a large step can be found in the red colour hysteresis loop which refers to the reversal of the doping atoms because of the smaller anisotropy. Afterwards the CoPt grains reverse and exhibit a larger coercivity. For higher density, this difference between two switching fields (doping atoms and CoPt grains) is reduced because the inter-granular exchange is getting stronger. And this also results in a reduction of the coercivity of the whole system. Fig. 3.13(b) shows the hysteresis loops of the whole system with a higher anisotropy $K_\mathrm{u} = 2.322 \times 10^{-23}$ Joules of the doping atoms. Again for the lower density such as 10%, a step is still obvious in the red colour hysteresis loop indicating the reversal of the doping atoms, but the switching field is larger according to the larger anisotropy of the doping atoms. Furthermore the step decreases with the increasing density of doping atoms, as well as the coercivity of the whole system. This originates from the stronger inter-granular exchange coupling. For a density larger than 30%, the purple triangle points in Fig. 3.12, the coercivity of the whole system increases a little, which is because of the stronger anisotropy of the doping atoms changing the reversal mode of the grains. The reversal of the grains starts with the nucleation of a perpendicular domain which propagates causing reversal of the CoPt grains. At higher values of the density, the nucleation and the propagation of this domain wall is inhibited by the CoPt grains, and so the coercivity reduction is less pronounced.

The thermal effects are also taken account into the calculation: Fig. 3.14 repeats the calculation in Fig. 3.12 but at room temperature. The thermal effect is simulated by using the Langevin dynamics. Fig. 3.14 shows that the thermal fluctuation reduces the coercivity for all the cases of different density and anisotropy of the doping atoms. The decrease of the coercivity with increasing density is more obvious for lower anisotropy such as $K_\mathrm{u} = 0$, the coercivity decreasing from 3.8 Tesla to 1.2 Tesla. While for $K_\mathrm{u} = 2.3 \times 10^{-23}$ Joules, the coercivity is reduced from 3.8 Tesla to 2.5 Tesla. However, for higher anisotropy $K_\mathrm{u} = 4.6 \times 10^{-23}$ Joules, the coercivities at 10% and 100% are almost the same, only with a fluctuation at 50% and 60%. This result shows the density of the doping atoms with lower anisotropy will reduce the system coercivity at room temperature and thermal effects can also be found in the calculation.

From Fig. 3.14, it can be seen that when the density of the doping atoms is less than 0.4, the coercivity curve is flat and keeps a constant value. This is because when the density is low, the exchange chains mentioned previously is weak and can be easily destroyed by the thermal fluctuations. When the density

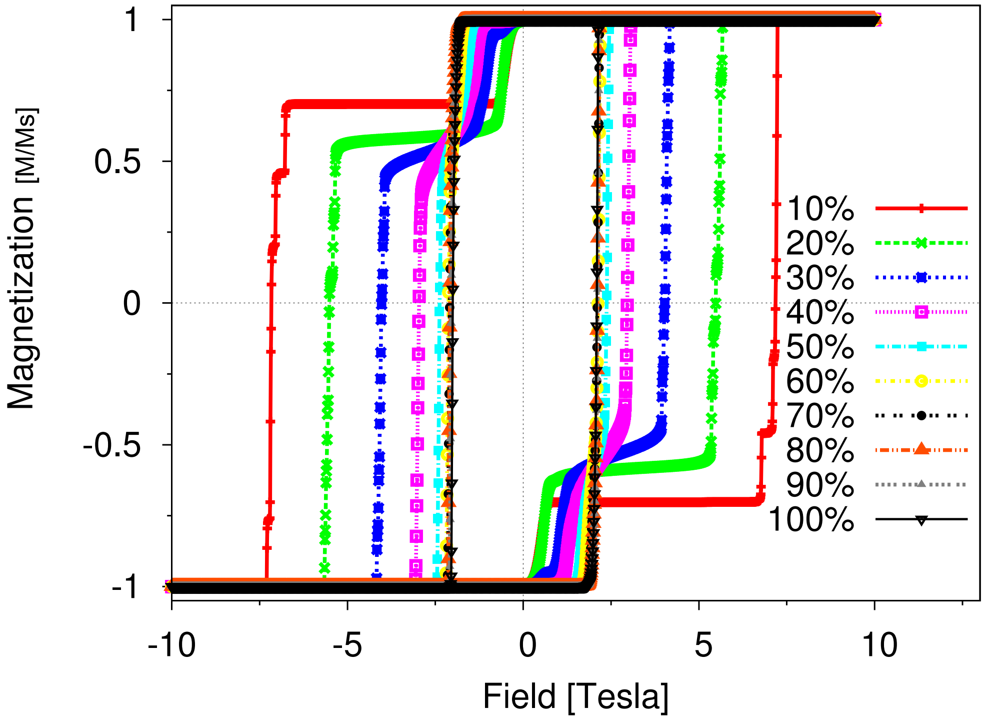

(a) $K_\mathrm{u} = 0$

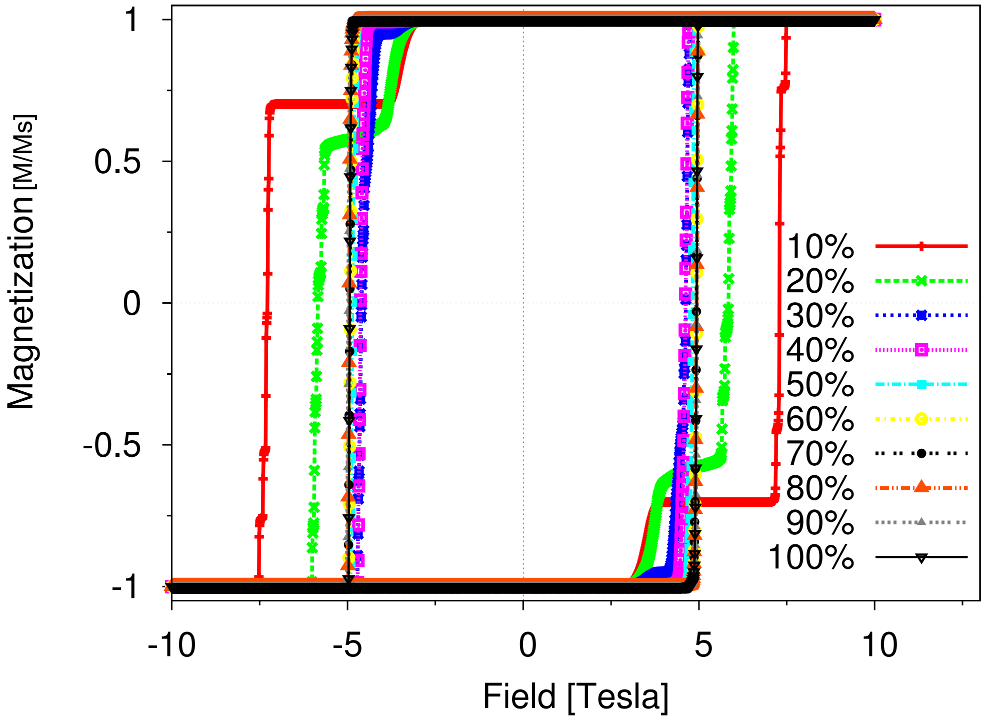

(b) $K_\mathrm{u} = 2.322 \times 10^{-23}$ Joules

Figure. 3.13: Hysteresis Loops for different density and anisotropy of the doping atoms. (a): $K_\mathrm{u} = 0$; (b): $K_\mathrm{u} = 2.322 \times 10^{-23}$ Joules

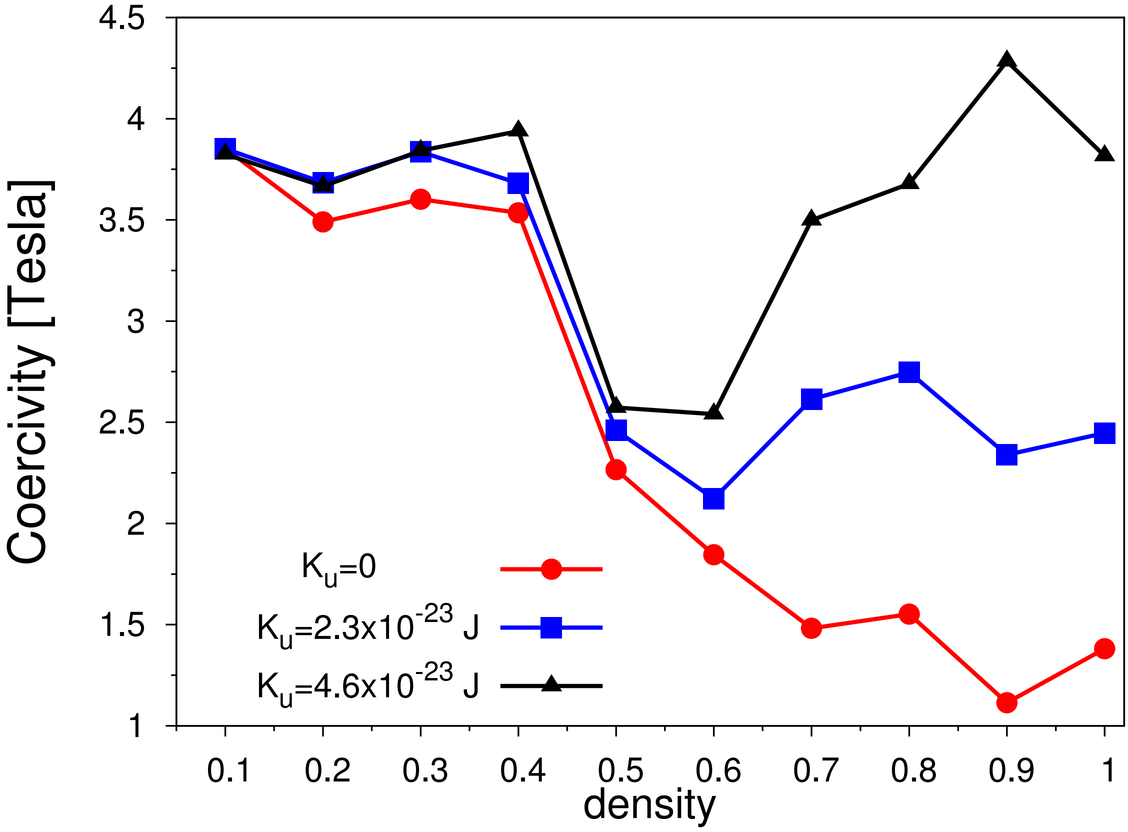

Figure. 3.14: Coercivity at Room Temperature (300 Kelvin) as a function of the density of the doping atoms in the spacer between grains, for different magnetocrystalline anisotropy constants of the doping atoms.

is higher than 0.4, the increase of the density has an effect on the coercivity because the exchange chains transfer the inter-granular exchange coupling and thus reduce the coercivity: for doping atoms with zero anisotropy, the coercivity is decreased from 3.5 Tesla to around 1 Tesla; for a higher anisotropy, the decrease of coercivity is less than that of zero-anisotropy; for a bulk value anisotropy, the decrease of the coercivity is much less pronounced, and the coercivity increases after the minimum at 0.5 and 0.6. This is because when the density is lower than 0.4, the exchange chains are too weak to link the grains. When the density is increasing, these exchange chains getting stronger, the coercivity is reduced due to the thermal fluctuation on these exchange chains. However, because the doping atoms has a very high anisotropy, when the density is continously increasing, the coercivity is again increasing until the bulk coercivity at 1.0 when the grains are connected to be a large bulk.

3.2.3 summary

In this section, a Monte Carlo method is used to calculate the restoring torque and the exchange energy of a system with two constrained magnetic layers coupled by some free atoms within the spacer of the two layers, to find the exchange coupling increases with the density of the doping atoms and decreases with the spacer thickness. The temperature dependent exchange energy is also simulated, indicating the thermal fluctuation has a larger effect on the exchange energy especially for thicker spacer. Furthermore, an atomistic model is used to calculate the hysteresis loops and the coercivity of a granular CoPt layer with doping atoms between the grains. The density of the doping atoms will reduce the coercivity of the whole system if the anisotropy of the doping atoms is small. It is worthy to mention that when the anisotropy of the doping atoms is less than 1×10^{-23} Joules, the coercivity can be reduced from higher than 7 Tesla to 2 Tesla with a density of 60%.

3.3 Conclusion

In summary, this chapter studies the inter-granular exchange coupling in a granular media. The first section gives a way to control the exchange coupling through a continuous capping layer on a granular layer whose grains are decoupled by very thick oxide spacer. The granular-continuous coupled system shows optimised interfacial exchange parameter is important to recude the coercivity. The second section calculates the exchange energy by using a Monte Carlo method and also an atomistic model, to further understand the inter-granular exchange by adding free ferromagnetic atoms into the spacer between grains in a granular media. This results tell the nucleation of exchange chains is the main resource of coupling between the grains.

4. Atomistic Modelling of Ultrafast Field Cooling Processes of Magnetic Recording Media

The reversal process during ultrafast field cooling is investigated by using an atomistic model. The physics in the vicinity of the Curie Temperature of a recording medium is studied by addressing the time, temperature and field dependence. An analytical result also demonstrates that the HAMR process is analogous to an ultrafast field-cooling process. In addition, a full HAMR process is demonstrated by writing several bit transitions to a realistic granular recording medium.

4.1 Introduction

The magnetic recording industry has been dramatically increasing in volume for several decades. The main challenge in designing the magnetic recording media is to overcome the magnetic recording trilemma, where increased recording densities lead to the use of high anisotropy materials to achieve thermal stability, because the volume of a single grains of the recording medium is getting smaller due to the requirements of a higher areal density of $TBit/in^2$ and beyond[43, 44]. Perpendicular magnetic recording using materials with very high perpendicular magnetocrystalline anisotropy such as Iron Platinum or Cobalt Platinum aims to long term thermal stability by maintaining a stable anisotropy-to-thermal energy ratio KV/k_BT at around 60. However, the large K gives rise to switching fields beyond those achievable by a conventional write head.

Heat Assisted Magnetic Recording (HAMR) is a potential solution which uses a laser as a heat source to reduce the coercivity of the medium during writing. There are several critical problems worthy to be studied during the cooling process when the laser is applied and switched off: heat delivery, endurance and the reversal mechanism. Several engineering challenges relate to the light delivery system. B. Challener, et al [45, 46], present a possible solution using surface plasmons in their HAMR head to focus a light beam below the diffraction limit. The complicated physics in vicinity of Curie Temperature (T_C) has also been studied in micromagnetic scale by the Landau-Liftshitz-Bloch (LLB) equation [47, 48, 49, 50, 51]. The existence of a so-called linear or elliptical reversal mechanism is also reported [52, 53]. However, how several factors in a HAMR process, such as temperature, heating time, applied field and grain size, affect the recording process, has not been deeply studied. In this chapter, an atomistic model is used to simulate the field, time and temperature dependent reversal process, which helps to understand the ultrafast magnetisation dynamics. Furthermore we also simulate a magnetic write process, writing several bits of data to a realistic granular recording medium.

4.2 Ultrafast field cooling processes of a heat assisted magnetic recording medium

In a HAMR process, there are two stages during a laser pulse: the heating process and the cooling process. In order to study the cooling process separately, firstly we assume all the spins in a recording grain have been equilibrated from the same temperature for long enough time. And then the grain is cooled down to room temperature at different rates. In the meantime, an external field is applied to the grain during the whole process. This research will tell us how the equilibrium temperature, the cooling rate and the applied field effect the reversal of recording grains.

A single FePt grain is firstly studied by using an atomistic model described in Chapter 2, to investigate the magnetic properties during the HAMR process. The grain-size is 5 nm (diameter) with a thickness of 8 nm which is close to the size of real recording particle in application. The FePt-FePt exchange coupling parameter is 3.0×10^{-21} Joules, and the magnetisation saturation is 2.38 Bohr magneton (μ_B), and the perpendicular magnetocrystalline anisotropy parameters is 6.622×10^{-23} J/atom [54].

Fig. 4.1 shows typical hysteresis loops of a single grain at different temperatures. The black line shows the hysteresis loop at zero temperature, from which it can be seen at zero temperature, the saturation magnetisation is 1 (normalised magnetisation value) and the loop is very square with a large switching field. The blue line presents the hysteresis loop at room temperature (300 K). Both of the magnetisation and the switching field are reduced: the magnetisation is around 0.8 of saturation and the switching field is almost half of that at zero temperature. When the temperature is increased to 650 K (red line), the saturation magnetisation is reduced to 0.25 and the switching field is also reduced to very small value (0.5 Tesla). From this result it can be seen, the temperature has two effects on the grain, one is to reduce the magnetisation, and another is to reduce the switching field. Generally the switching field is thought to be proportional to the anisotropy constant of the grain, which is also temperature dependent.

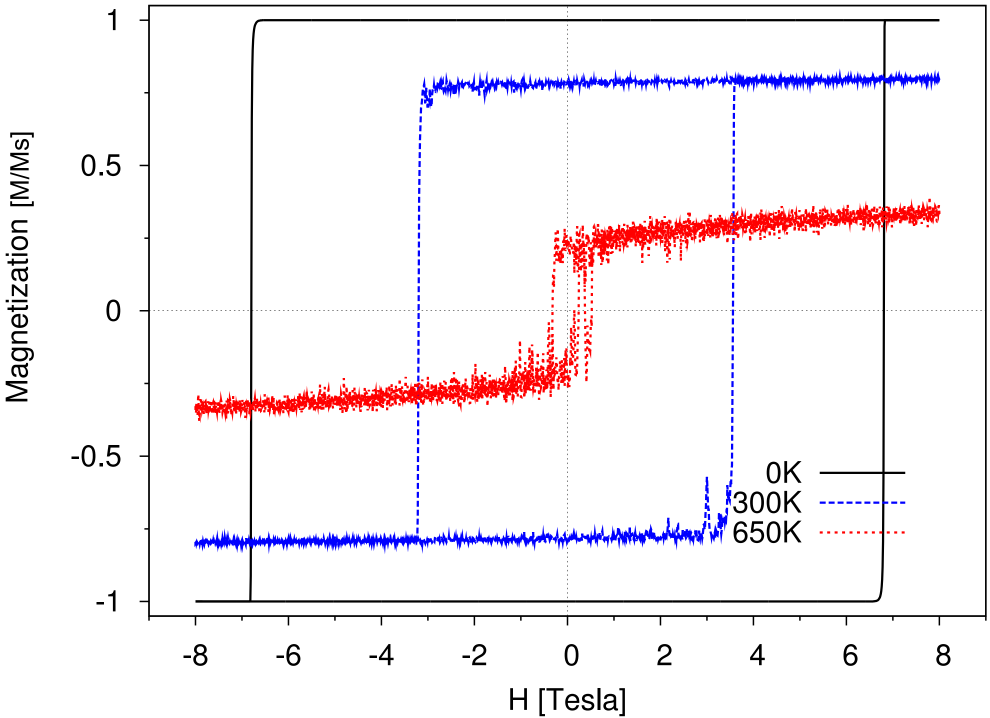

Figure. 4.1: Hysteresis loops of a single grain at three different temperatures: 0 K (black), 300 K (blue) and 650 K (red).

The simulation results of M/M_S and K/K_0 is shown in Fig. 4.2: the magnetisation decreases with the increasing temperature and reaches zero around Curie Temperature (T_C). The anisotropy decreases linearly with the temperature and no more data can be gained beyond T_C because the magnetisation is reduced to zero.

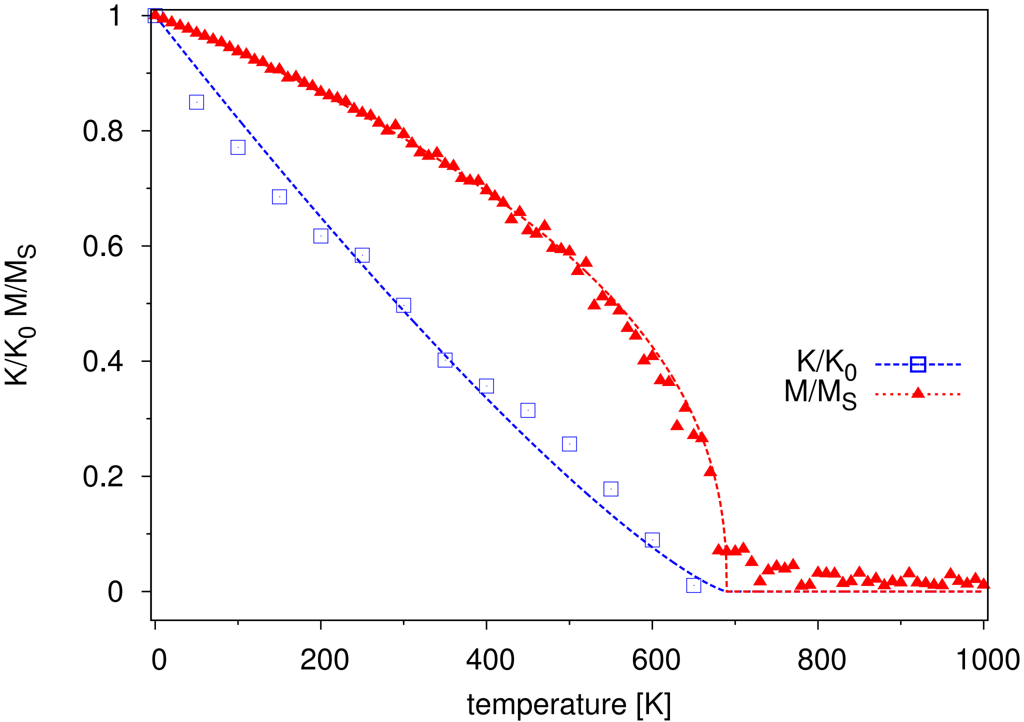

Figure. 4.2: The temperature dependent magnetisation M and magnetocrystalline anisotropy K of a 5nm single grain. Points: simulations results; Dashed lines: fitting curves

For temperatures less than the Curie Temperature (T_C), we fit the temperature dependent magnetisation and magnetrocrystalline anisotropy by using a power law function of temperature:

$$K(T) = m(T)^3 \tag{4.1}$$

where the temperature dependent magnetisation $m(T)$ takes the form:

$$m(T) = (1 - \frac{T}{T_C})^{0.42} \tag{4.2}$$

Combining Eq. 4.1 and Eq. 4.2, we get the temperature dependent K:

$$K(T) = (1 - \frac{T}{T_C})^{1.05} \tag{4.3}$$

The fitting results demonstrate the anisotropy constant K is very linear with temperature.

In order to simulate the statistical properties of the reversal process, we have used a system of 124 non-interacting hexagonal grains as shown in Fig. 4.3. The grain size is set at 5 nm and the material parameters are representative of FePt, with a Curie temperature of 690K and uniaxial anisotropy such that $KV/k_BT = 60$.

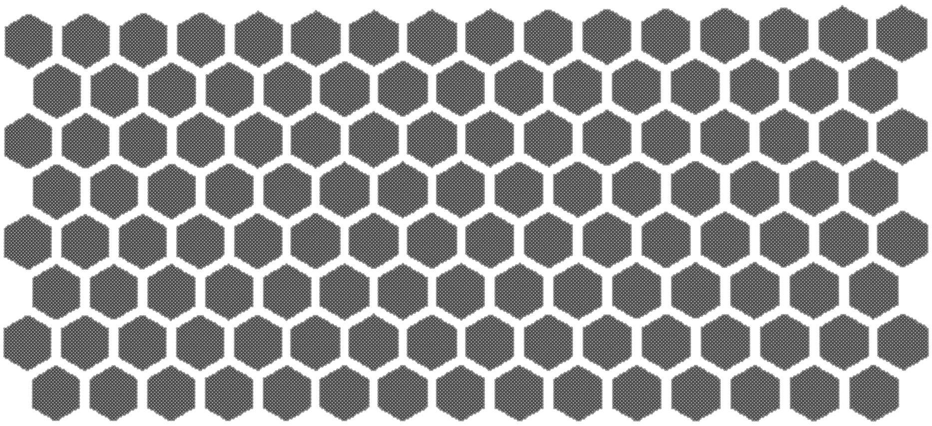

Figure. 4.3: Visualisation of the whole system.

A cooling process is simulated according to the time dependent temperature, shown in Fig. 4.4:

$$T(t) = T_R + (T_{max} - T_R) \cdot exp(-t/\tau) \tag{4.4}$$

where T_R is the room temperature (300 Kelvin), T_{max} is the peak temperature from which the temperature will be cooling back down to the room temperature.

τ is the cooling time, which varies from 10 ps to 500 ps, and t is the real time. The temperature is kept at peak temperature for a period of time (200ps) to make sure all the grains start from the same random state. The temperature reduces according to Eq. 4.4. The whole cooling process is continued for up to 1 ns. An external magnetic field is applied in the opposite direction ($-z$ direction) to the initialized direction, with an angle of 5 degrees between z direction. This applied field, which varies from 0.001 Tesla to 0.8 Tesla, is added for the whole cooling period.

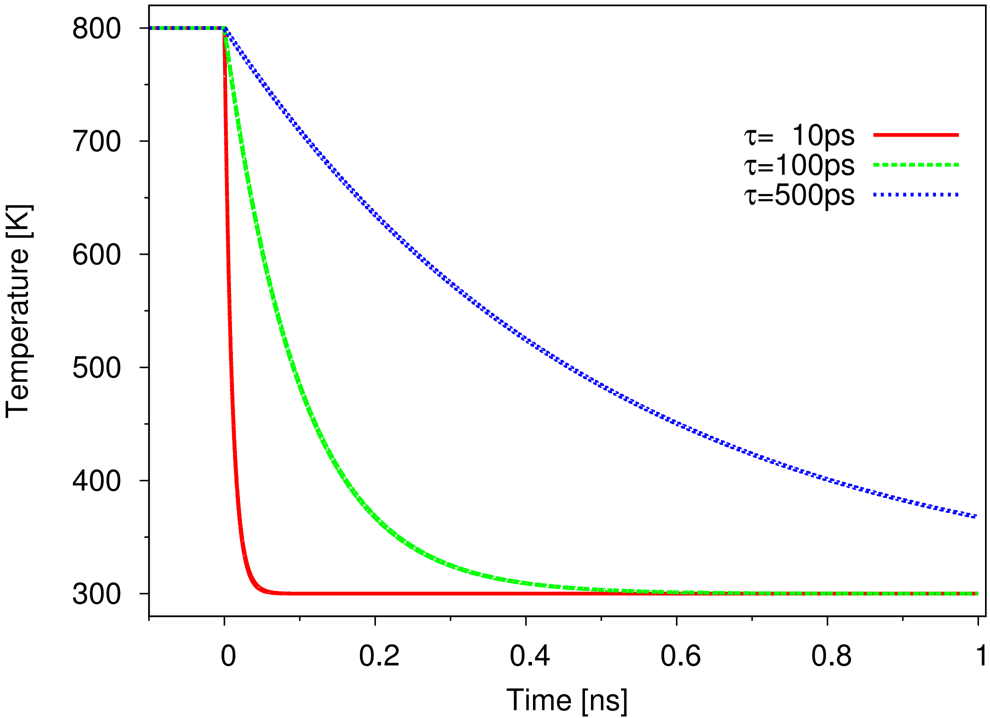

Figure. 4.4: Temperature performance for different cooling rates, according to Eq. 4.4.

During this cooling process, several parameters become critical elements effecting the magnetic reversal and other properties of the grains, such as the applied field, the cooling time and the peak temperature. Therefore in the following sections, we have varied these elements independently to study how they effect the cooling process.

4.2.1 Applied Field

Firstly, the effect of applied field is studied. According to the thermal activation law [18], the switching time is proportional to the exponential of $\Delta E_{total}/k_B T$, where $E_{total}(\theta) = -MHVcos(\theta) + KVsin^2(\theta)$. And ΔE_{total} is the energy barrier. θ is the angle between the magnetisation and the easy axis. The anisotropy energy is symmetric and has a maximum at the hard axis. The field reduces the energy barrier to reversal, allowing switching by thermal activation processes.

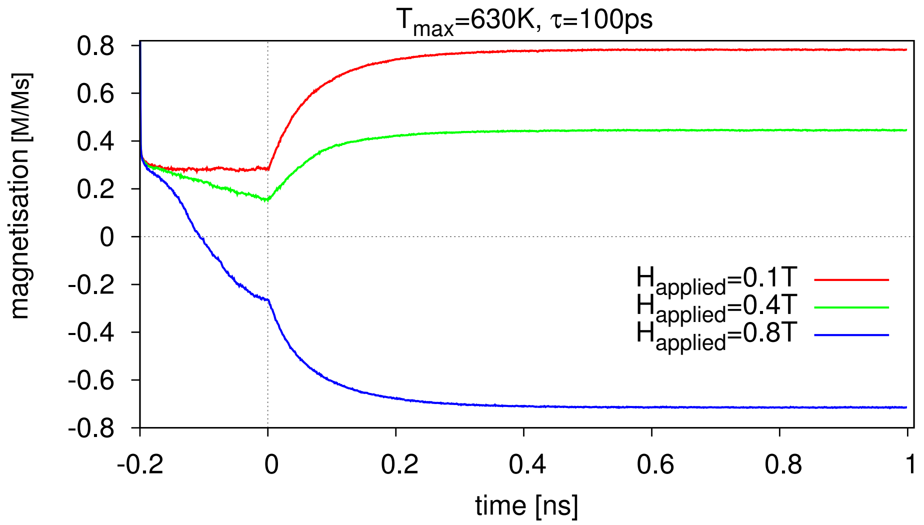

(a) $T_{max} = 630K$

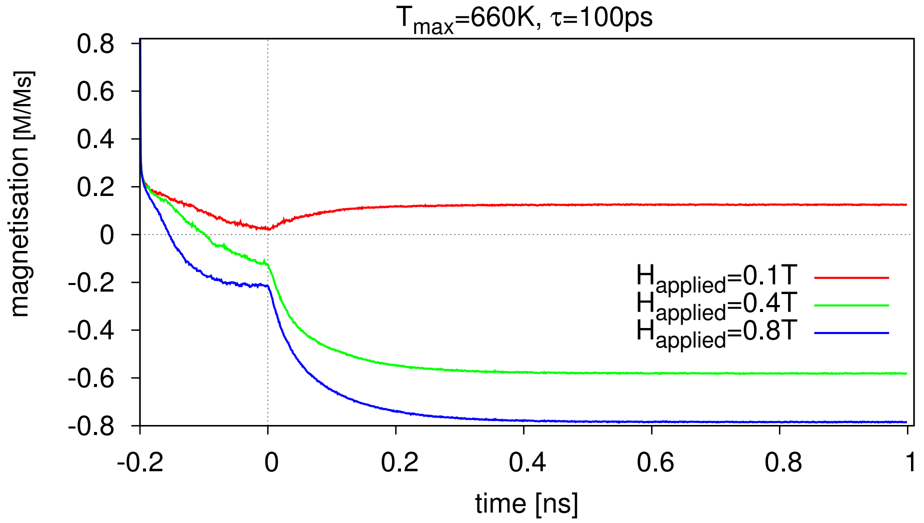

(b) $T_{max} = 660K$

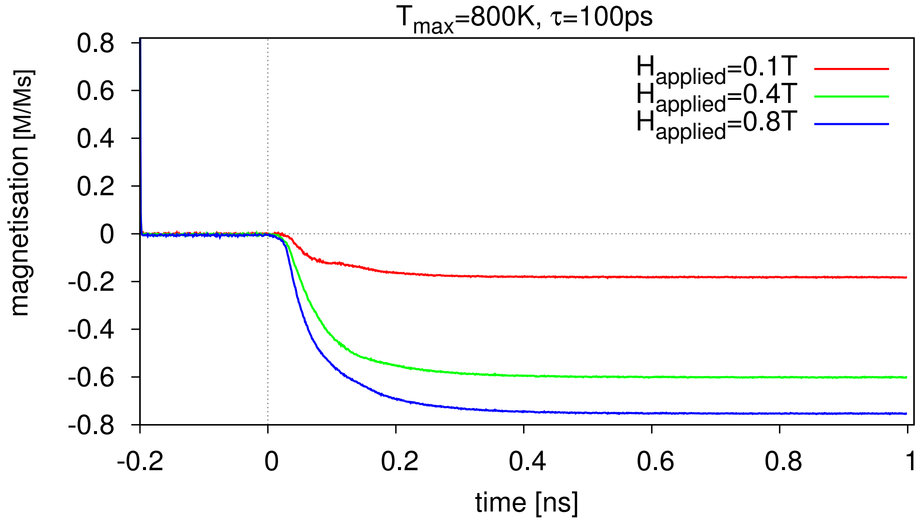

(c) $T_{max} = 800K$

Figure. 4.5: The time dependent z component of the magnetisation with fixed $\tau = 100ps$, varying H_{app}, for different peak temperatures: 630K (a), 660K (b), and 800K (c).

Fig. 4.5 presents the average of the z component of the magnetisation of all the grains as a function of time, for different applied field: 0.1 Tesla (red lines), 0.4 Tesla (green lines) and 0.8 Tesla (blue lines). In Fig. 4.5, the cooling rate $\tau = 100ps$, and the peak temperatures are 630K (Fig. 4.5(a)), 660K (Fig. 4.5(b)), and 800K (Fig. 4.5(c)), respectively. Fig. 4.5(a) shows the average magnetisation of all 124 grains as a function of time, when $T_{max} = 630K$ and $\tau = 100ps$. For small applied field 0.1 Tesla, the magnetisation firstly decreases to 0.35 and remains constant at this value during the first 200 ps because of demagnetisation process and the applied field. It then increases and finally recovers back to 0.78 as the temperature cools down to room temperature. For $H_{applied} = 0.4T$, the magnetisation is also decreased during the first 200 ps, to the lower value of 0.18. Again the magnetisation goes back to higher value when the cooling process starts. However, when the temperature is decreased to room temperature, the magnetisation does not return to the starting value of 0.78 but to 0.4, which means some of the grains are reversed in this case. When the applied field is larger, 0.8 Tesla, the decreasing curve of the magnetisation in the first 200ps passes across the zero line, which suggests that during the equilibration process, the reversal processes of the grains has started. When the temperature starts to decrease, the magnetisation does not recover but decreases further to a saturation value -0.7. In this case, it can be seen that more than half of the grains have reversed. It can be seen the larger the applied field, the more the magnetisation is reversed. This is because the applied field biases the energy barrier and forces the magnetisation to align in the same direction as the applied field. The reversal process happens during the first 200 ps time period, while the temperature is decreasing to the room temperature. Once the temperature achieves the room temperature, the magnetisation also approaches a flat value in the curve and no more grains reverse further.

Fig. 4.5(b) presents the effect of applied field on a field cooling process when the peak temperature is higher: $T_{max} = 660K$, and the cooling time keeps the same value $\tau = 100ps$. Therefore, for the first 200 ps equilibrium process, the temperature is higher and thus the magnetisation curves of both 0.4 Tesla and 0.8 Tesla cross the zero line, which means more than half of the grains have reversed during this period. Therefore when the temperature starts to cool down from zero time point, the magnetisations of both 0.4 Tesla and 0.8 Tesla fields are further decreased to -0.58 and -0.78, respectively. However the magnetisation of 0.1 Tesla case does not cross the zero line during the first 200 ps so it goes back to 0.2 after cooling down. Fig. 4.5(a) and Fig. 4.5(b) prove in a field cooling process, the effect of a negative applied field is to decrease the magnetisation and reverse the grains. Also the final average magnetisation of all the grains is depending on the first 200 ps equilibrium process: during which the reversal processes of the grains has already completed for large field cases.

The average magnetisation in Fig. 4.5(c) is kept at zero during the first 200 ps equilibrium process, because during this period the temperature is higher than the Curie temperature of the grains. When the temperature is cooling down, the magnetisation starts to reduce to negative values: more than half of the grains have reversed for a higher peak temperature case. The effect of the applied field is still to get more grains reversed and lower the magnetisation. When the temperature is higher than T_C, all the grains are completely demagnetised and the magnetisation is zero. In this case if an external field is applied on the grains, the energy barrier is biased by the applied field. Therefore the magnetisation of the grains tends to align along the direction of the applied field. The larger the applied field, the more grains reverse.

4.2.2 Cooling Rate

Fig. 4.6 compares the results of different cooling time τ, the applied field is 0.8 Tesla. Fig. 4.6(a) and Fig. 4.6(b) present the average magnetisation as a function of time, where the peak temperature $T_{max} = 630K$ and $T_{max} = 660K$, respectively. It can be seen for both figures, the magnetisation starts to reverse to a negative value during the first 200 ps equilibration process. When the temperature starts to cool down to room temperature, the magnetisation is further decreased to the same saturation value at different rates, which is depending on the different cooling time τ. This result proves the reversal process has been completed in the equilibration period, the number of reversed grains is the same in each case.

Fig. 4.6(c) shows a different result. First the magnetisation is kept at zero during the equilibrium process because of demagnetisation at a temperature higher than T_C. Afterwards, the magnetisation is decreased to different saturation values at different rates. For short cooling time $\tau = 10ps$, the magnetisation is decreased to -0.58, which means not all of the grains reverse. However for a slower cooling process $\tau = 100ps$, the magnetisation is decreased to -0.78, almost all the grains have reversed. It is also likely that if the $\tau = 500ps$ case is run for a longer time to get the temperature cooled down to room temperature, the magnetisation of the blue line will also be reduced to -0.78. According to this results, the effect of the cooling rate is to give the magnetisation enough time to climb over the energy barrier caused by the thermal activation when cooling from T_C. Since the peak temperature is 800K, the whole system is equilibrated at a temperature higher than Curie Temperature (T_C) and all the spins are thermally activated at a random state. If the temperature is cooling down very quickly, there is not enough time for the magnetisation of the grains to cross over the energy

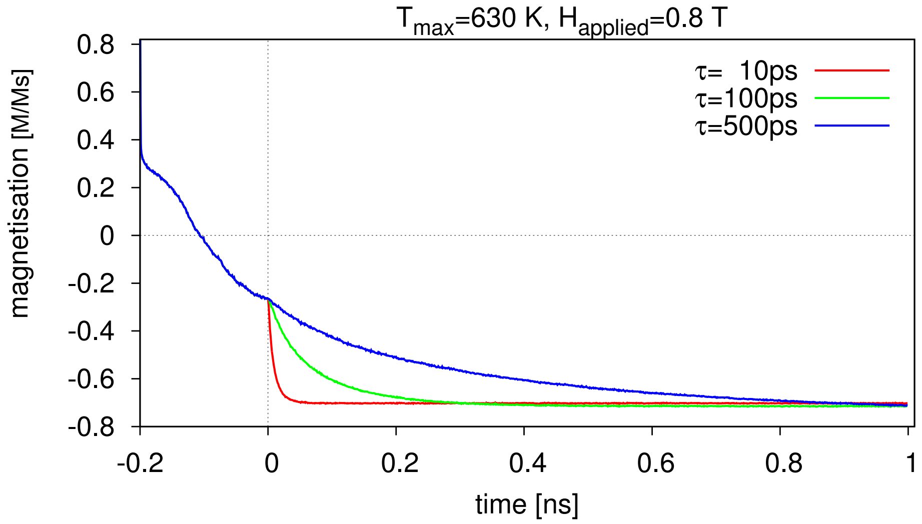

(a) $T_{max} = 630K$

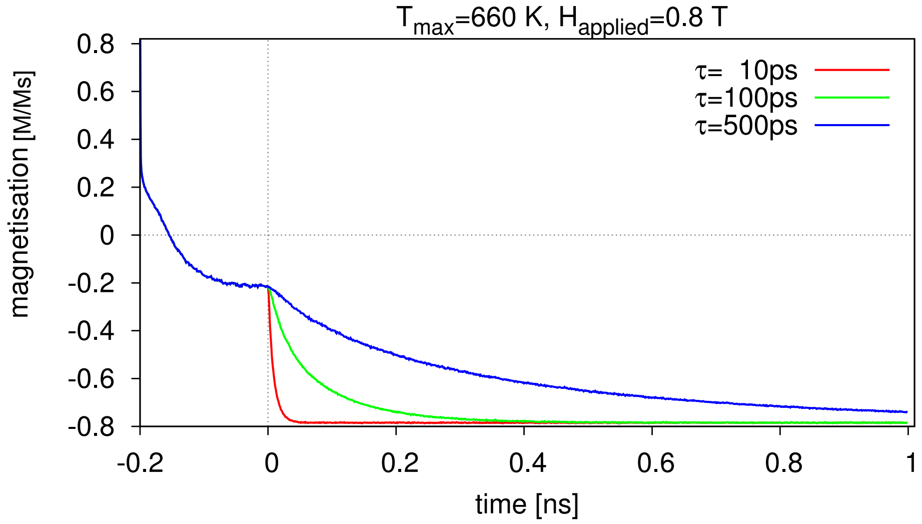

(b) $T_{max} = 660K$

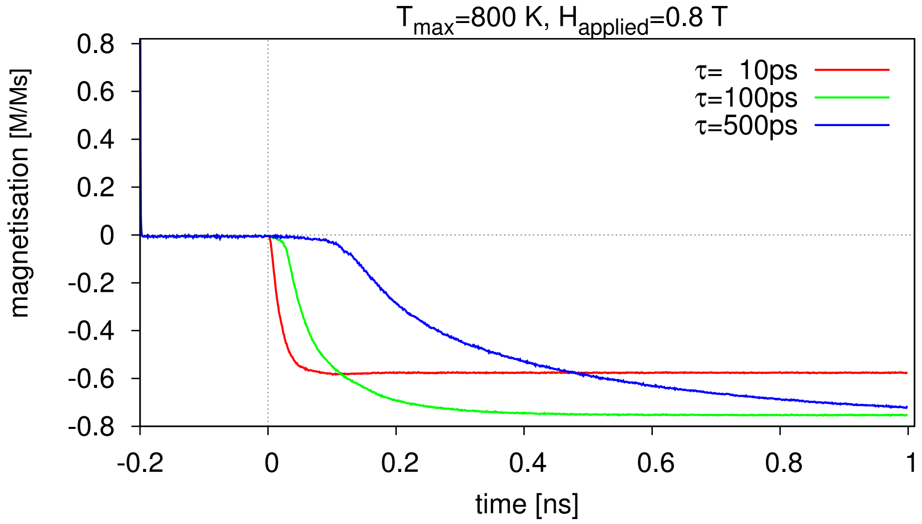

(c) $T_{max} = 800K$

Figure. 4.6: The time dependent z component of the magnetisation with fixed $H_{applied} = 0.8T$, varying τ, for different peak temperatures.

barrier between 0 degree to 180 degree. However for longer τ (100ps and 500ps), the temperature is cooling down slowly, the magnetisation has longer time to cross over the energy barrier so that more grains reverse. For cases whose τ are 10ps and 100ps, respectively, the 10ps case has a smaller negative Mz after the temperature is cooling down back to 300K because less grains are reversed during the faster cooling process. In addition, comparing the 100ps and 500ps cases, more grains are reversed during the cooling process for τ=500ps case because of the slower cooling rate. However the value of its magnetisation is slightly smaller than 100ps, this is because the temperature is cooling down too slowly that the temperature can't go back to 300K so that the thermal energy is higher of this case and results in a smaller magnetisation.

4.2.3 Peak Temperature

Furthermore, the average magnetisation for different peak temperatures has been studied, shown in Fig. 4.7. The applied field is fixed at 0.8 Tesla, Fig. 4.7(a) shows the results for $\tau = 10ps$ cooling from different peak temperature T_{max}=630K (red line), 660K (green line) and 800K (blue line), respectively. The magnetisation of all the cases has been decreased to negative values after the cooling process, which means most of the grains have reversed. Additionally, the average magnetisation of 800K has the smallest value when saturated. In comparison, the magnetisation of 660K is larger than that of 630K. According to this result, for the same applied field and very fast cooling time, the highest peak temperature which is higher than T_C does not reverse the most number of grains, but the temperature lower than T_C does. This still can be explained by the completion of the reversal process in the first 200 ps period when the peak temperature is lower than T_C. The higher the peak temperature, the more grains have reversed during this period. However when the peak temperature is higher than T_C, the magnetisation is completely demagnetised to zero during this period, and all the grains are at a random state. The reversal starts from the cooling process, while when the temperature is cooled down very rapidly, there is not enough time for all the grains to cross over the energy barrier, therefore the number of reversed grains is less and the average magnetisation is smaller when cooling from above T_C.

Fig. 4.7(b) and Fig. 4.7(c) present the effect of peak temperature on slower field cooling process, with $\tau = 100ps$ and $\tau = 500ps$, respectively. It can be seen, below T_C, the higher peak temperature has a larger magnetisation after cooling down to room temperature. The disadvantage of temperature higher than T_C is less for a longer cooling time, because in this case, the random grains have longer time to overcome the energy barrier and reverse. When the cooling time is as long as 500 ps, the final magnetisation has been decreased to almost the same value after the

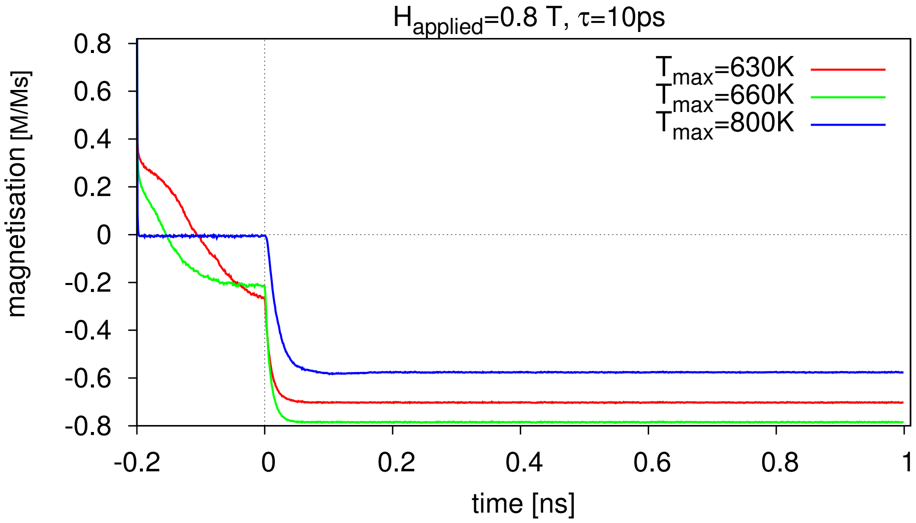

(a) $\tau = 10ps$

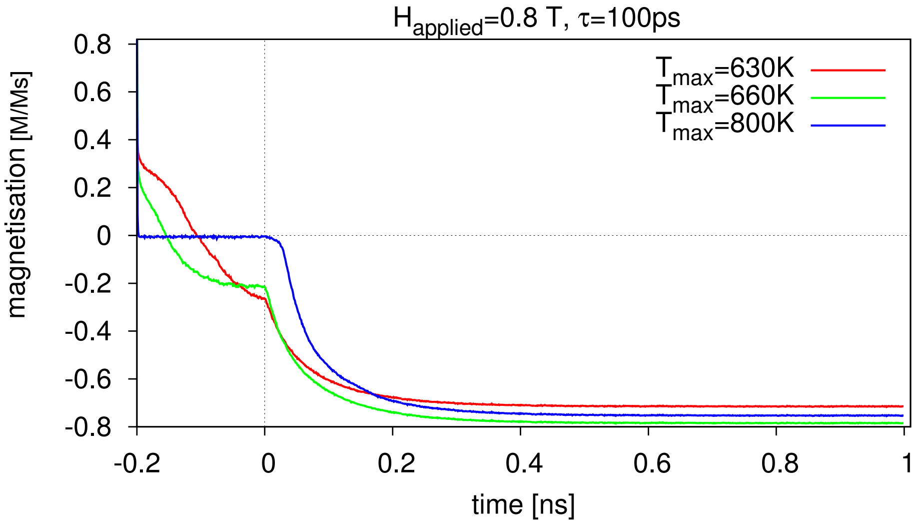

(b) $\tau = 100ps$

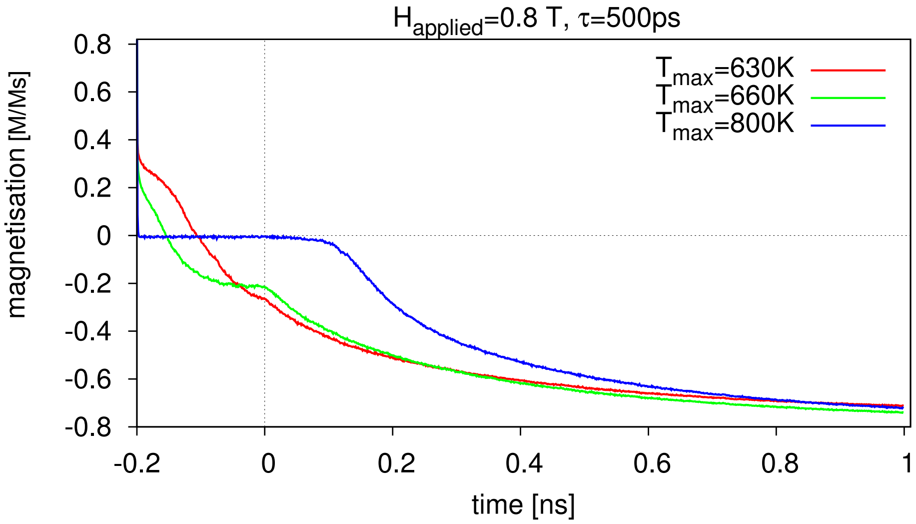

(c) $\tau = 500ps$

Figure. 4.7: The time dependent z component of the magnetisation with fixed $H_{applied} = 0.8T$, varying T_{max}, for different cooling times: (a) $\tau = 10ps$; (b) $\tau = 100ps$; (c) $\tau = 500ps$.

cooling process is finished.

In order to prove the assumption that the reversal process has been partly completed during the first 200 ps time, we have calculated the average magnetisation of 124 grains, when the temperature is kept at peak temperature (630K and 660K, respectively), under varied applied fields antiparallel to the direction of the initialized orientation of the magnetic moment of the grains. Fig. 4.8 shows for 630K temperature and 0.1 Tesla applied field, the magnetisation does not reverse during 1 ns time. While for 0.4 Tesla, the reversal happens at 400 ps and for 0.8 Tesla, the reversal happens at around 120 ps. For a higher temperature such as 660K, the reversal process has completed faster. In Fig. 4.9, the magnetisation has been switched at 60 ps when the applied field is 0.8 Tesla, and 120 ps for 0.4 Tesla. And the reversal time is little longer, around 300 ps for 0.1 Tesla applied field. These results demonstrate that during the first 200 ps period, the reversal process has completed for appropriate applied field and temperature: for 630K, a field as large as 0.8 Tesla is needed to finish switching in 200 ps time. While for a higher temperature 660 K, both 0.4 Tesla and 0.8 Tesla are enough to switch the magnetisation in the same time period. From this result it can also be estimated that if the grains are kept at peak temperature with an applied field for long enough time, rather than just 200 ps, the field cooling process will be different.

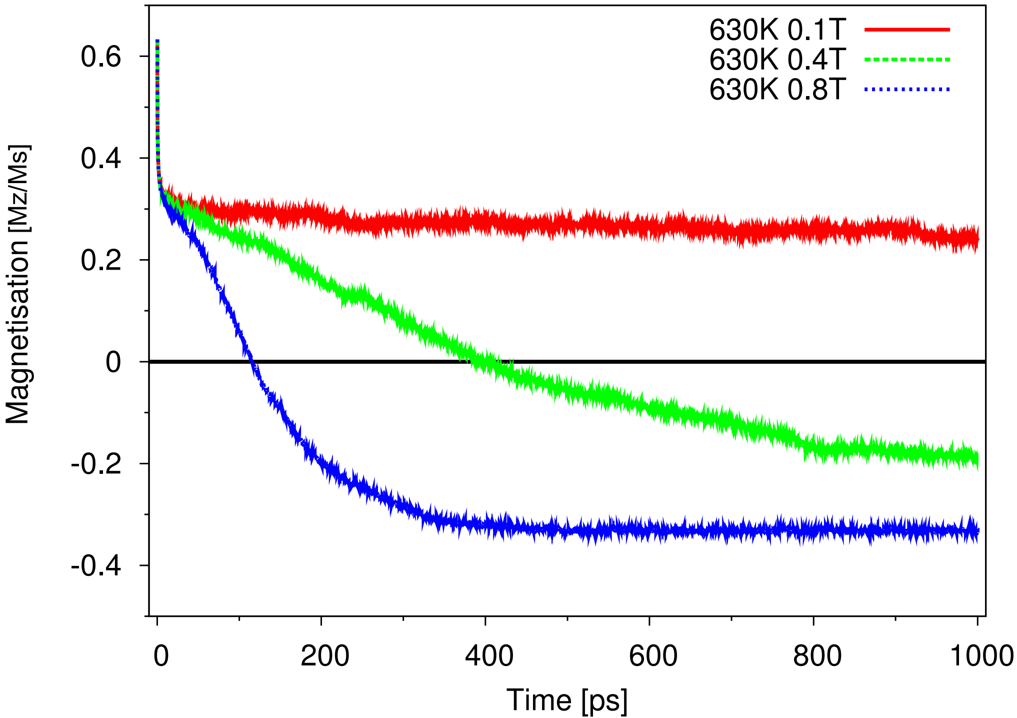

Figure. 4.8: Reversal time for grains when the temperature is kept at peak temperature 630 K, under varied applied fields.

To sum up, when the peak temperature is lower than T_C, the higher the peak temperature, the more grains have been reversed. However when the peak temperature is higher than T_C, the cooling time will play an important role,

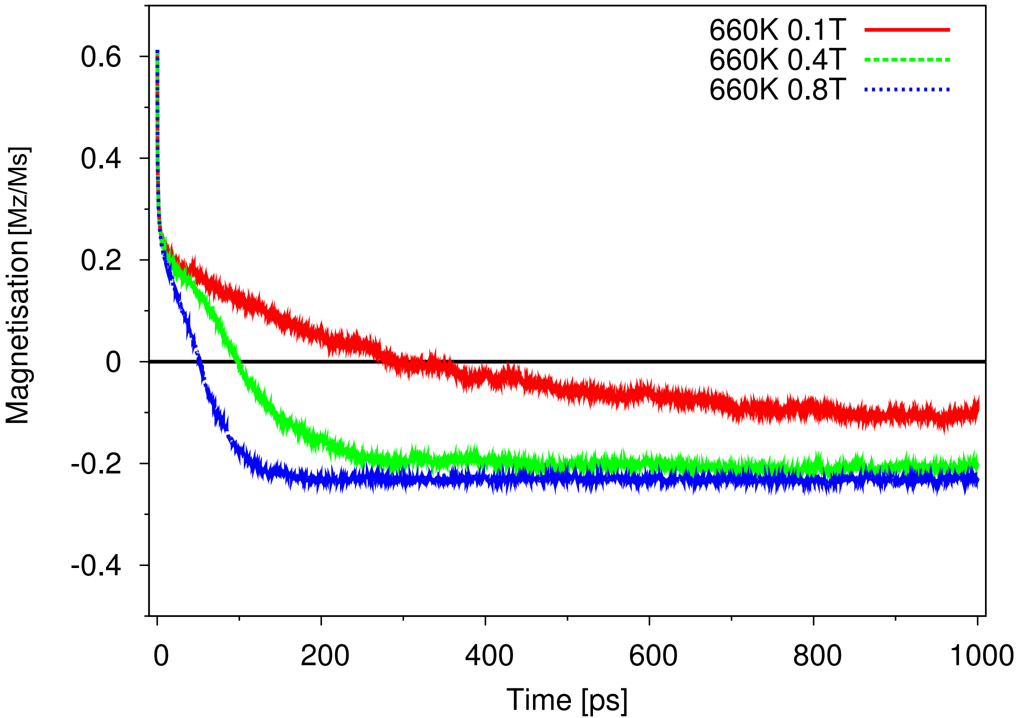

Figure. 4.9: Reversal time for grains when the temperature is kept at peak temperature 660 K, under varied applied fields.

to give the grains enough time reverse from random state to the direction of the applied field. It is noted that this is an idealised version of HAMR since in practice it is not possible to allow the system to equilibrate for 200ps in the reversing field. Essentially this process allows sufficient time for reversal by coherent rotation at relatively low temperature. Although not realistic for HAMR is also allows comparison with a single semi-analytical model as shown in the following section.

4.2.4 Grain Size

In order to study the performance of the field cooling process, a reversal probability has been defined:

$$p_{sw} = \frac{N_{reversed}}{N_{total}} \tag{4.5}$$

Where $N_{reversed}$ is the number of the reversed grains, and N_{total} is the total grain number. Fig. 4.10 presents the reversal probability as a function of grain size (the diameter of the grain). The peak temperature T_{max}=800K, and the applied field is 0.8 Tesla. The cooling time τ= 10 ps. The thickness of the grains is 5 nm and the energy barrier KV/k_BT is kept at 60. The diameter of the grains varies from 3nm to 7nm. It can be seen the reversal probability is lower for smaller grains, around 0.76 for 3 nm grains. Afterwards it increases to 0.95 for 5 nm grains, and when the grain size is increased to 7 nm, the reversal probability is 1. Evans, et al [9] has reported the probability p_{sw} that the magnetisation is switched into the correct state by the field during the attempt is to write the information, $P_{sw} = (m_e + 1)/2$, where m_e is the equilibrium magnetisation, taking the form:

$$m_e = tanh(\frac{\mu\mu_0 H}{kT}) \tag{4.6}$$

where $\mu = M_S V$ is the magnetic moment of the grain with M_S the material saturation magnetisation and V the particle volume. According to Eq. 4.6, the reversal probability is proportional to the grain volume, which has a good agreement with our results.

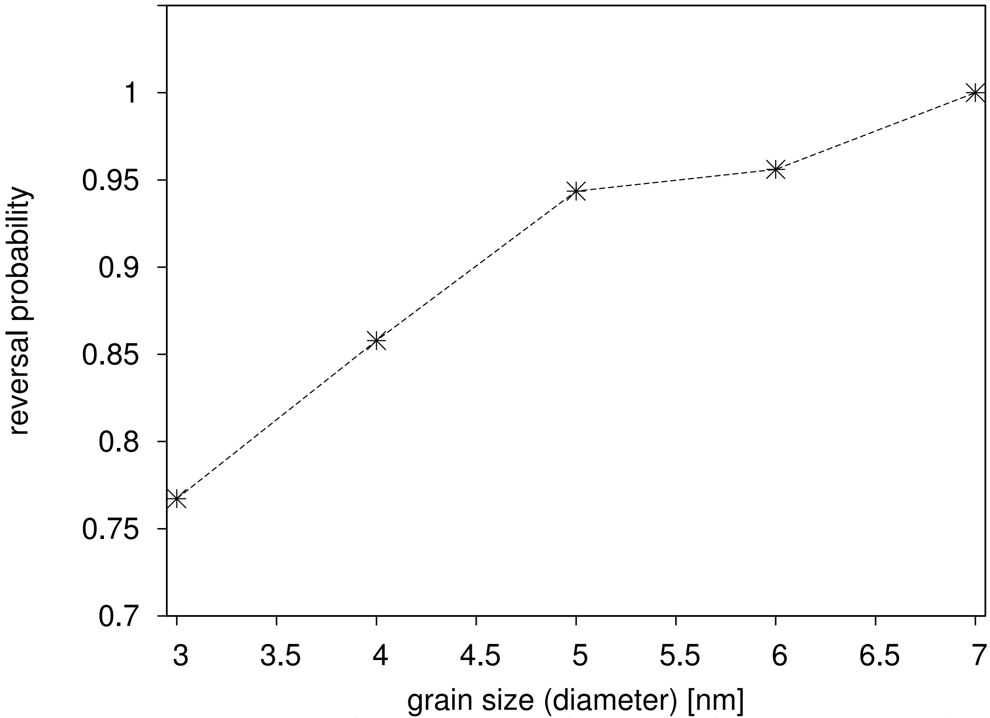

Figure. 4.10: Probability of reversal as a function of the diameter of the grains. $\tau = 100ps$, $H_{applied} = 0.8T$.

4.2.5 Angular Dependent Reversal Probability

Fig. 4.11 shows the angular dependent reversal probability for 5 nm diameter FePt grains, with different peak temperatures, the cooling time $\tau = 100ps$, and the applied field $H_{applied}$ = 0.8 Telsa. For a lower peak temperature such as 630K, the reversal probability increases when the angle is increasing from 0° to 10°, and then it slightly reduces when the angle is changing to 45°. This result can be explained by the Stoner-Wohlfarth model [55], which is a micromagnetic model widely used for single domain particles, the total energy having the form:

$$E = K_1 V sin^2\theta - \mu_0 M_S V H cos\theta \tag{4.7}$$

Where the first term is the anisotropy energy and the second term is the Zeeman energy. For small angle, the coercivity reduces with increasing of the angle, therefore the reversal probability is increasing. When the angle is continuously increasing, there is insufficient bias in the perpendicular direction - the $\mu H/kT$ [9] orient the magnetisation at a large angle, possibly lowering the reversal probability. When the peak temperature is higher, such as 660K and 800K, the difference of angle dependent reversal probability is less, because for the higher temperature, linear reversal is the main mechanism during the reversal process, and this reversal mode has less angular dependence. So the effect of angle, or the effect of the applied field, is not that apparent for higher temperature.

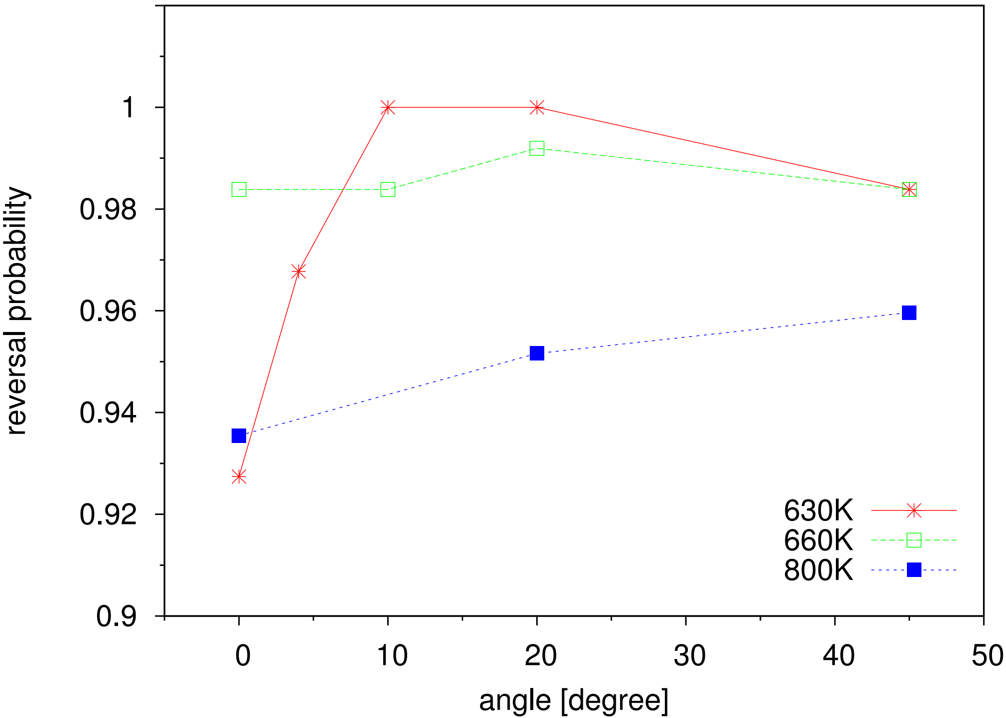

Figure. 4.11: Probability of reversal as a function of the angle between applied field and the easy axis, for different peak temperatures.$\tau = 100ps$ $H_{applied} = 0.8T$.

4.2.6 *Semi-analytical Model*

Fig. 4.12 shows the probability of reversal after the cooling process as a function of applied field. The peak temperature is 800 K. The points are simulation results which uses the atomistic model. According to Fig. 4.12, it can be firstly seen that the applied field has the largest effect on the probability of reversal. The reversal probability increases from 0.5 to almost 1.0 when the applied field is increasing from 0 to 0.8 Tesla. Secondly, the effect of τ is apparent: the faster cooling process with $\tau = 10$ ps has lower reversal probability, and the slower cooling processes with $\tau = 100$ ps and $\tau = 500$ ps have higher reversal probability. This is because the reversal process happens during the cooling process, while the magnetisation is demagnetized at the first 200 ps equilibration process. In this case, the cooling rate τ plays an important role in the reversal process, which decides whether the magnetisation of the grains have enough time to cross over the energy barrier. From the figure it can be seen, 100 ps is enough for the grains to reverse.

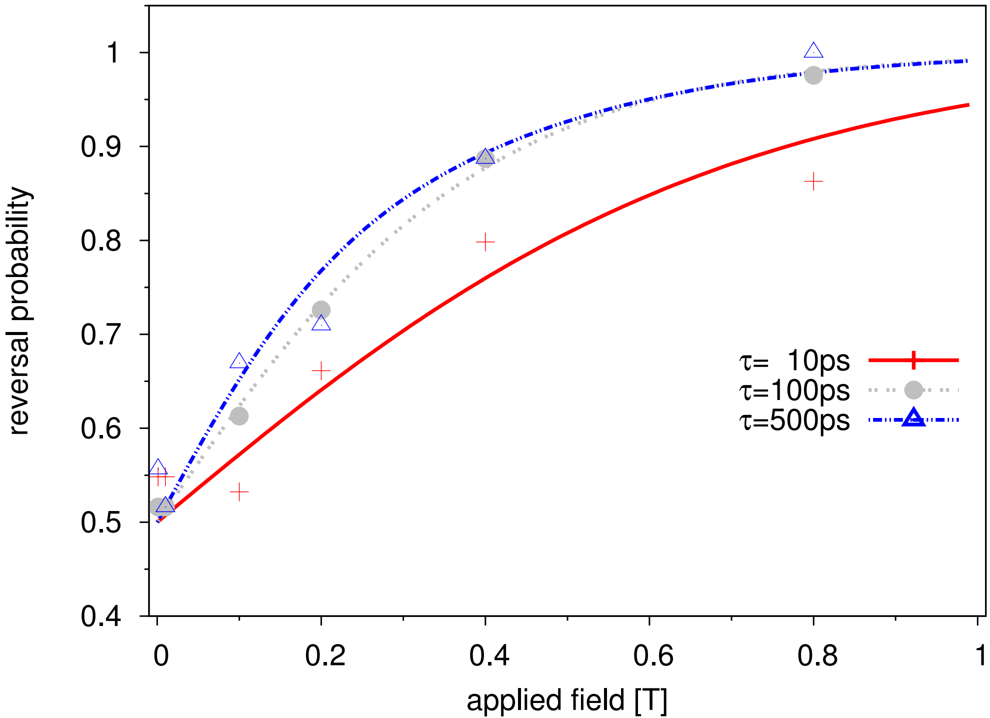

Figure. 4.12: Probability of reversal after equilibration as a function of applied field, for different cooling times.

We also use a master equation to fit the reversal probabilities for all cases, which assumes the average time dependent magnetisation $m(t)$ [56]:

$$m(t) = m_0 - (m_0 - m_\infty)[1 - exp(-t/\tau_N)] \tag{4.8}$$

where m_0 is the initial magnetisation, m_∞ is the magnetisation at infinite time, and τ_N is the characteristic relaxation time. This equation assumes the magnetisation is an exponential function of the characteristic time, from the initial magnetisation to that at infinite time. The infinite magnetisation takes the form:

$$m_\infty = tanh(\frac{\mu_0 \mu H}{k_B T}) \tag{4.9}$$

where μ_0 is the permeability of free space, and μ is the magnetic moment, H is the applied field, k_B is the Boltzmann constant, and T is the system temperature. The characteristic relaxation time is originated from the *Néel*-Arrhenius equation:

$$\tau_N = \tau_0 exp(\frac{\Delta E(T)}{k_B T}) \tag{4.10}$$

where $\tau_0 = 3 \times 10^{-11} s$ is the attempt time characteristic the material, and $\Delta E(T) = \Delta(KV + \mu_0 \mu H)$ is the height of the energy barrier. The anisotropy constant K is also temperature dependent, and is a power function of magnetisation, which is shown in Eq. 4.3 and Eq. 4.2.

In another work [57], this master equation works well with slower cooling processes, but not fits good with a faster cooling process which $\tau = 10$ ps. This is because the master equation does not include the linear reversal mode which allows a ultr-fast equilibration. The ultra-fast equilibrium magnetization is important for the reversal probability as mentioned in Ref. [57]. However, here in our system, we integrate the whole cooling process from the first 200 ps equilibration process and afterwards 1 ns cooling process. The numerical results (the lines in Fig. 4.12) agree with the simulation very well which demonstrates the HAMR process is similar with an ultra-fast field cooling process. Here because our system has a 200 ps equilibration process, which is long enough for a 800 K peak temperature, all the grains starts from the same quilibration state and thus the master works well for different cooling time.

4.3 Full HAMR process on a realistic granular recording media

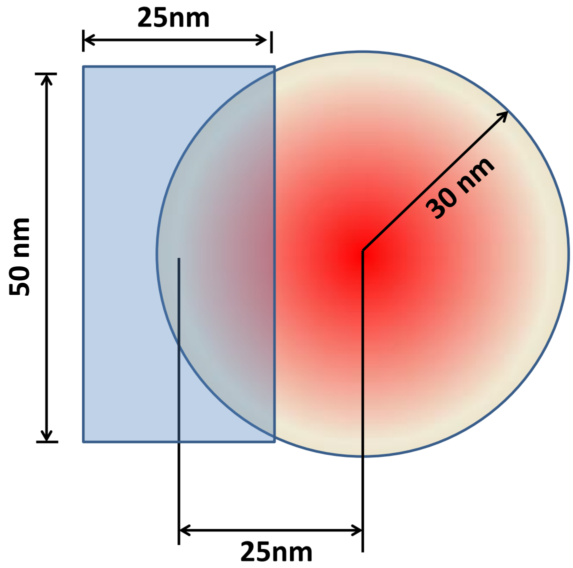

Figure. 4.13: Sketch of the magnetic field and laser areas in a hamr head: the blue square is the uniform magnetic field area, and the read round is the laser heating area.

A full HAMR process is simulated by using an atomistic model: a laser with peak temperature close to Tc at the centre is applied to the magnetic recording grains, which simultaneously, a magnetic writing head is also applied. The recording media is created using a Voronoi structure, shown in Fig. 4.14. A writing head is placed over the grains, with a laser and a uniform 25x50 nm magnetic field. The laser has a Gaussian distribution in temperature, and the distance between the laser centre and the field centre is 25 nm. The diameter of the laser is 30 nm. A sketch is shown in Fig. 4.13. The central temperature of the laser is higher than the Curie Temperature of the recording grains. When the writing head is moving over the grains, there will be some grains which are within the heating area, and if at the same time the applied field is reversed, the grains can be switched. Fig. 4.14(a) to Fig. 4.14(f) show a sequence of images as the write head is moved forward. The blue colour stands for spin up and the red colour is spin down. From these figures it can be clearly seen that the information (assuming spin-up is 1 and spin-down is 0) is recorded on the granular bits. The spin-up or spin-down states can be controlled by the wave form of the electric current in the coil which generates the magnetic field. In Fig. 4.14 the field is taken as a square wave. From Fig. 4.14(f), it can be investigated that the bit size is around 18x50 nm, so that the areal density can be obtained, which is around 0.7 TB/in^2. Although this areal density is less than that has been reported in industry recently, in this calculation mode, the bits size can be controlled by the laser area, the magnetic field width, and also the head velocity. So it can be inferred it is not difficult to get a higher areal density than the current results.

This full HAMR process is simulated to demonstrate that the atomistic model works for a realistic writing process of recording grains. No detailed study has been done yet, it only proves the capability of using this model for futher work of recording processes.

4.4 Conclusion

In this work, an atomistic model is used to simulate a single FePt grain to get the basic magnetic properties of this system, such as the hysteresis loop, the Curie temperature and the temperature dependent coercivity. Furthermore a multiple FePt grain system has also been investigated during a cooling process. Three crucial factors: the peak temperature, the cooling rate, and the applied field have impacts on the magnetisation and the reversal processes of the grains. The results point out that higher peak temperature, longer cooling time, and larger applied field will give a higher reversal probability, however, a peak temperature higher than Curie temperature will reduce the reversal probability and thus is

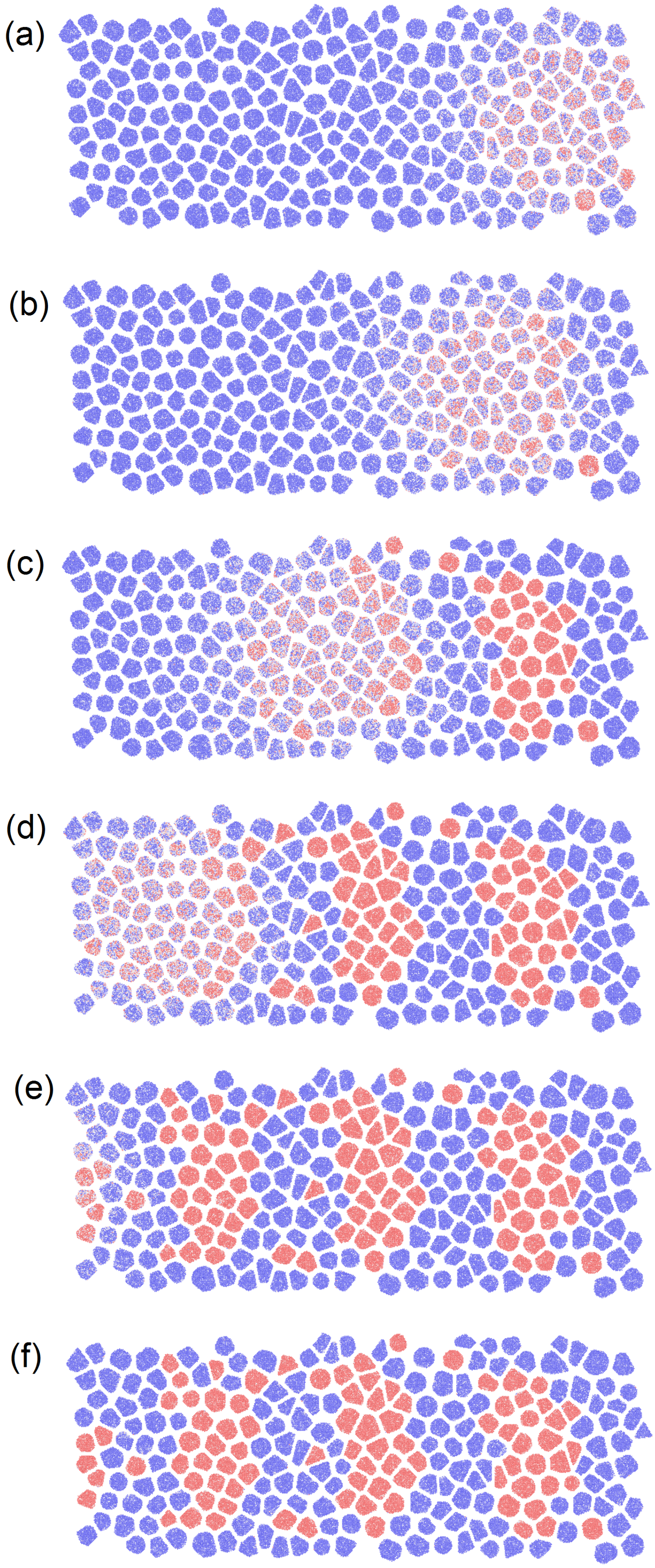

Figure. 4.14: Visualisation of a full HAMR processes to a realistic granular recording medium

unecessary. A semi-analytical approach was developed getting good agreement with the simulation results, and this proves the HAMR process is analogous to an ultra-fast cooling process which is controlled by the three factors. Both the simulation and numerical results give the explanation of the reversal process and how the three elements effect the reversal process.

5. Heat Assisted Magnetic Recording Processes of Exchange Coupled Composite Media

5.1 Introduction

Based on the results of previous chapters, it is known that perpendicular magnetic materials have attracted much attention because the high perpendicular anisotropy can maintain the energy barrier $\Delta E = KV/k_BT$ at a large value, such as 60, keeping the magnetisation stable for up to 10 years, in order to realize high density recording. However, the so-called ”trilemma” is always with the magnetic recording technique: the engineering compromise arising from different requirements of writeability, readability, and stability. High K can enhance the stability, but on the other hand, it will result in a large coercivity, requiring a very large writing field which is beyond the ability of existing writing heads. Therefore, an Exchange Coupled Composite (ECC) media is created to reduce the switching field of a hard magnetic layer [58], such as $L1_0$ ordered FePt or CoPt, by coupling a soft layer, such as Fe or Co. Exchange coupled composite materials have attracted much attention both experimentally [59, 60, 61, 62, 63, 64, 65] and theoretically [30, 37, 58, 66, 67], because they can not only reduce the coercivity of the recording grains, but also keep a higher thermal stability for long term data storage.

In an ECC bilayer, several parameters of the two magnetic layers have been studied since they are critical to the magnetic properties and effect the magnetic dynamics process: the magnetic anisotropy [68], the thickness of each layer [69, 70, 71]. However, the effect of interface exchange coupling has been less reported, mainly because in experiment it is difficult to measure this value. In this chapter, this interface exchange constant is investigated by using an atomistic spin model, finding it has large impacts on the coercivity of an ECC bilayer and also the reversal mode of the media at switching field. In this chapter, an $L1_0$ ordered FePt layer coupled with FCC Fe is used as the ECC media, where the anisotropy of FePt is high and that of Fe is low, and the Curie Temperature of FePt is lower than that of the Fe. It is possible that, since the coercivity of the hard layer is reduced at elevated temperature, there may be some advantage of using HAMR with ECC media. However, this requires the assumption that the ECC effect is still working at elevated temperature. In order to test this assumption, a full HAMR process is also performed on this ECC media, in order to investigate the reversal probability at some time scales.

5.2 Reversal Processes of an ECC FePt/Fe Bilayer

5.2.1 Interface Exchange Constant Dependent Switching Field of FePt/Fe bilayers

Firstly, an atomistic model is used to create an exchange coupled composite FePt/Fe bilayer, where FePt is $L1_0$ ordered, and Fe is FCC structure. The magnetic dynamics is calculated by using the LLG equation with a Heisenberg spin model. The anisotropy of FePt atoms is $K_H = 4.9 \times 10^{-23}$ J, and that of Fe is $K_S = 0$ J. The exchange constant of FePt is $J_H = 3.0 \times 10^{-21}$ J, and for Fe $J_S = 4.2 \times 10^{-21}$ J. The magnetic moment of the FePt atom is $1.458\mu_B$, and Fe is $2.2\mu_B$. The interface exchange constant J_{int} varies from 0 to the value of FePt J_H. The thickness of FePt is 5 nm and 1 nm Fe, and the grain is 5×5 nm in the x-y plane.

Zero Temperature

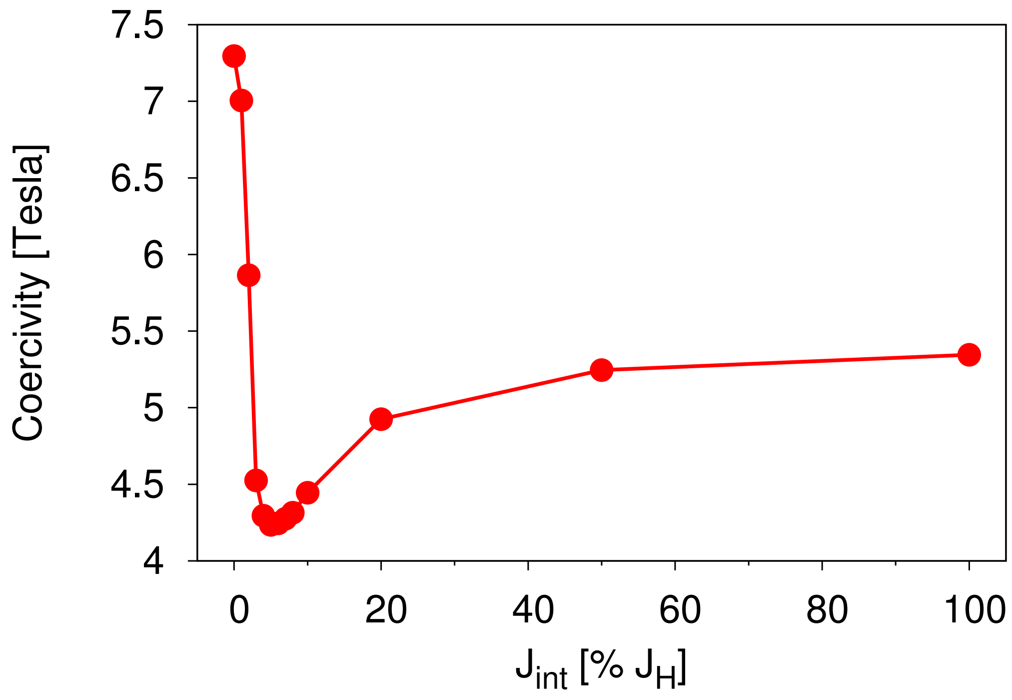

Figure. 5.1: Interface exchange constant dependent coercivity of a 5nm FePt layer coupled with 1 nm Fe layer at zero temperature.

Fig. 5.1 presents the coercivity of the FePt/Fe bilayer as a function of interface exchange constant J_{int} at zero temperature. The coercivity has a minimum value when $J_{int} = 5\% J_H$. This result is unexpected: it was expected that if a hard layer is coupled with a soft layer, the total coercivity of the bilayers will be reduced monotonically to a value intermediate between the two layers. However, in Fig. 5.1, when $J_{int} = 0$, $H_C = 7.25$ Tesla and $H_K = 7.254$ Tesla. Furthermore, when J_{int} is increasing, the coercivity drops dramatically to 4.3 Tesla at $J_{int} = 5\% J_H$, which is almost half of the maximum value. Afterwards, H_C is increasing slowly, back to 5.2 Tesla.

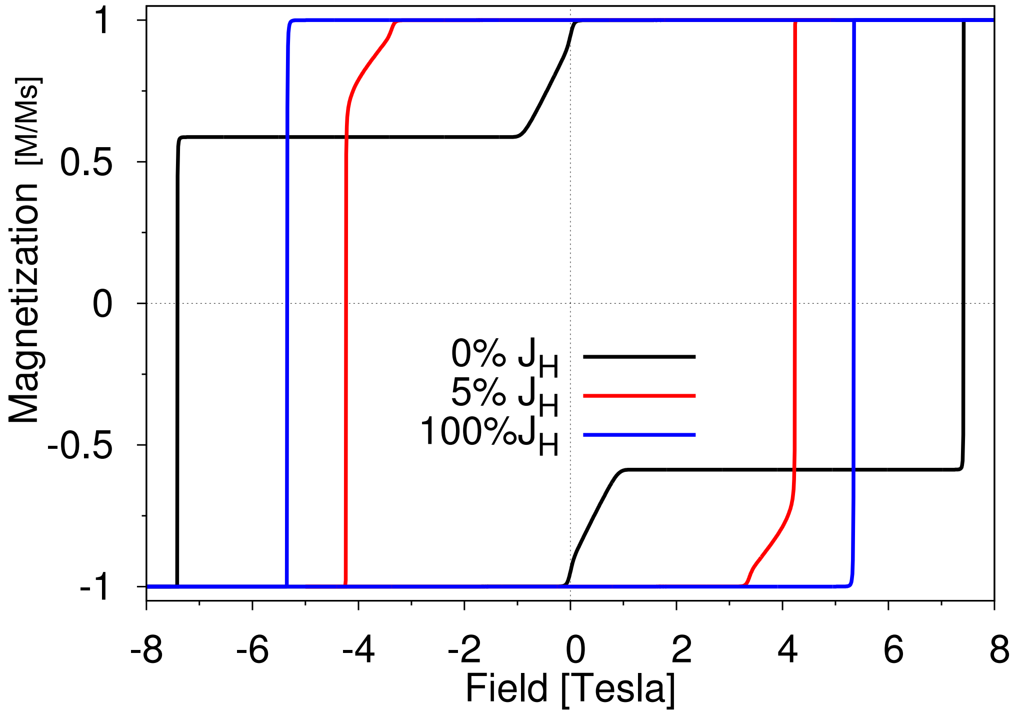

Figure. 5.2: Hysteresis loops of a 5nm FePt coupled with 1 nm Fe bilayers at zero temperature.J_{int}=0 (black line), 5% (red line), and 100% (blue line) of J_H

In order to explain this result, we plot several hysteresis loops with different J_{int}. Fig. 5.2 shows the hysteresis loops of FePt/Fe with different J_{int}=0 (black line), 5% (red line), and 100% (blue line) of J_H. It is easy to understand the black line, $J_{int} = 0$, FePt and Fe are not coupled together, and they are two independent layers. So their magnetisation is reversed at each switching field: the soft layer is switched at 0.1 Tesla and the hard layer reverses at 7.4 Tesla. This independent reversal also results in the two large steps in the loop, as well as the large coercivity. The large slope in the black line is because the anisotropy of the soft layer is set to be zero. The blue line is also easy to understand: when $J_{int} = 100\% J_H$, FePt layer and Fe layer are strongly coupled together, so they have to reverse at the same switching field, which is between the two values of hard and soft layers. In the meantime, no steps are found in the blue line. For the red line, $J_{int} = 5\%J_H$, it is different from the other two cases: there are not very large steps as the black line, and the loop is not as square as the other loops. It has two small steps around the switching fields, and the curve across the switching fields is more rounded.

Fig. 5.3 shows the angle of the average magnetisation with the easy axis. It is assumed there is no domains in each layer. This assumption is suitable for the 0% and 100% cases, but not for the 5% case. According to this result, it can be assumed, when $J_{int} = 5\%J_H$, there is domain structure in the hard and soft layers. And because of the nucleation and propagation of the domain structure, the coercivity of the bilayers achieves the minimum value.

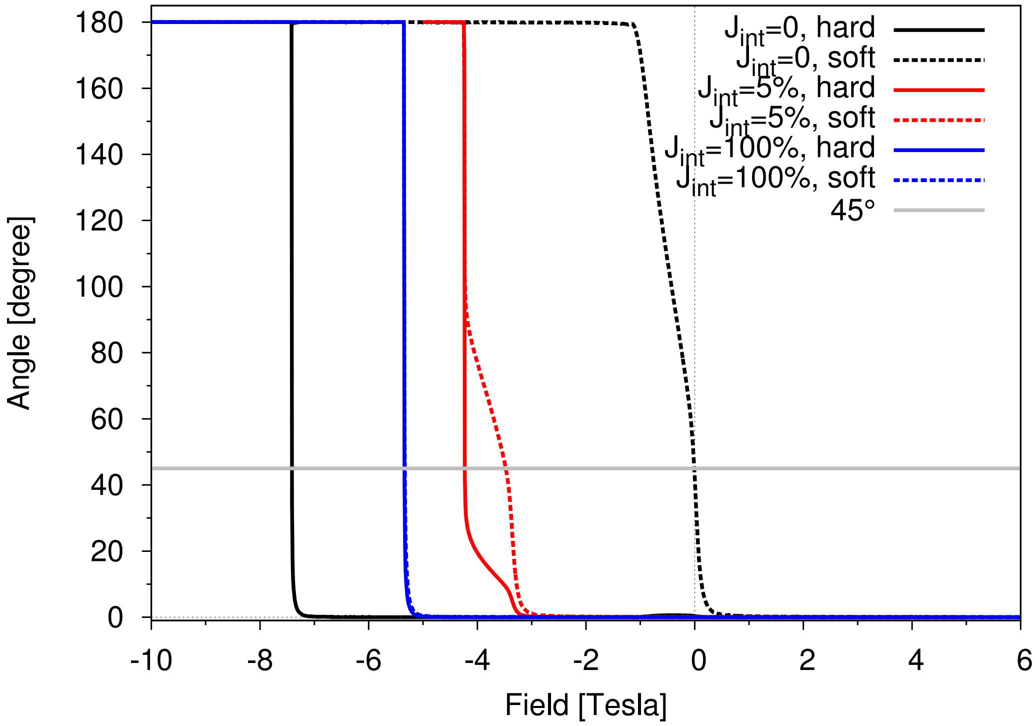

Figure. 5.3: Angle between the magnetic moment and easy axis of the hard layers (the solid lines) and the soft layers (the dashed lines). J_{int}=0 (black line), 5% (red line), and 100% (blue line) of J_H

According to the hysteresis loops for different J_{int}, it can be inferred that the reversal modes of the FePt/Fe bilayers are different for different J_{int}. Before seeing the visualization of the reversal processes, we plot the angle of the magnetic moments of hard and soft layers around the switching fields in Fig. 5.3. The magnetic moment of each layer is treated as an independent vector, whose angle with the easy axis (+z direction) is plotted as a function of applied field. The applied field is reduced from +7.5 Tesla to -7.5 Tesla along the z direction (from right to left along the x axis in the Figure), so these are the left branches in the hysteresis loops. For the black lines, $J_{int} = 0$, the angle of the hard layers suddenly changes from 0° to 180° at a large negative field, whereas the dashed line, which is the soft layer, reverses at a field close to zero, which means the reversal happens independently. For the blue lines, when $J_{int} = 100\% J_H$, the two blue lines are identical, and the angle changes from 0° to 180° at the same field. This is because the strong interface coupling makes the hard and soft layers reverse together. However for the red lines, $J_{int} = 5\% J_H$, the two angles of hard and soft layers start to reverse at the same field, around 3 Tesla. However, this reversal is slower than those of $J_{int} = 0$ and $J_{int} = 100\% J_H$ cases. They do not change from 0° to 180° directly. Besides, the changing rates of the two angles are different: the soft layer reverses faster first and slows down from 70°, while the hard layer slows down from 20°. This means the soft layer starts to switch first, indicating that it nucleates the reversal. And this different reversal processes makes the small difference in the black lines.

In order to prove the assumption, we have plotted the layer resolved magnetisation of the hard and soft layers, which represents the magnetic moment of each atomic layer in the bilayers as a single averaged moment. Fig. 5.4 to Fig. 5.6 show the magnetic moment of each atomic layer in the FePt/Fe bilayers around the switching field, which shows different reversal modes for different interface exchange constants. Layer number 0 to 28 is FePt and layer number larger than 28 is the Fe atomic layers.

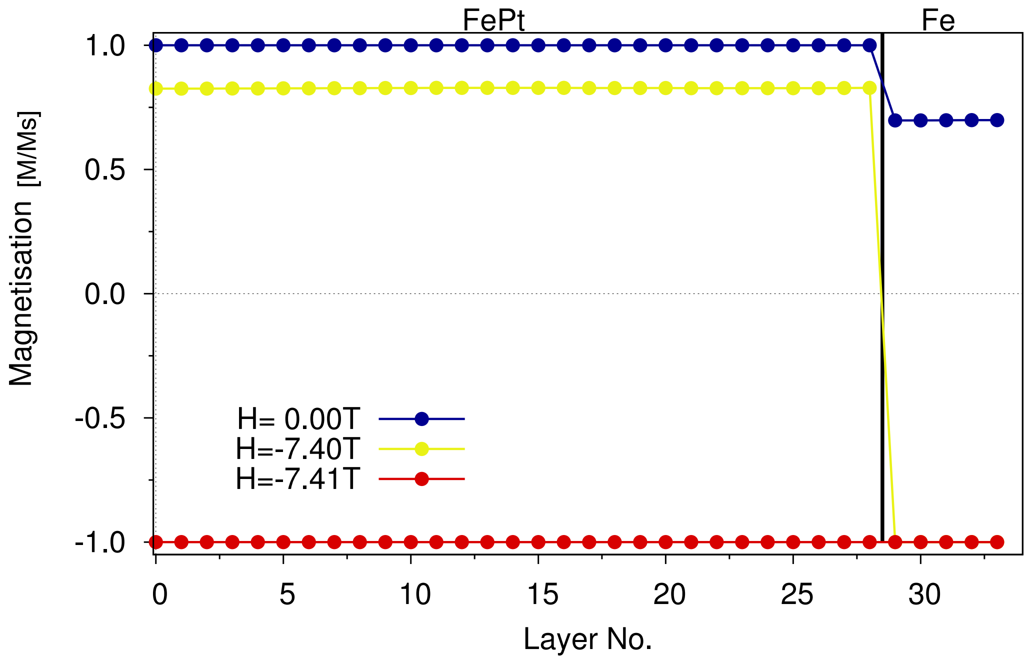

Figure. 5.4: Layer resolved magnetisation of the FePt/Fe bilayers:$J_{int} = 0$

Fig. 5.4 presents the layer resolved magnetisation for $J_{int} = 0$. The y axis is the z component of the normalized magnetisation of each layer. It can be seen before the switching field, $H_{applied} = 0.00$ Tesla, the magnetisation of FePt is 1 and that of Fe is 0.7. This is because when the field is far away from switching field, the FePt spins are maintained in the initial easy axis. However, the Fe exhibits soft magnetic properties due to the magnetostatic which is taken account into the calculation. When the negative field is increasing, the magnetisation of Fe is negative, which means the soft layer has reversed while the hard layer stays at saturation value. This status continues until the switching field of the hard layer, at which the hard layer reverses. This reversal process is very quick, and it is a coherent reversal process. This layer resolved magnetic moments reversal process can explain the large steps in Fig. 5.2 and the sudden changing of the angles in Fig. 5.3.

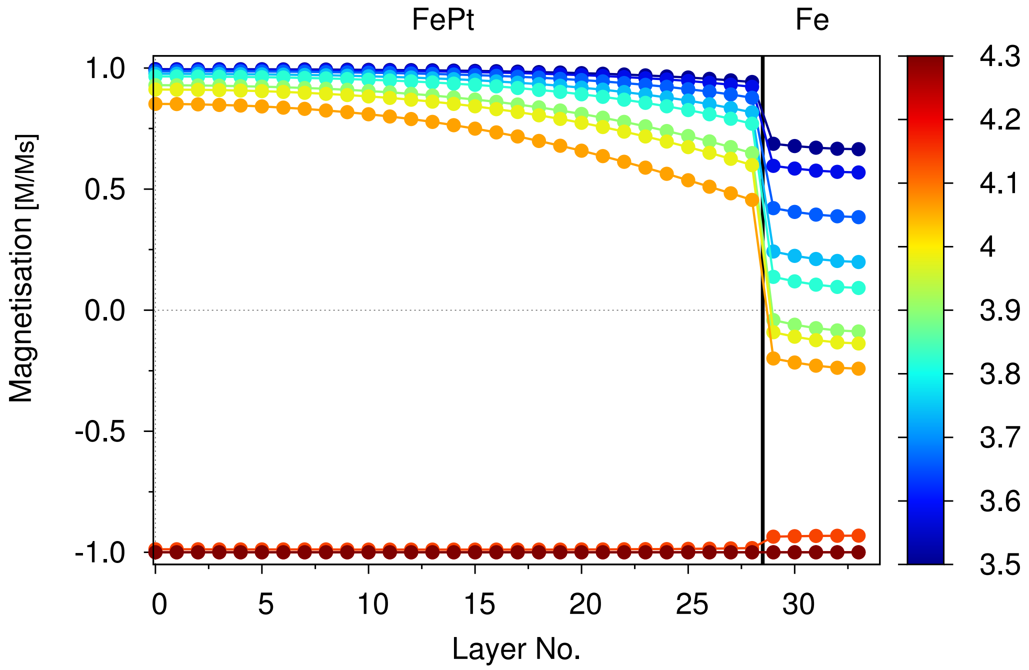

Figure. 5.5: Layer resolved magnetisation of the FePt/Fe bilayers:$J_{int} = 5\% J_H$

Fig. 5.5 presents the layer resolved magnetisation when $J_{int} = 5\% J_H$. The colour box on the right shows the value of negative applied fields. It can be seen that the soft layer starts to reverse earlier than the hard layer, and at around -3.9 Tesla, the soft layer has reversed. The reversal of the hard layer follows later, so there is a discontinuity between the soft and hard layers. Also, in the hard layer, the magnetisation of each atomic layer varies slightly. This small difference does not cause a domain structure because the thickness of the soft layer is too thin to support a domain structure. However this variation in the layer resolved magnetisation proves the reversal process of the bilayers is not coherent. The soft layer switches first, and the exchange coupling makes the atomic layers of FePt close to the interface rotate first and afterwards the rotation propagates to the rest of the FePt atomic layers. This incoherent rotation is more obvious in Fig. 5.6 when the interface exchange coupling is stronger. Additionally, the reversal mode for a weak interface coupling will result in a smaller coercivity, which can be proved in the later free energy calculation.

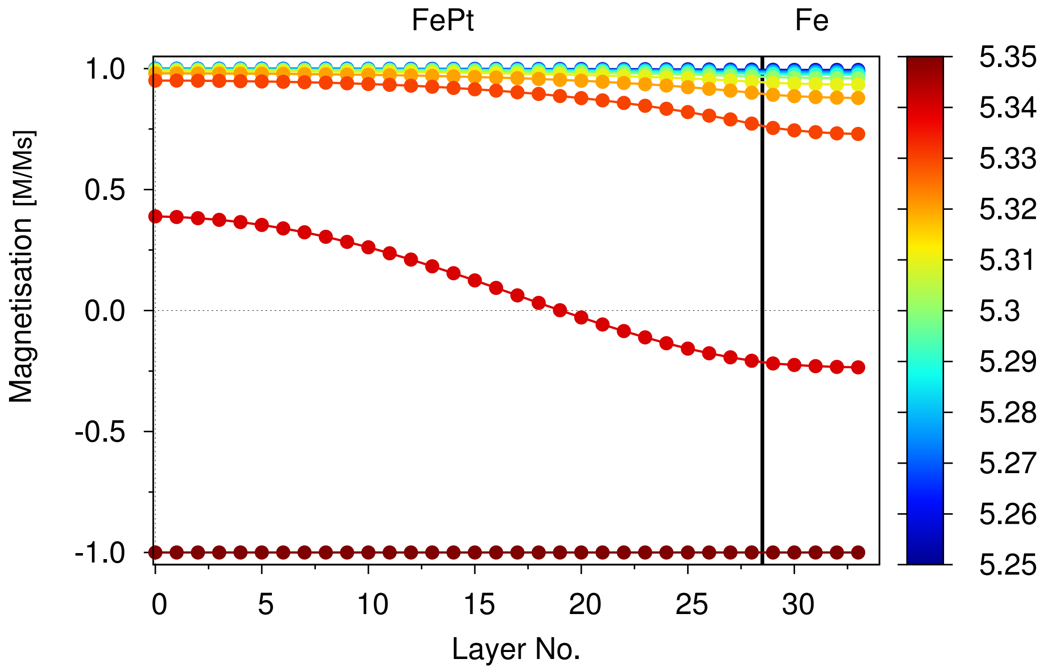

Figure. 5.6: Layer resolved magnetisation of the FePt/Fe bilayers:$J_{int} = 100\% J_H$

Fig. 5.6 presents the strongly coupled FePt/Fe reversal process. The colour box on the right also shows the value of negative applied fields. When $J_{int} = 100\% J_H$, the hard and soft layers are strongly coupled together. It can be seen that the magnetisation of Fe initially starts to decrease when the applied field is -5.3 Tesla. Then the reduction of magnetisation spreads into the FePt atomic layers. Especially when the applied field is -5.34 Tesla, the layer resolved magnetisation curve crosses the zero axis. It can be inferred that the nucleation of magnetisation rotation starts from the top atomic layers in Fe, because it has smaller anisotropy and has a weaker coupling from surface, since an open boundary condition is used in this model. This rotation later propagates to the FePt atomic layers and completes the reversal process. Compared to the weaker interface coupling, the discontinuity between Fe layers and FePt layers can not be found in this case. Additionally, the reversal process with a stronger interface coupling is much faster than the weaker interface coupling, from -5.3 Tesla to -5.35 Tesla, all the arrows turn to the opposite direction immediately. This result demonstrates the sharp blue curve in the hysteresis loops in Fig. 5.2.

In order to more deeply understand the reversal processes of the FePt/Fe bilayers, we have plotted the vectors of layer resolved magnetisation. Fig. 5.7 to Fig. 5.9 show the magnetic moment of each atomic layer in the FePt/Fe bilayers around the switching field, which shows different reversal modes for different interface exchange parameters. The red dashed lines specify the FePt/Fe interface. The numbers above each columns of arrows are the applied fields.

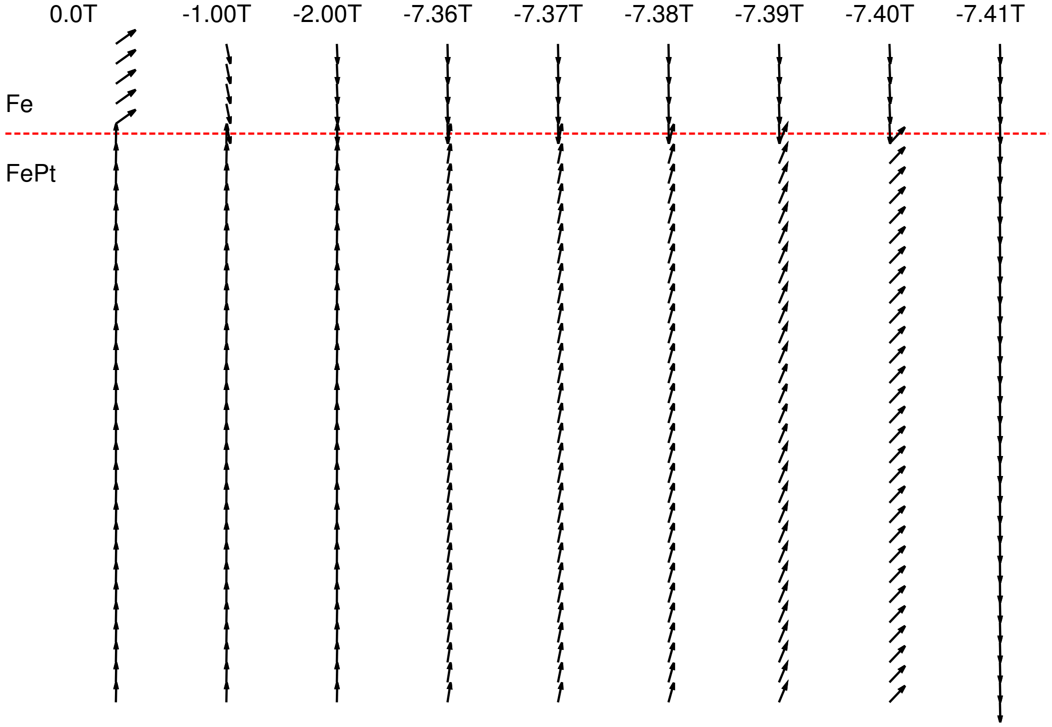

Figure. 5.7: Layer resolved magnetisation reversal of the 5nm FePt coupled with 1nm Fe: $J_{int} = 0\% J_H$

Fig. 5.7 presents the independent magnetic switching of each Fe and FePt layers when there is no interface exchange coupling. The arrows show the orientations of the magnetic moment of each atomic layer. It can be seen when the applied field is very small, the soft layer behaves more paramagnetically because the anisotropy of Fe is set to zero in the calculation. After the soft layer is reversed, the magnetic moments of Fe and FePt are opposite to each other, which explains the large step in the hysteresis loop. This opposite state continues until $H_{applied}$=7.36 Tesla, where the hard layer starts reversing. This reversal process is very quick and coherent. This is responsible for the sharp drop at the switching field in the hysteresis loop.

Fig. 5.8 and Fig. 5.9 show the reversal processes when J_{int} is not zero. For a weaker interface coupling in Fig. 5.8, the coherent rotation nucleation field, which is around -3.5 Tesla, is much smaller than the coercivity, which is around

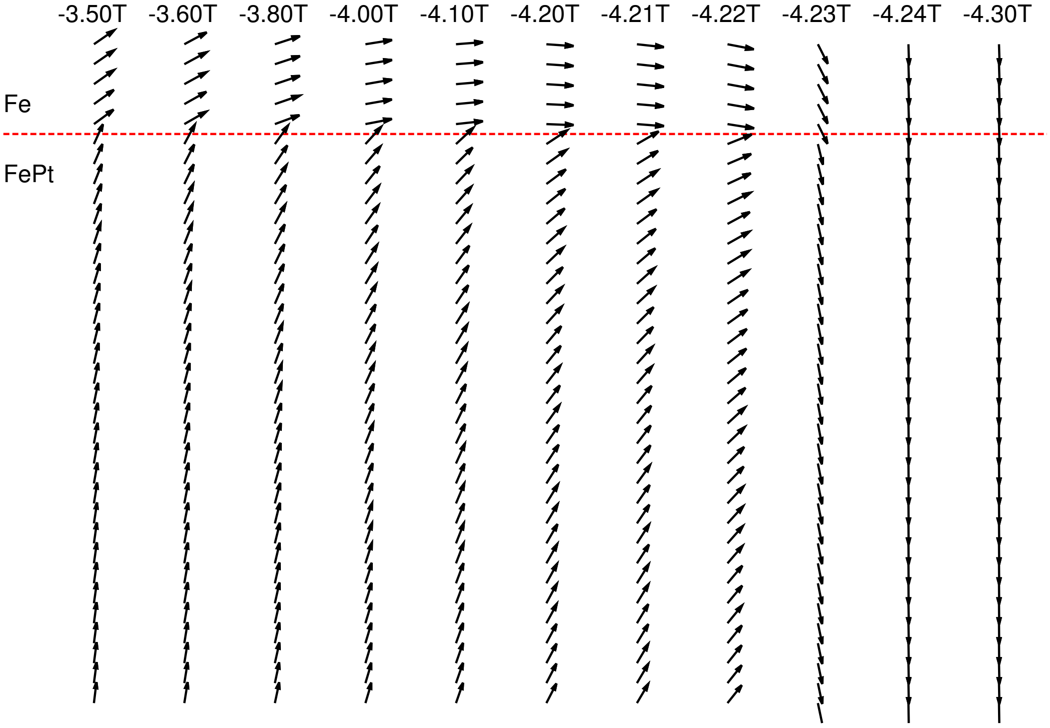

Figure. 5.8: Layer resolved magnetisation reversal of the 5nm FePt coupled with 1nm Fe: $J_{int} = 5\% J_H$

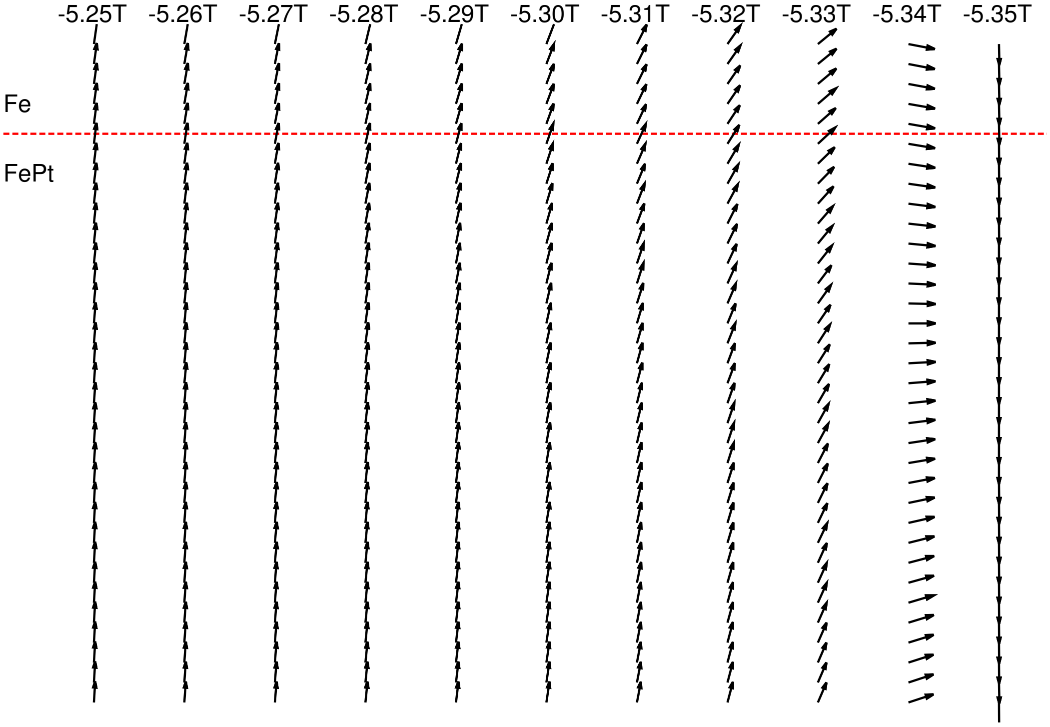

Figure. 5.9: Layer resolved magnetisation reversal of the 5nm FePt coupled with 1nm Fe: $J_{int} = 100\% J_H$

-4.2 Tesla. The Fe and FePt layers reverse have a discontinuity at the interface, which means the soft layer starts to reverse at a smaller field first, and then the interface exchange coupling pulls the hard layer to reverse. In Fig. 5.9, the coherent rotation nucleation field is higher, around -5.25 Tesla and closer to the switching field. The soft and the hard layers are strongly coupled without any discontinuity, and the coherent reversal is completed quickly at -5.35 Tesla.

From the previous calculation, it can be analysed that for different interface exchange coupling, the reversal modes are different. The nucleation field of a reversed domain in the soft layer is effected by the interface exchange coupling: in Fig. 5.2, the points where the magnetisation starts to reduce determines this nucleation field. It can be seen this nucleation field increases when the interface exchange parameter is increasing, which is due to the contribution from the hard layer. Furthermore, for small interface exchange coupling, the propagation of the reversed domain in soft layer is inhibited by the hard layer, as shown in Fig. 5.7, since it has very high magnetic anisotropy. When the interface exchange coupling is increasing, the propagation of the reversed domain is encouraged into the hard layer, shown in Fig. 5.8. This causes the a minimum value of the coercivity of the bilayers. When the interface exchange coupling is as strong as in Fig. 5.9, a coherent rotation reversal mode is established and thus the system coercivity is increased.

To sum up, the coercivity of FePt/Fe bilayers is strongly dependent on the interface exchange constant, which can be much reduced compared to the single hard layer. For smaller exchange coupling the coercivity is reduced to a minimum value at intermediate J_{int}. Incoherent rotation of each atomic layer is found in the hard layer, and its nucleation and propagation decreases the energy barrier to be crossed in a switching process and reduces the coercivity.

5.2.2 Free Energy Calculated by Constrained Monte Carlo Method

A free energy calculation using the Monte Carlo method is shown in Fig. 5.10. The free energy has the maximum value at soft/hard $\theta_{soft} = 0°, \theta_{hard} = 180°$, or $\theta_{soft} = 180°, \theta_{hard} = 0°$, when the soft and hard layers are opposite to each other. This state has the highest energy because of the exchange coupling. To discuss the free energy in a different aspect, Fig. 5.11 shows the gradient free energy as a function of m_Z. From Fig. 5.11 it can be seen that the coherent rotation path is slightly higher than the minimum free energy, therefore two nucleation fields are obtained according to the gradient of the coherent rotation path and the minimum free energy. These are the coherent rotation nucleation field and the fitted nucleation field. This result demonstrates the coherent rotation happens in the hard/soft bilayers if the interface exchange coupling is strong. Note that this is the zero applied field case. It suggests that, although the coercivity is reduced, the thermal stability is relatively unaffected for this case.

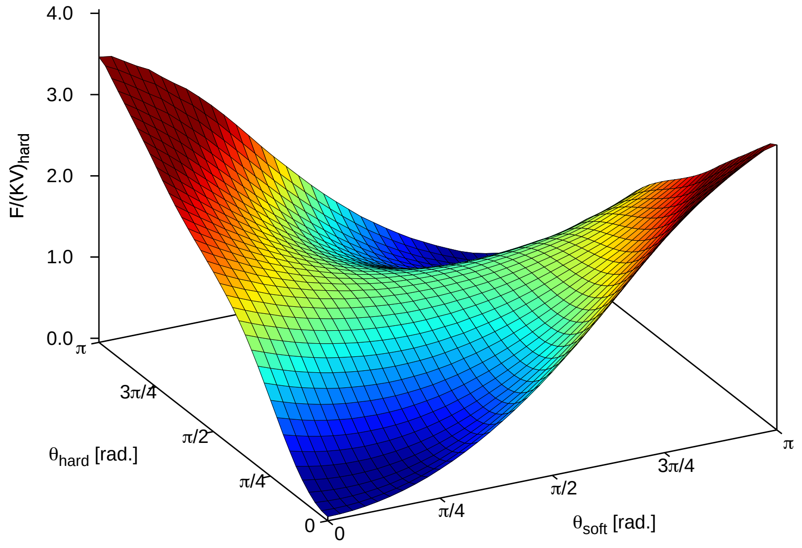

Figure. 5.10: The free energy of 5 nm FePt coupled with 1 nm Fe: the interface exchange coupling is $J_{int} = 100\%J_H$.

5.2.3 Effect of the Thickness of Soft Layer in ECC Bilayers

In order to study the effect of the thickness of soft layer and the interface exchange with different thickness, we calculate the coercivity of the 5 nm FePt/x nm Fe, x equals to 2, 3, 4, 5, 6, 7, 8, 9, 10 nm respectively, with varying interface exchange parameters J_{int}.

Fig. 5.12 shows the coercivity of 5 nm FePt coupled with 2 nm Fe, as a function of the interface exchange coupling J_{int}. Similar to the 1 nm Fe results, the coercivity is decreased a lot by coupling to the soft layer. It drops to almost half of the value of the single hard layer. The coercivity approaches the minimum value when $J_{int} = 20\%J_H$, around 2.95 Tesla. When the interface exchange is increasing, the coercivity of the bilayers also increases a little, to 3.05 Tesla. Compared to the results of 5nm FePt/1nm Fe, the absolute value of coercivities of 2 nm Fe case are smaller. Furthermore, the change of coercivity as a function of interface exchange coupling has similar trend to the 1 nm Fe case: the coercivity decreases quickly first to a minimum value and then increases slightly. However, the minimum value for the 2 nm Fe case has shifted to $J_{int} = 20\%J_H$, and the difference between minimum value and the value when $J_{int} = 100\%J_H$ is less than for the 1 nm case.

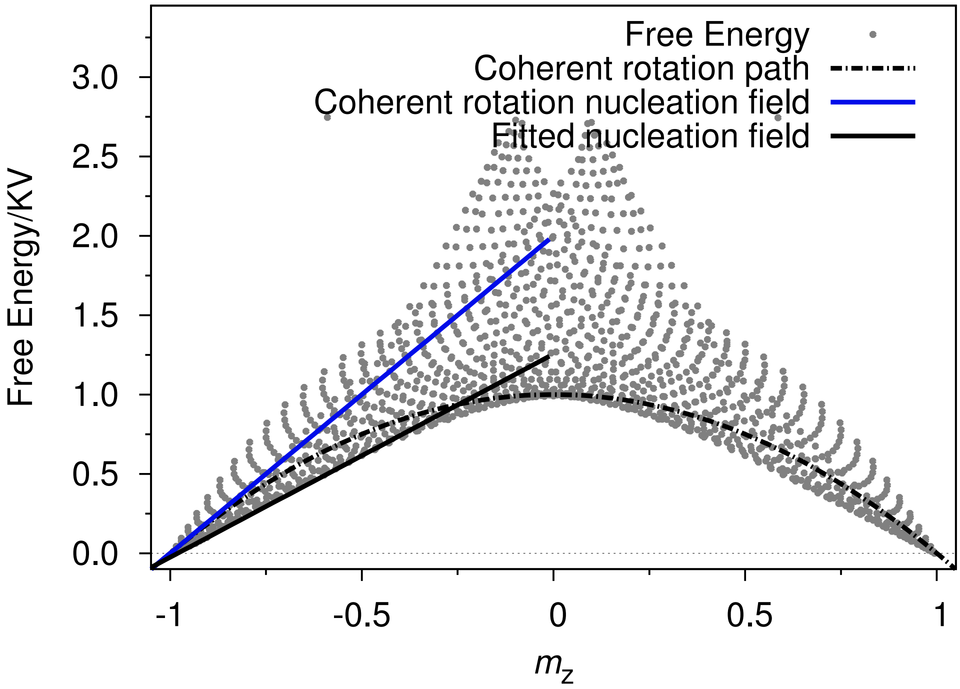

Figure. 5.11: The gradient free energy of 5 nm FePt coupled with 1 nm Fe: the interface exchange coupling is $J_{int} = 100\% J_H$.

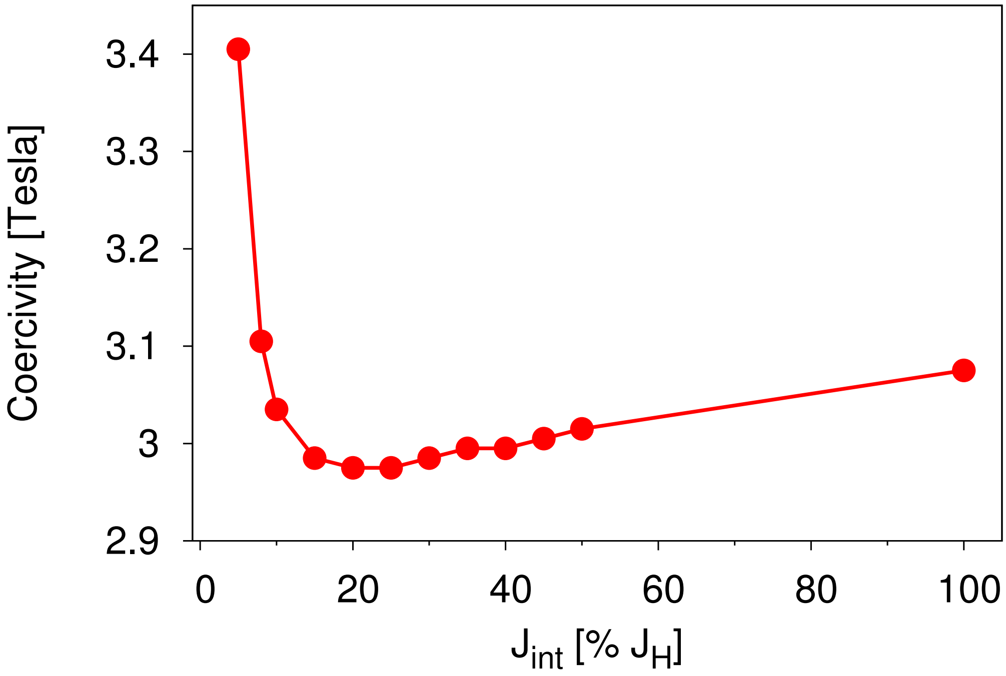

Figure. 5.12: The coercivity of 5 nm FePt/2 nm Fe bilayers as a function of the interface exchange coupling J_{int}.

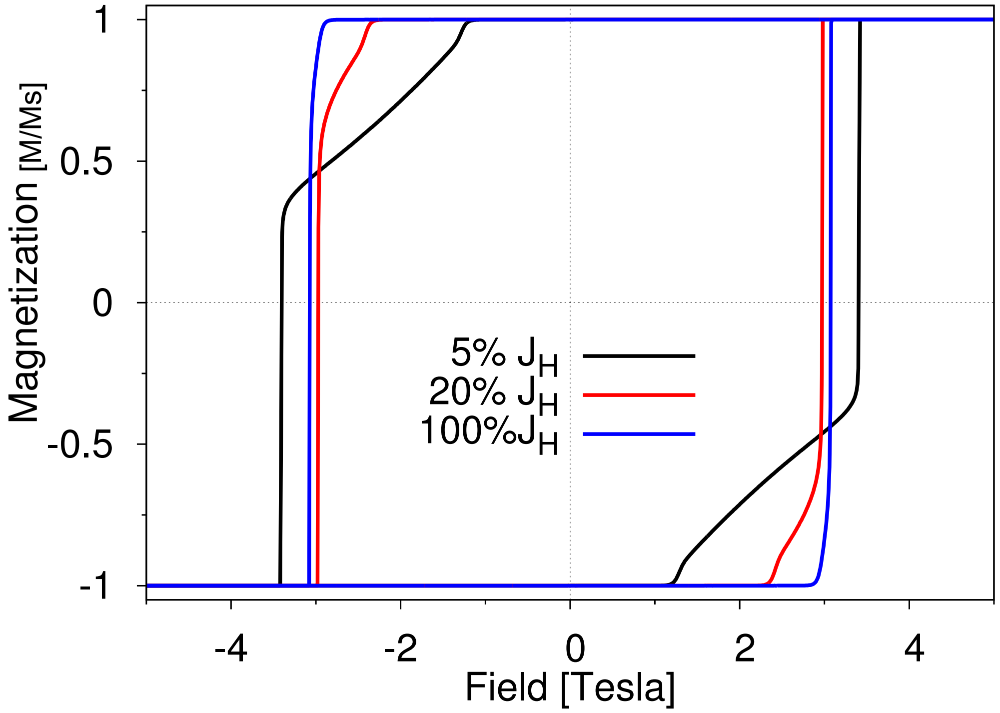

Figure. 5.13: The hysteresis loops of 5 nm FePt/2 nm Fe bilayers with different interface exchange coupling J_{int}.

Fig. 5.13 presents the hysteresis loops of 5 nm FePt coupled with 2 nm Fe, for different interface exchange coupling: J_{int}=5 (black line), 20% (red line), and 100% (blue line) of J_H. For smaller interface coupling, the hysteresis curve has two large steps which are the independent reversal processes of the soft and the hard layers. And this independent reversal comes along with a high coercivity close to that of the hard layer. For a middle value of interface exchange coupling, the two steps are smaller, and the coercivity is reduced to a smaller value. This can be explained by the reversal models discussed in the 1 nm Fe case. For a strong interface exchange coupling, the hysteresis loop is very sharp, which means the soft and hard layers are coupled together and the reversal is a coherent rotation. This also brings a reduction in the coercivity, but not as much as the middle value of interface coupling.

According to the previous hysteresis loops and the interface exchange coupling dependent coercivity curve, when the soft layer is thicker, the nucleation field of the reversed domain in soft layer is different from that of a thinner soft layer. When the soft layer is 1 nm, the nucleation field for $J_{int} = 5\% J_H$ is around 3.5 Tesla, however when the soft layer is increased to 2 nm, the nucleation field for the same interface exchange value is decreased to 1.5 Tesla. For the same value of interface exchange coupling, the contribution from the hard layer is less announced if the soft layer is thicker. Here the coercivity is dominated by the interfacial pinning field which will be discussed later. This results in the shift of the minimum coercivity in Fig. 5.12, and it can also be inferred that this minimum value of the coercivity will disappear when the thickness of the soft layer is increasing further.

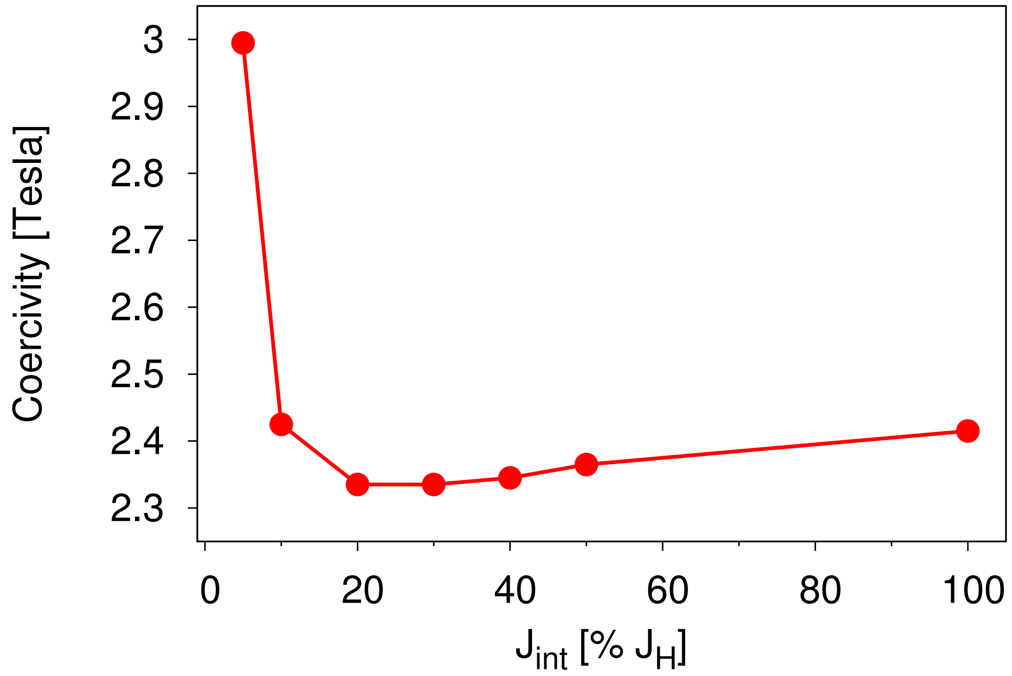

Figure. 5.14: The coercivity of 5 nm FePt/3 nm Fe bilayers as a function of the interface exchange coupling J_{int}.

Fig. 5.14 also studies the coercivity as a function of the interface exchange coupling, for a thicker soft layer, which is 3 nm Fe. Similarly, the coercivity values are smaller because of an enhanced effect of the soft layer. And the minimum value of coercivity is also around $J_{int} = 20\% J_H$. However, after the minimum value, the coercivity increases very slightly, and the difference between $J_{int} = 20\% J_H$ and $J_{int} = 100\% J_H$ is very small. This is because in a case of a thicker soft layer, the nucleation field of rotation is smaller and the propagation of the reversed domain is more exhibited. Therefore the difference of the coercivity for different interface exchange coupling is less announced in the thicker case.

The hysteresis loops are also given in Fig. 5.15, for different interface exchange coupling: $J_{int} = 5\% J_H$ (black line), $J_{int} = 20\% J_H$ (red line), and $J_{int} = 100\% J_H$ (blue line). Again, when interface coupling is as small as $J_{int} = 5\% J_H$, the hysteresis curve has two large steps which are the independent reversal processes of the soft and the hard layers. And this independent reversal results in a high coercivity. For a middle value, such as $J_{int} = 20\% J_H$, the two steps are smaller, and the coercivity is reduced to a smaller value. This can be explained by the

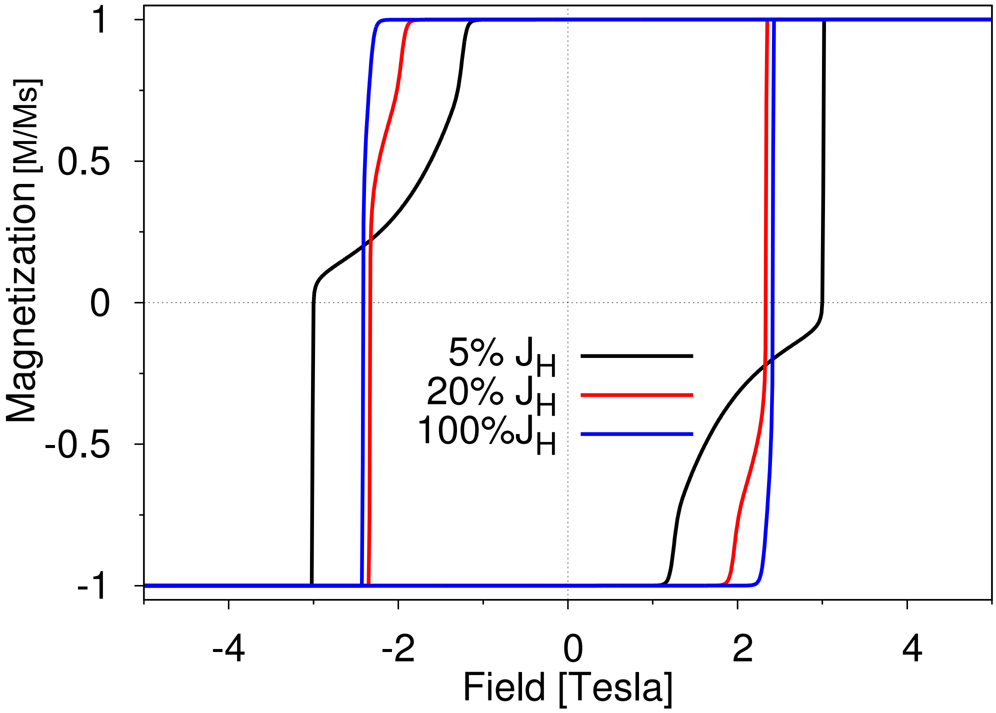

Figure. 5.15: The hysteresis loops of 5 nm FePt/3 nm Fe bilayers with different interface exchange coupling J_{int}.

reversal models mentioned earlier. For a strong interface exchange coupling $J_{int} = 100\% J_H$, the hysteresis loop is very sharp, which means the soft and hard layers are coupled together and the reversal is a coherent rotation. It also can be seen that the difference between $J_{int} = 20\% J_H$ and $J_{int} = 100\% J_H$ is smaller than for the thinner soft layers.

Furthermore, we have investigated a series of FePt/Fe bilayers. The FePt layer is kept at 5 nm, while the Fe layer is varying from 1 nm to 10 nm. For Fe layers thicker than 4 nm, we assume the minimum value of coercivity is when $J_{int} = 100\% J_H$, so the coercivity as a function of interface exchange coupling is not given for thicker soft layers.

Fig. 5.16 presents the coercivity of the FePt/Fe bilayers as a function of the thickness of Fe layer.The red circle points are the coercivity as a function of Fe thickness when the interface exchange coupling $J_{int} = 100\% J_H$. The black square points are the minimum coercivity of each thickness of Fe, which occurs, as shown earlier, at a specific value of the interface exchange coupling parameter. The coercivity decreases dramatically in the beginning: it drops from 7.2 Tesla for single FePt layer to 5.3 Tesla when the Fe layer is 1 nm thick. And it continuously decreases to 3 Tesla when the Fe thickness is 2 nm. Afterwards the coercivity decreases slowly with the increasing Fe thickness, approaching 1 Tesla when the Fe layer is 10 nm. In the meantime, the minimum value of the coercivity for each thickness of Fe is also calculated by varying the interface exchange coupling, finding that for thinner Fe, the difference between the minimum value of coercivity and the stronger coupling case is larger. For instance, the 1nm Fe layer case, when $J_{int} = 100\% J_H$, the coercivity is 5.3 Tesla, while the minimum value of coercivity is 4.2 Tesla when $J_{int} = 5\% J_H$. It can be seen when the thickness of Fe is increasing, this difference of coercivity between $J_{int} = 100\% J_H$ and the minimum value is decreasing, which means the effect of interface exchange is less important for the cases with thicker soft layer. When the Fe layer is thicker than 4 nm, the coercivity does not change too much when the interface exchange parameter changes. Therefore the value of $J_{int} = 100\% J_H$ is the minimum value.

According to a micromagnetic model [72], if the hard and soft layers are strongly coupled so that the domain wall is continuous across the interface from soft layer to hard layer, the coercivity should be:

$$H_C = H_K^H \cdot \frac{1 - \varepsilon_K \varepsilon_J}{(1 + \sqrt{\varepsilon_J \varepsilon_m})^2} \tag{5.1}$$

where $\varepsilon_K = K_S/K_H$, $\varepsilon_J = J_S/J_H$, and $\varepsilon_m = \mu_S/\mu_H$. Using the parameters for the hard and soft layers, we get $H_C = 1.23$ Tesla, which is comparable to the atomistic model if the thickness of the soft layer is large. This coercivity is called Kronmuller-Goll value which is the dashed blue line shown in Fig. 5.16.

Fig. 5.17 shows the hysteresis loops of FePt/Fe bilayers for different Fe thickness, the interface exchange coupling $J_{int} = 100\% J_H$. The colour box on the right shows the thickness of Fe layer in nm. The FePt is still kept at 5 nm. First of all, the switching field decreases when the soft layer gets thicker. Secondly, the hysteresis loop is less square for thicker soft layer case. This shows the different nucleation fields for each atomic layer when the soft layer is thicker and the interface exchange coupling is not strong enough to couple both of the soft and the hard layers.

To sum up the thickness effect, the effect of thickness of the soft layer in an ECC media is to reduce the coercivity of the hard/soft bilayers. The interface exchange coupling has a large effect on the coercivity. However, the thicker the soft layer, the less the interface exchange coupling effects the coercivity.

5.2.4 Room Temperature

The same calculation of the bilayers has been performed at room temperature (300 Kelvin), where the thermal effect is taken account into the atomistic scale calculation by using the Langevin Dynamics. Fig. 5.18 shows the coercivity of

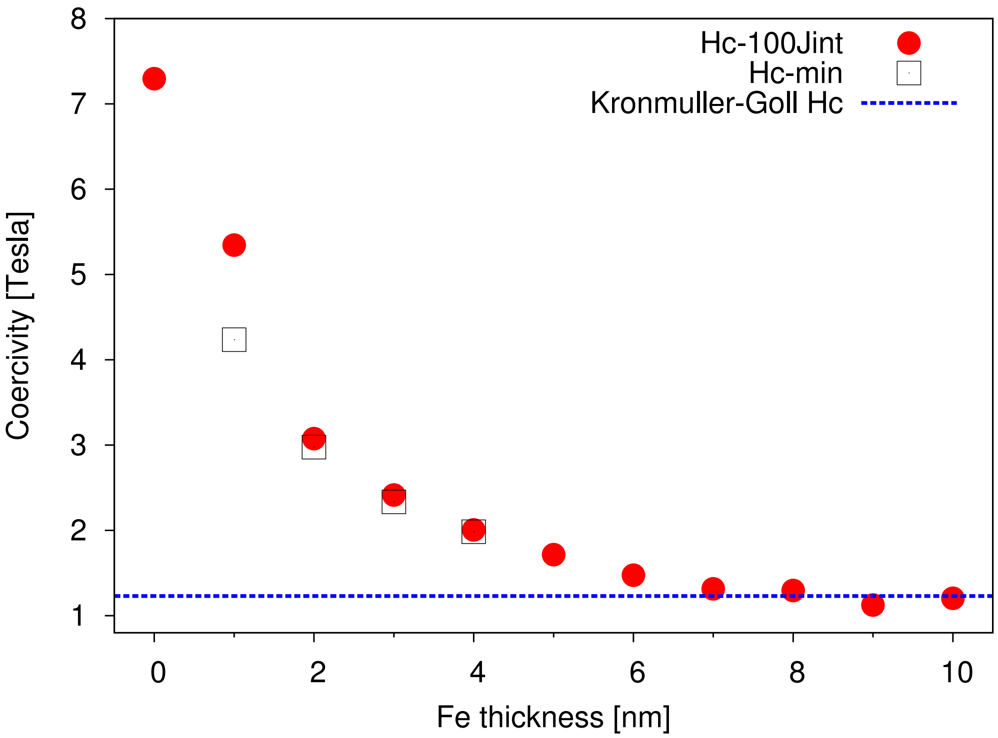

Figure. 5.16: The coercivity of FePt/Fe bilayers as a function of the thickness of Fe layer.

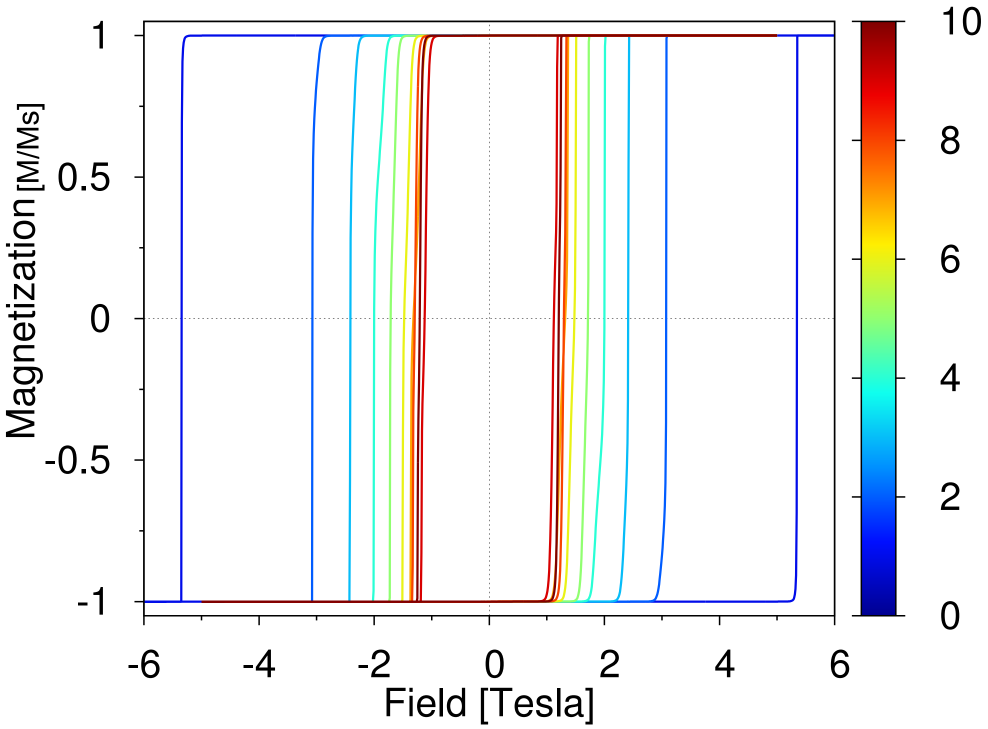

Figure. 5.17: The hysteresis loops of FePt/Fe bilayers for different thickness of Fe layer.

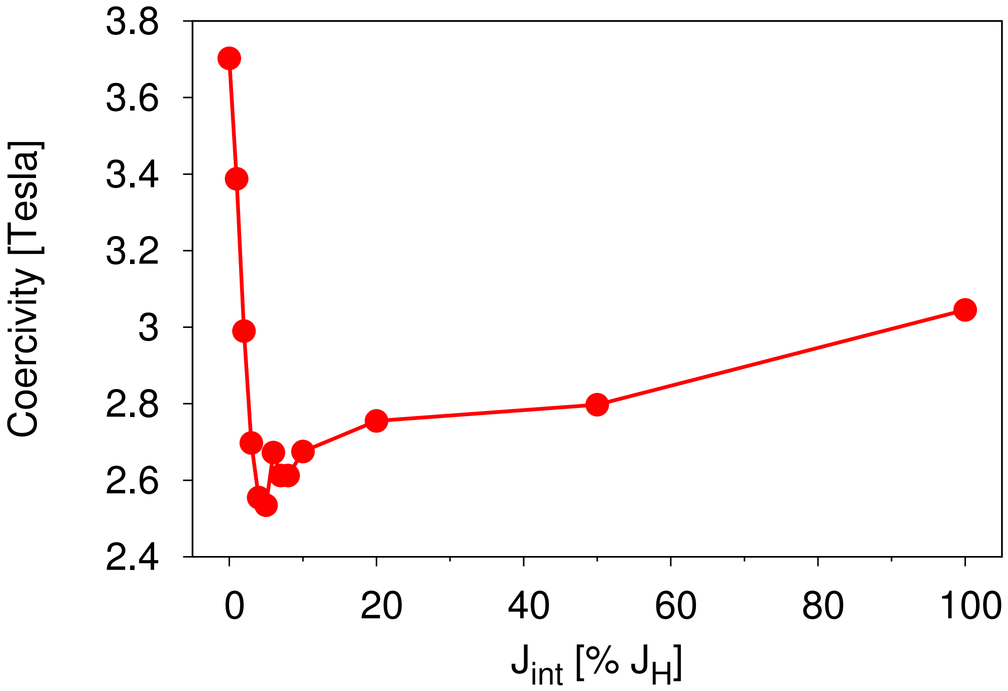

Figure. 5.18: Interface exchange constant dependent coercivity of a 5nm FePt coupled with 1 nm Fe bilayers at room temperature.

5 nm FePt coupled with 1 nm Fe as a function of interface exchange J_{int} at room temperature. The results are similar to those at zero temperature, except for lower coercivity at room temperature because of the thermal fluctuation. The coercivity decreases dramatically for weak interface exchange coupling, when $J_{int} = 5\% J_H$, the coercivity has the minimum value of 2.5 Tesla. And then the coercivity is increasing back a little, to 3 Tesla when $J_{int} = 100\% J_H$.

From Fig. 5.18, the coercivity reduction is smaller at 300K than 0K, which could be due to several reasons: 1. the reduction of the effective interface exchange due to spin fluctuations at the interface, or 2. the reduction in M_s of soft layer. These reasons are all related to the thermal effect, and therefore further work is required to solve these problems.

The hysteresis loops are shown in Fig. 5.19. The loops show a reduction of saturation magnetisation, which is around 0.8 because of the demagnetisation caused by the thermal fluctuation at room temperature. The behaviour of each loop is similar to that at zero temperature: for the black line when the interface coupling is zero, two large steps can be found because of the independent reversal of the soft and the hard layer. The coercivity is the same as a single hard layer. For the red line, when the interface exchange coupling is 5%, the steps are not apparent because of the thermal fluctuation, while the coercivity approaches the minimum value. When the interface exchange is very strong shown in the blue

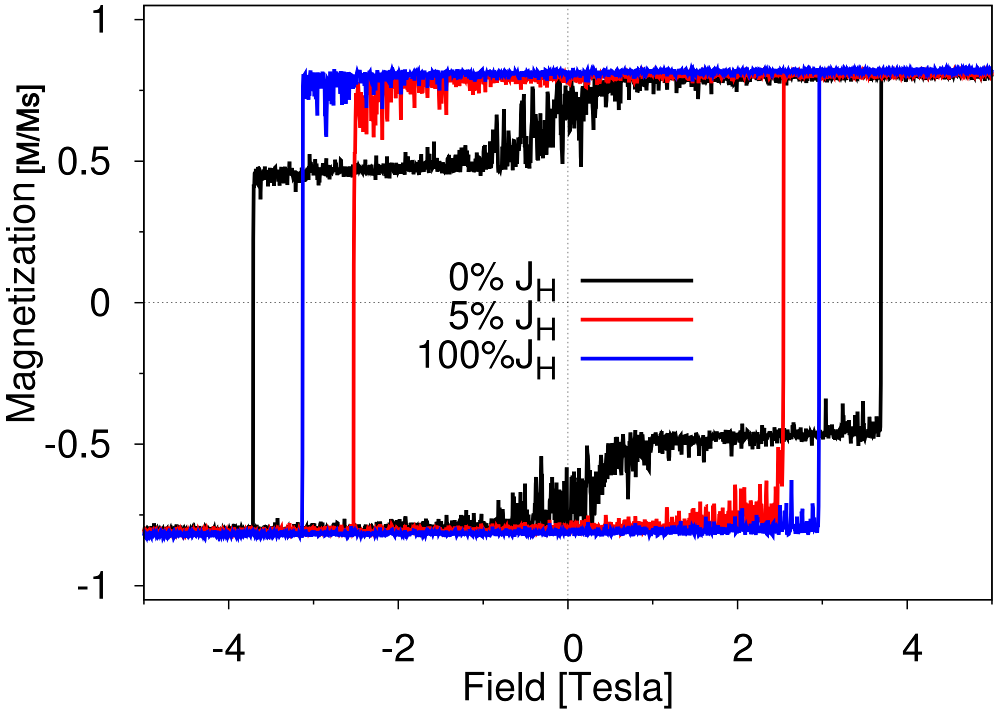

Figure. 5.19: Hysteresis loops of a 5nm FePt coupled with 1 nm Fe bilayers at room temperature.J_{int}=0 (black line), 5% (red line), and 100% (blue line) of J_H

line, no step can be seen in the curve, and the loop is quite square except for some thermal fluctuation. The coercivity is larger than weaker interface coupling case, but smaller than the no coupling case, consistent with the zero temperature calculation.

The effect of the thickness of the soft layer has also been studied at room temperature, as shown in Fig. 5.20. The coercivity is smaller than that at zero temperature because of the thermal effect. It starts from 3.1 Tesla for 1 nm Fe layer, and then decreases asymptotically to 1 Tesla when the Fe thickness is increased to 10 nm. Compared to the result at zero temperature in Fig. 5.16, the thickness of the soft layer in a hard/soft bilayers has a similar effect both at room temperature and zero temperature, which is to reduce the coercivity.

Fig. 5.21 shows the hysteresis loops of FePt/Fe bilayers for different Fe thickness at room temperature, the interface exchange coupling $J_{int} = 100\% J_H$. The color box on the right shows the thickness of Fe layer in nanometre. The FePt thickness is constant at 5 nm. Again, similar results can be found as in Fig. 5.17: the switching field decreases when the soft layer gets thicker; the hysteresis loop is less square for thicker soft layer case (more fluctuation can be found around the switching fields). Besides, the saturation magnetisation is smaller because of the thermal effect.

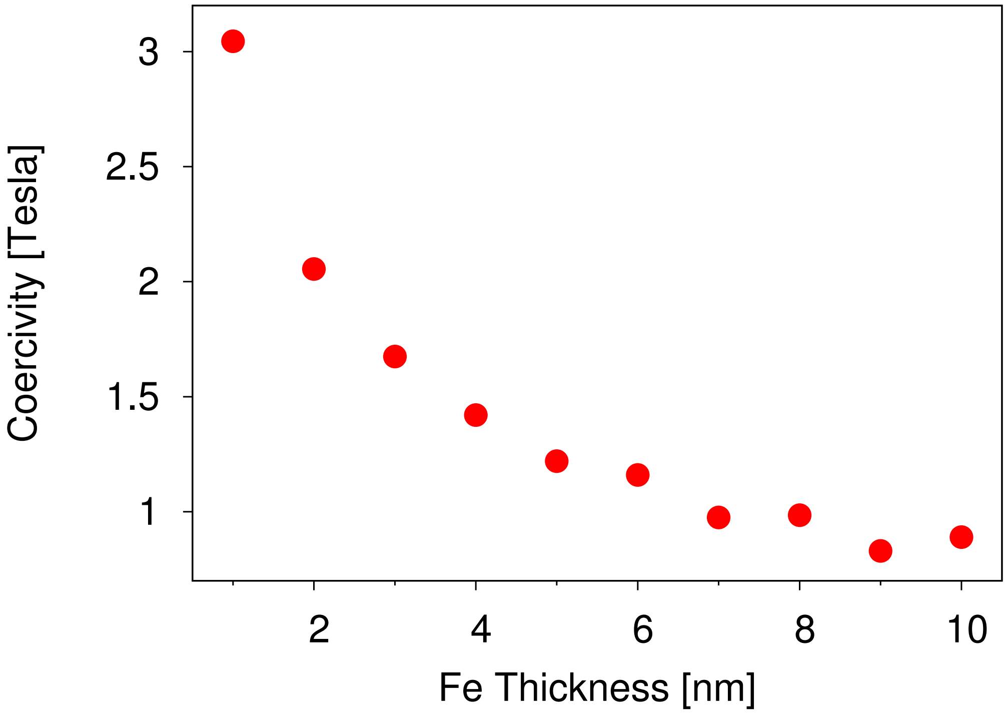

Figure. 5.20: The coercivity of FePt/Fe bilayers as a function of the thickness of Fe layer at room temperature.

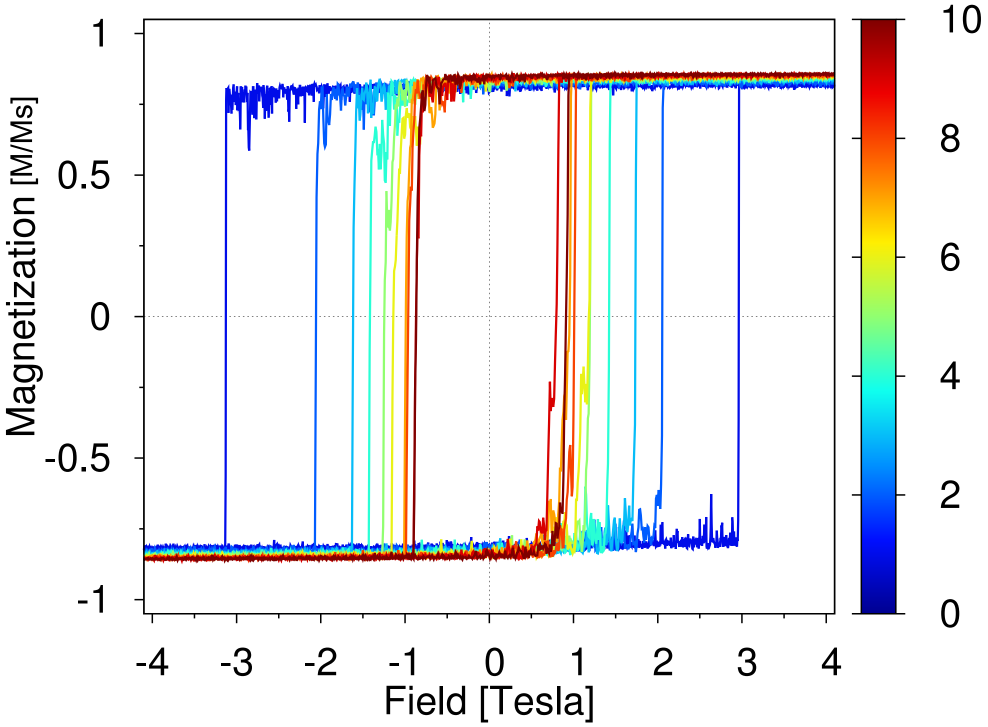

Figure. 5.21: The coercivity of FePt/Fe bilayers as a function of the thickness of Fe layer at room temperature, $J_{int} = 100\% J_H$.

To sum up, according to the results at room temperature, the interface exchange coupling still has a large effect on the coercivity of hard/soft bilayers. It reduces the coercivity from 3.7 Tesla to 2.5 Tesla, which can be seen from Fig. 5.18. Additionally, the interface exchange will reduce the coercivity most when it has a smaller value, for instance less than 10% of the bulk exchange in this system, rather than a very strong coupling. This is because for an appropriate J_{int} value, the reversal mode of the bilayers is different from the strongly coupled case. Furthermore, the thickness of the Fe layer also has the same effect on the coercivity at room temperature, which is to reduce the coercivity at a rate which is at most weakly dependent on the temperature.

5.3 Temperature Dependent Reversal Probability in a HAMR process of ECC media

5.3.1 Cooling Rate Dependent Reversal Probability

After studying the reversal processes of ECC bilayers, the main aim of this chapter is to apply the ECC media in a heat assisted magnetic recording process, and to see if the ECC media has advantages. So we have performed a whole field cooling process on ECC grains, which is 5 nm FePt coupled with 2 nm Fe, and the interface exchange coupling $J_{int} = 100\% J_H$. The grain size is 5 nm, and the total number of the grains is 100, there is no inter-grain exchange coupling in the system. The results are compared to those of a single 5 nm FePt layer [57]. The field cooling process is to apply an external magnetic field, which is 0.8 Tesla, opposite to the initial direction of the grains. In the meantime, a laser pulse is applied to the ECC grains, which has the temperature variation shown in Fig. 5.22. The temperature is assumed a Gaussian profile according to the following equation:

$$T(t) = T_R + (T_{max} - T_R) \cdot exp(-t^2/\tau^2) \tag{5.2}$$

where T_R is the room temperature 300 Kelvin. T_{max} is the peak temperature, which is varied from 300 Kelvin to 900 Kelvin, and τ is the cooling time (the pulse width), which is varied from 10ps to 100 ps. We have calculated the reversal probability by dividing the number of reversed grains over the total number of grains.

Fig. 5.23 shows the reversal probability as a function of peak temperature for different cooling time. The dashed lines are the results of the same cooling

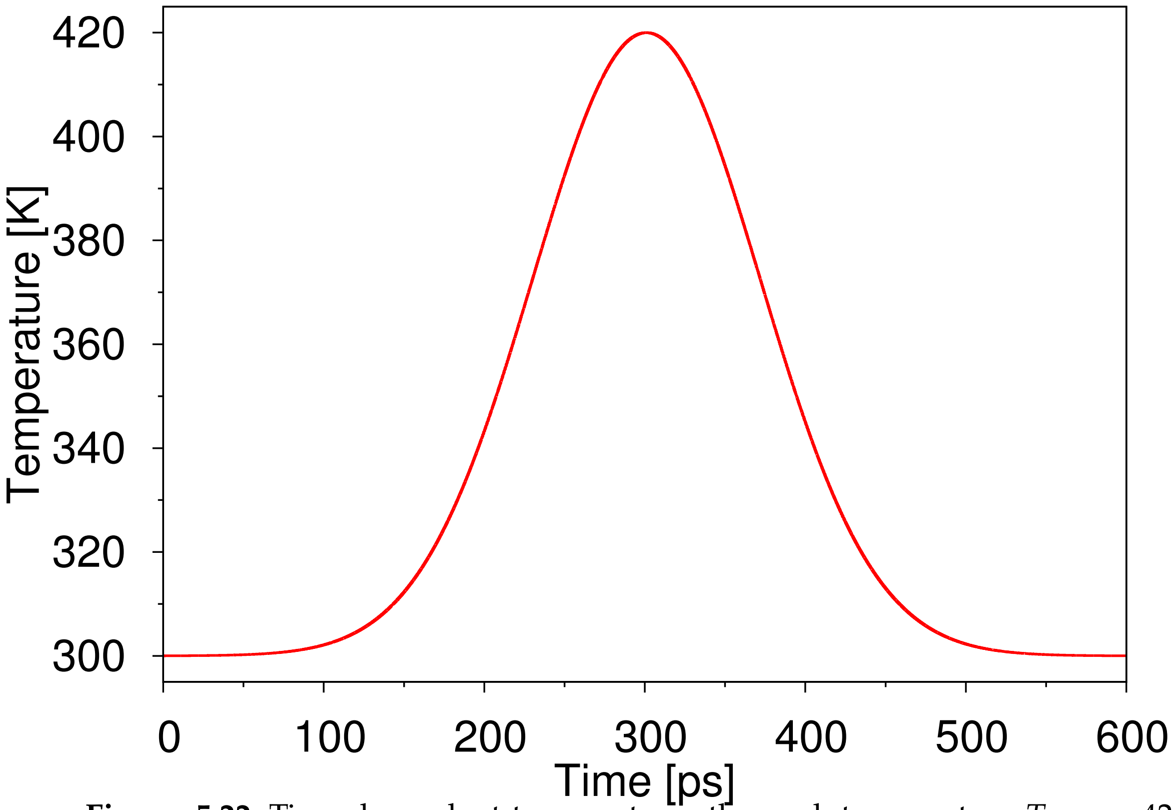

Figure. 5.22: Time dependent temperature: the peak temperature $T_{max} = 420K$, the cooling time $\tau = 100ps$.

processes of single FePt grains (the same grain size and magnetic properties). The points are the results of the ECC grains. Generally seen from the single FePt grains, the longer the cooling time, the higher the reversal probability. For the longer cooling time, heating over the Curie Temperature is not necessary. However, even for a very high peak temperature, the reversal probability cannot reach 100 percent. While for the shorter cooling time, the reversal probability is lower for any peak temperature. Compare the ECC grains, for a shorter cooling time, the reversal probability is much lower than that of the single FePt grains. While for a longer cooling time, the ECC grains have slight advantages.

There are two types of reversal mechanism which should be mentioned: precessional reversal and linear reversal [52, 53]. Precessional reversal is the most common mode of reversal which can be described by the LLG equation, however, this kind of reversal is slow. The linear reversal is much quicker, but requires a high temperature close to T_C. In the ECC bilayers, the FePt has a lower $T_C = 690$ K and the Fe has a high T_C around 1300 K. So for the ultrafast heating process, the reversal modes of two layers are different. FePt has linear reversal when the temperature is close or high than 690 K, but the peak temperature is much lower than the T_C of Fe, so Fe has precessional reversal. This means that the reversal of FePt is quick but Fe is slow, and so for a short cooling time, Fe is difficult to reverse and brings disadvantages to the reversal probability eventually.

For the FePt/Fe coupled grains, for a shorter time, because the cooling time is much shorter than the time required to complete a precessional reversal, so Fe is more difficult to reverse. The exchange coupling between Fe and FePt leads the FePt to recover in the direction of the Fe magnetisation, hence non-reversal of the Fe leads to non-reversal of the FePt. This results in the worse performance of FePt/Fe grains at a shorter cooling time. For a longer cooling time, Fe can finish the precessional reversal process. The FePt magnetisation reduces rapidly to zero and the combination of the applied field and exchange field from the Fe results in reversal of the FePt layer.

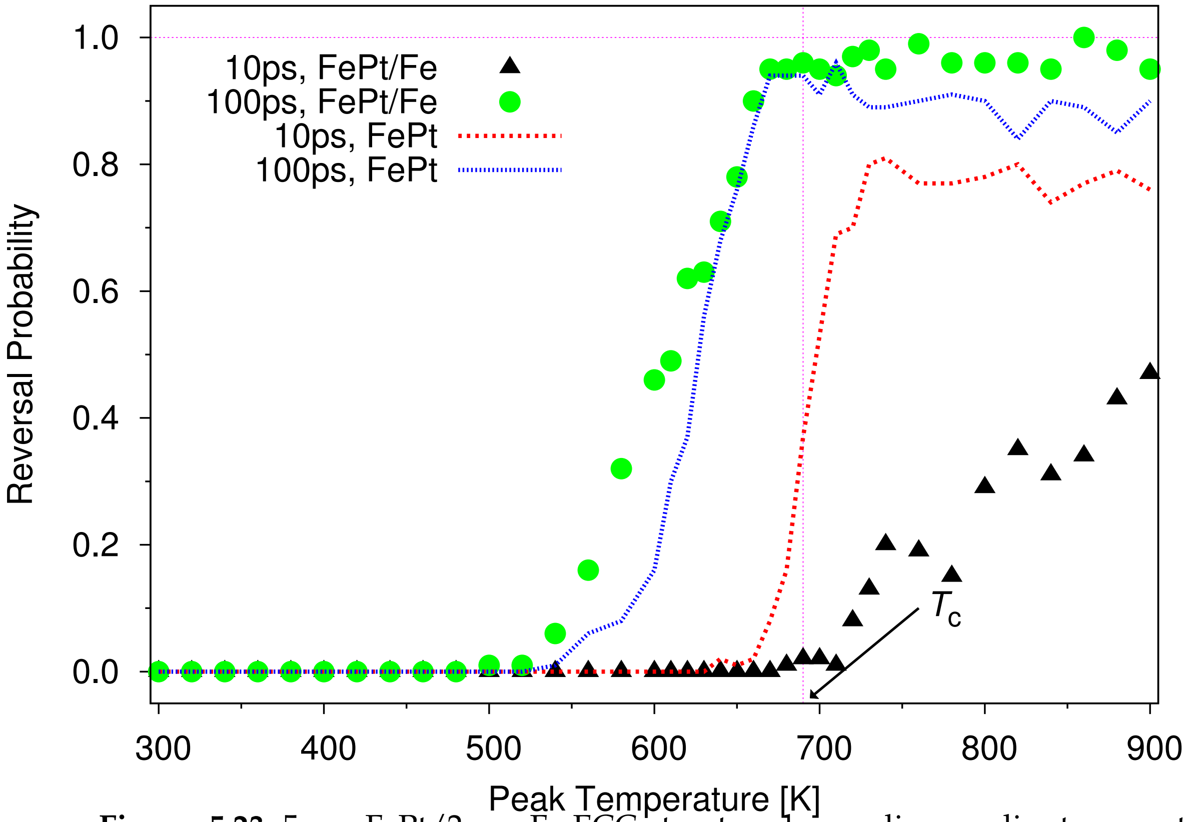

Figure. 5.23: 5 nm FePt/2 nm Fe ECC structured recording media: temperature dependent reversal probability at different cooling time.

5.3.2 *Effect of Interface Exchange Coupling and the thickness of soft layer on the Reversal Probability*

According to previous results, the thickness and the interface coupling are very important in determining the reversal processes of an ECC media. We have also calculated a field cooling process of a FePt layer coupled with a thicker Fe layer. The cooling process is still performed on 100 exchange decoupled grains, which are 5 nm FePt layer coupled with 5 nm Fe, and the interface exchange coupling $J_{int} = 30\% J_H$. The grain size is still 5 nm. Fig. 5.24 shows the reversal probability of this system, still compared to the single FePt grains. It can be seen, for a shorter cooling time, the reversal probability is much lower than for the 2nm Fe layer, presumably because of the slower reversal of the larger Fe grains. In contrast, fro the longer cooling time, the reversal probability is generally enhanced relative to the 2nm Fe layer case. This is possibly due to the fact htat, for the longer cooling time, the FePt/Fe has sufficient time to achieve the thermal equilibrium. In this case, the reversal probability will be determined by the ratio of $\mu H/kT$ for the Fe grains, which determines the actual value of the Fe magnetisation [9]. A larger Fe magnetisation would be expected to cause more reversal of the FePt due to an enhanced exchange field from the Fe layer.

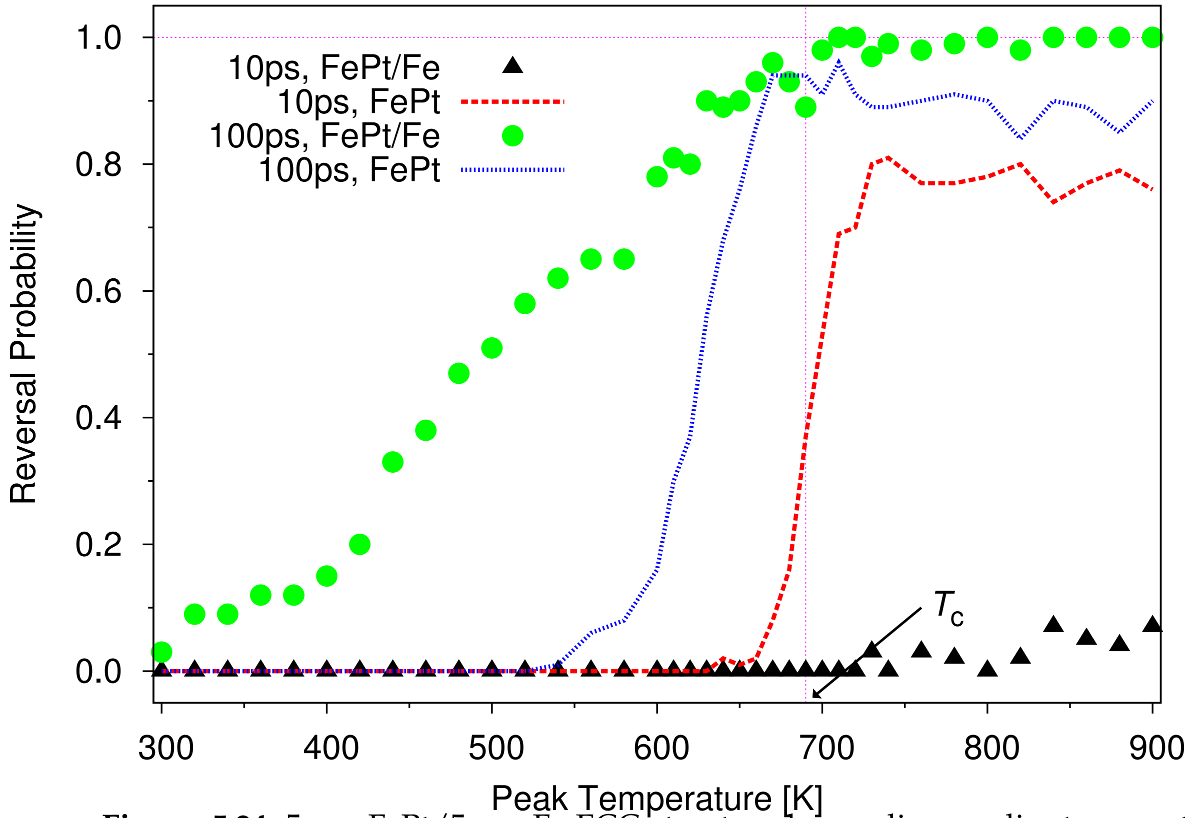

Figure. 5.24: 5 nm FePt/5 nm Fe ECC structured recording media: temperature dependent reversal probability at different cooling time.

To sum up, the ECC media has advantages in a field cooling process when the cooling time is longer, while it does not behaves better when the cooling time is shorter because of the longer thermal relaxation time of Fe, which makes harder to reverse Fe, and then the exchange coupling forbids the FePt to reverse and reduce the reversal probability.

5.4 Conclusion

An ECC material with a soft/hard bilayer structure has a lower coercivity comparing to the hard layer. The interface exchange coupling between the soft and hard layers plays an critical role in the reversal mode and also results in the reduction of coercivity. A weak interface exchange constant will result in a minimum system coercivity, rather than a very large one. This is due to a different reversal mode when the interface exchange is weak. The nucleation of the rotation of the magnetisation in the soft layer which then propagates into the hard layer is the main reason that reduces the coercivity. The thickness of the soft layer also decreases the coercivity. In a field cooling process, the ECC media has advantages when the cooling time is as long as 100ps, but disadvantages for a shorter cooling time. This is because of longer thermal relaxation time of the soft layer, which is harder to reverse itself and also the hard layer due to the interface exchange.

6. Conclusions

In this chapter, the results of previous chapters will be considered and also further research on the reversal processes of the magnetic recording media is also discussed.

Inter-granular exchange coupling between CoPt grains

Intergranular exchange coupling is an important factor in the design of current media, being introduced to partially counteract the effect of the demagnetising field. Since the grain size of magnetic recording particles is decreasing and it becomes harder to control the inter-granular exchange coupling, one approach is to totally decouple the magnetic grains with a very thick oxide spacer, and add a capping layer to uniformly control the exchange coupling. Therefore, the interface exchange coupling between the grains and the continuous capping layer has an essential effect on the magnetic properties of the system, as well as the thickness of the capping layer. A sharp decrease in coercivity is found for small value of interface exchange coupling leading to a minimum, after which the coercivity increases to a constant value. This is due to the nucleation and propagation of an in-plane domain wall which leads the reversal of CoPt grains for smaller exchange, while for larger exchange, this propagation of the domain wall is inhibited by the CoPt grains. For weak exchange coupling the coercivity is reduced, whereas for strong coupling the reversal mechanism tends toward coherent rotation and the coercivity consequently increase. In the meanwhile, the thickness of the capping layer will reduce the coercivity and thus to vary the thickness of the capping layer is also an effective way to control the system coercivity.

Another method to control the inter-granular exchange coupling is directly doping magnetic atoms into the spacer between recording grains. A Monte Carlo method was used to calculate the restoring torque and the exchange energy of a system with two constrained magnetic layers coupled by some free atoms within the spacer of the two layers, to find the exchange coupling increases with the density of the doping atoms and decreases with the spacer thickness. The temperature dependent exchange energy is also simulated, indicating the thermal fluctuation has a larger effect on the exchange energy especially for thicker spacer. Furthermore, an atomistic model is used to calculate the coercivity of a granular CoPt layer with doping atoms between the grains. The density of the doping atoms reduces the coercivity of the whole system if the anisotropy of the doping atoms is small. Therefore, controlling the density of doping magnetic atoms in the spacer between recording grains is also a way to control the exchange coupling between grains.

Field cooling process of magnetic recording grains

Heat assisted magnetic recording is a possible solution to the so-called trilemma problem in recording media. There are several crucial factors in HAMR which effect the reversal processes: the temperature, the applied field and the heating and cooling times. An atomistic model was used to simulate a single FePt grain to get the basic magnetic properties of this system, such as the hysteresis loop, the Curie temperature and the temperature dependent coercivity. Furthermore a multiple FePt grain system has also been studied during a cooling process. The effects of the peak temperature, the cooling rate, and the applied field have been investigated. However, in the field cooling process, it is found that the initial state is quite important. For further study, a semi-analytical approach was performed obtaining good agreement with the simulation results, and this proves the HAMR process is analogous to an ultra-fast cooling process which is controlled by the three factors mentioned previously. Both the simulation and numerical results give a good description of the reversal process and how the three elements effect the reversal process.

Finally a complete HAMR process is performed by using a whole atomistic model, to simulate a real HAMR heating and cooling process of multiple cording grains with grain size distribution. A writing head which has a laser with a Gaussian temperature and a uniform magnetic field is scanned over the grains. By choosing appropriate parameters of the laser temperature and the applied field value and also the distance between the laser and the field, when the head is moving as a certain speed, it was demonstrated that the HAMR writing is possible at for 5 nm grains at 0.7 Tb/in^2.

Exchange coupled composite media

Exchange coupled composite media with a soft/hard bilayer structure is an important recording media. Firstly, an atomistic model was used to simulate the reversal process of the soft/hard bilayers at constant temperatures. At zero temperature, the interface exchange coupling between the soft and hard layers plays an critical role in the reversal mode and also results in the reduction of coercivity. A constrained Monte Carlo method was also used to calculate the free energy, giving more details about the reversal mechanism. Furthermore, the soft layer thickness dependent coercivity was investigated, the increasing of the thickness also decreases the coercivity. Similar conclusion is obtained at room temperature, the small differences from the zero temperature results are due to the thermal effect.

Secondly, a HAMR heating and cooling process was performed on the exchange coupled composite media with a soft/hard bilayer structure, since it has a lower coercivity comparing to the hard layer, and also a higher Tc of the soft layer resulting a better thermal stability. In a field cooling process, the ECC media has advantages when the cooling time is as long as 100ps, but disadvantages for a shorter cooling time. This is due to the different reversal modes of the grains at different temperature. At a temperature higher than Tc, linear reversal dominates, which is ultra-fast. At a lower temperature, precessional rotation dominates, which takes longer time than the linear reversal. Therefore, for a longer time, heating up to Tc is not necessary, and ECC media has a higher reversal probability than the grains with only hard layer. For a time shorter than the thermal relaxation time, heating over Tc is required to guarantee that the linear reversal mode can switch the magnetisation. HAMR on ECC media with a high T_C soft layer relies on switching of the soft layer by precession. This is a relatively slow process, as a result of which it is successful for clloing time of around 100 ps, wherear a cooling time of 10 ps is insufficient to allow reversal. As a result, no large increase in data rate is possible with this design.

Further Prospects

Based on the calculation using the atomistic model, there are several further topics to work on following the current results. For the current model, a generic spin model is used to simulate the $L1_0$ phase FePt and CoPt. However, these two materials have more complicated structures and properties, such as the long range exchange coupling rather than the direct exchange coupling of the Heisenberg model. Furthermore, The interface exchange coupling has an important effect on the magnetic properties of multi-layer structures, so a detailed and accurate layered exchange constant calculation is needed, rather than the uniform exchange constant used currently. The atomistic model is able to use the parameters calculated from the ab-initial method to get a more accurate results, so the connection between atomistic modelling and ab-initial calculation is worthy to do in the future.

Papers and Presentations

Papers

"Control of the exchange coupling in granular CoPt/Co recording media", W. J. Fan, R. F. L. Evans, Y. Hancock, and R. W. Chantrell, Journal of Applied Physics, 109, 07B752 (2011).

"The Curie temperature distribution of FePt granular magnetic recording media", O. Hovorka, S. Devos, Q. Coopman, W. J. Fan, C. J. Aas, R. F. L. Evans, Xi Chen, G. Ju, and R. W. Chantrell, Applied Physics Letters, 101, 052406 (2012).

"Calculation of the thermoremanent magnetization induced by non-equilibrium cooling in the vicinity of the Curie point", R. F. L. Evans, W. J. Fan, and R. W. Chantrell, to be submitted to Physical Review Letters.

"Large Coercivity Reduction: Effect of Interface Coupling on Exchange Coupled Composite FePt/Fe Bilayers", W. J. Fan, R. F. L. Evans, and R. W. Chantrell, to be submitted to Applied Physics Letters.

"Atomistic spin model simulations of magnetic nanomaterials using VAMPIRE", R. F. L. Evans, W. J. Fan, P. Chureemart, T. A. Ostler, J. Barker, M. O. A. Ellis, and R. W. Chantrell, to be submitted to Physical Review B.

"Atomistic calculation of the thickness and temperature dependence of the inter grain exchange coupling in magnetic recording media", R. F. L. Evans, Q. Coopman, S. Devos, W. J. Fan, and R. W. Chantrell, to be submitted to Applied Physics Letters.

Presentations

"Atomic scale calculation of ultrafast processes", Wurzburg, Germany, EU FANTOMAS project Conference, 2010.4.

"Impact of exchange coupling on reversal processes of granular CoPt/Co bilayers", Stoos, Switzerland, EU FANTOMAS project conference, 2010.10.

"Control of the exchange coupling in granular CoPt/Co recording media", Atlanta, GA, USA, 55th Magnetism and Magnetic Materials Conference, 2010.11

"Atomistic simulation of magnetic reversal processes for heat assisted magnetic recording”, Vancouver, Canada, IEEE INTERMAG Conference, 2012. 5.

”Control of the exchange coupling in granular CoPt/Co recording media”, poster presentation, JSPS York-Tohoku Research Symposium, York, UK, 2011.6.

References

[1] W. J. Fan, E. F. L. Evans, Y. Hancock, and R. W. Chantrell. Control of the exchange coupling in granular CoPt/Co recording media. *Journal of Applied Physics*, 109:07B752, 2011.

[2] F. Michael. *Historical Beginnings of Theories of Electricity and Magnetism*. 1997.

[3] H. C. Oersted. *Selected Scientific Works of Hans Christian Oersted*. Princeton University Press, 1998.

[4] R. Skomski. *Simple Models of Magnetism*. Oxford University Press, Oxford, 2008.

[5] B. D. Cullity and C. D. Graham. *Introduction to Magnetic Materials*. Wiley, New Jersey, 2009.

[6] T. A. Ostler, R. F. L. Evans, and Chantrell. R. W. Crystallographically amorphous ferrimagnetic alloys: Comparing a localized atomistic spin model with experiments. *Physical Review B*, 84:024407, 2011.

[7] T. A. Ostler, J. Barker, R. F. L. Evans, Chantrell. R. W., U. Atxitia, O. Chubykalo-Fesenko, S. EI Moussaoui, L. Le Guyader, E. Mengotti, L. J. Heyderman, F. Nolting, A. Tsukamoto, A. Itoh, D. Afanasiev, B. Ivanov, A. M. Kalashnikova, K. Vahaplar, J. Mentink, A. Kirilyuk, Th. Rasing, and A. V. Kimel. Ultrafast heating as a sufficient stimulus for magnetization reversal in a ferrimagnet. *Nature Communications*, 3(666), 2012.

[8] H. Kronmuller and S. Parkin, editors. *Handbook of Magnetism and Advanced Magnetic Materials*. Wiley, 2007.

[9] R. F. L. Evans, R. W. Chantrell, U. Nowak, A. Lyberatos, and H. J. Richter. Thermally induced error: Density limit for magnetic data storage. *Applied Physics Letters*, 100:102402, 2012.

[10] W. F. Brown. *Micromagnetics*. Wiley, New York, 1963.

[11] W. Heisenberg. Zur theorie des ferromagnetismus. *Zeitschrift für Physik*, 49:619, 1928.

[12] W. Heitler and F. London. Wechselwirkung neutraler atome und homöopolare bindung nach der quantenmechanik. *Zeitschrift für Physik*, 44:455, 1927.

[13] L.D. Landau and E.M. Lifshitz. Theory of the dispersion of magnetic permeability in ferromagnetic bodies. *Physikalische Zeitschrift der Sowjetunion*, 8:153, 1935.

[14] T. L. Gilbert. A lagrangian formulation of the gyromagnetic equation of the magnetic field. *Physical Review*, 100:1243, 1955.

[15] N. Mo, J. Hohlfeld, M. ul Islam, C. S. Brown, E. Girt, P. Krivosik, W. Tong, A. Rebei, and C. E. Patton. Origins of the damping in perpendicular media: Three component ferromagnetic resonnance linewidth in co-cr-pt alloy films. *Applied Physics Letters*, 92:022506, 2008.

[16] M. L Schneider, Th. Gerrits, A. B. Kos, and T. J. Silva. Gyromagnetic damping and the role of spin-wave generation in pulsed inductive microwave magnetometry. *Applied Physics Letters*, 87(7):072509, 2005.

[17] W. F. Brown Jr. *Magnetics, IEEE Transactions on*, 15:1196, 1979.

[18] U. Nowak. *Thermally activated reversal in magnetic nanostructures. Annual Review of Computational Physics IX*. World Scientific, Singapore, 2001.

[19] W. F. Brown. Thermal flucturations of a single-domain particle. *Physics Review*, 130(5):1677–1686, 1963.

[20] O. N. Mryasov, U. Nowak, K. Y. Guslienko, and R. W. Chantrell. Temperature-dependent magnetic properties of FePt: Effective spin hamiltonian model. *Europhysics Letters*, 69(5):805–811, 2005.

[21] S Okamoto, N. Kikuchi, O. Kitakami, T. Miyazaki, Y. Shimada, and K. Fukamichi. Chemical-order-dependent magnetic anisotropy and exchange stiffness constant of fept (001) epitaxial films. *Physical Review B*, 66(2):024413, 2002.

[22] D. C. Crew, J. Kim, and K. Barmak. Interdiffusion in bilayer CoPt/Co films: potential for tailoring the magnetic exchange spring. *Journal of Magnetism and Magnetic Materials*, 233(3):257–273, 2001.

[23] A. Iserles. *A First Course in the Numerical Analysis of Differential Equations*. Cambridge University Press, Cambridge, 1996.

[24] L. M. Falicov, Daniel T. Pierce, S. D. Bader, R. Gronsky, Kristl B. Hathaway, Herbert J. Hopster, David N. Lambeth, S. S. P. Parkin, Gary Prinz, Myron Salamon, Ivan. K. Schuller, and R. H. Victora. Surface, interface, and thin-film magnetism. *Journal of Materials Research*, 5:1299, 1990.

[25] B. Heinrich and J.F. Cochran. Ultrathin metallic magnetic films: magnetic anisotropies and exchange interactions. *Advances in Physics*, 42(5), 1993.

[26] M. T. Johnson, P. J. H. Bloemen, F. J. A den Broeder, and J. J. de Veries. Magnetic anisotropy in metallic multilayers. *Reports on Progress in Physics*, 59:1409, 1996.

[27] U. Nowak, J. Heimel, T. Kleinefeld, and D. Weller. Domain dynamics of magnetic films with perpendicular anisotropy. *Physical Review B*, 56:8143–8148, 1997.

[28] M. H. Kryder, W. Messner, and L. R. Carley. Approaches to 10 Gbit/in^2 recording. *Journal of Applied Physics*, 79:4485, 1996.

[29] D. N. Lambeth, E. M. T. Velu, G. H. Bellesis, L. L. Lee, and D. E. Laughlin. Media for 10 Gbit/in^2 hard disk storage: Issues and status. *Journal of Applied Physics*, 79:4496, 1996.

[30] D. Goll. Magnetic properties of exchange-coupled $L1_0$-FePt/Fe composite elements. *Magnetics, IEEE Transactions on*, 44(11):3472–3475, 2008.

[31] D. Goll and A. Breitling. Coercivity of ledge-type $L1_0$-FePt/Fe nanocomposites with perpendicular magnetization. *Applied Physics Letters*, 94:052502, 2009.

[32] F. Casoli. Exchange-coupled FePt/Fe bilayers with perpendicular magnetization. *Magnetics, IEEE Transactions on*, 41:3877–3879, 2005.

[33] E. Goto, N. Hayashi, T. Miyashita, and K. Nakagawa. Magnetization and switching characteristics of composite thin magnetic films. *Journal of Applied Physics*, 36:2951, 1965.

[34] G. Asti, M. Solzi, Ghidini M., and F. M. Neri. Micromagnetic analysis of exchange-coupled hard-soft planar nanocomposites. *Physical Review B*, 69:174401, 2004.

[35] F. Garcia-Sanchez, O. Chubykalo-Fesenko, R. W. Chantrell, and K. Y. Guslienko. Exchange spring structures and coercivity reduction in FePt/FeRh bilayers: A comparison of multiscale and micromagnetic calculations. *Applied Physics Letters*, 87:122501, 2005.

[36] E. E. Fullerton, J. S. Jiang, C. H. Sowers, and S. D. Bader. Exchange-spring behavior in epitaxial hard/soft magnetic bilayers. *Physical Review B*, 58:12193–12200, 1998.

[37] R. H. Victora and X. Shen. Exchange coupled composite media for perpendicular magnetic recording. *Magnetics, IEEE Transactions on*, 41:2828–2833, 2005.

[38] N. Metropolis and S. Ulam. The monte carlo method. *Journal of the American Statistical Association*, 44(247):335–341, 1949.

[39] C. P. Robert and G. Casella. *Monte Carlo Statistical Methods (Second Edition)*. Springer-Verlag, New York, 2004.

[40] John S. Thomsen. Logical relations among the principles of statistical mechanics and thermodynamics. *Physics Review*, 91(5):1263–1266, 1953.

[41] G. Marsaglia. Choosing a point from the surface of a sphere. *Annals of Mathematical Statistics*, 43:645–646, 1972.

[42] K. Binder. Applications of monte carlo methods to statistical physics. *Reports on Progress in Physics*, 60(5):487–559, 1997.

[43] R. E. Rottmayer, S. Batra, D. Buechel, W. A. Challener, J. Hohlfeld, Y. Kubota, L. Li, B. Lu, C. Mihalcea, K. Mountfield, K. Pelhos, C. Peng, T. Rausch, M. A. Seigler, D. Weller, and X. M. Yang. Heat-assisted magnetic recording. *Magnetics, IEEE Transactions on*, 42(10):2417, 2006.

[44] M. H. Kryder, E. C. Gage, T. W. McDaniel, W. A. Challener, R. E. Rottmayer, G. Ju, Y. T. Hsia, and M. F. Erden. Heat assisted magnetic recording. *Proceedings of the IEEE*, 96(11):1810, 2008.

[45] W. A. Challener, C. Peng, A. V. Itagi, D. Karns, W. Peng, Y. Peng, X. M. Yang, X. Zhu, N. J. Gokemeijer, Y. T. Hsia, G. Ju, R. E. Rottmayer, and M. A. Seigler. Heat-assisted magnetic recording by a near-field transducer with efficient optical energy transfer. *Nature Photonics*, 3:220, 2009.

[46] L. Pan and D. B. Bogy. Heat-assisted magnetic recording. *Nature Photonics*, 3:189, 2009.

[47] D. A. Garanin. Fokker-planck and landau-lifshitz-bloch equations for classical ferromagnets. *Physical Review B*, 55(5):3050, 1997.

[48] D. A. Garanin and O. Chubykalo-Fesenko. Thermal flucturations and longitudinal relaxation of single-domian magnetic particles at elevated temperatures. *Physical Review B*, 70:212409, 2004.

[49] U. Nowak, O. N. Mryasov, R. Wieser, K. Guslienko, and R. W. Chantrell. Spin dynamics of magnetic nanoparticles: Beyond brown’s theory. *Physical Review B*, 72:172410, 2005.

[50] O. Chubykalo-Fesenko, U. Nowak, R. W. Chantrell, and D. A. Garanin. Dynamic approach for micromagnetics close to the curie temperature. *Physical Review B*, 74:094436, 2006.

[51] U. Atxitia, O. Chubykalo-Fesenko, N. Kazansseva, D. Hinzke, U. Nowak, and R. W. Chantrell. Micormagnetic modeling of laser-induced magnetization dynamics using the landau-lifshitz-bloch equation. *Applied Physics Letters*, 91:232507, 2007.

[52] N. Kazantseva, D. Hinzke, R. W. Chantrell, and U. Nowak. Linear and elliptical magnetization reversal close to the curie temperature. *Europhysics Letters*, 86(2):27006, 2009.

[53] J. Barker, R. F. L. Evans, R. W. Chantrell, and U. Nowak. Atomistic spin model simulation of magnetic reversal modes near the curie point. *Applied Physics Letters*, 97:192504, 2010.

[54] C. Antoniak, M. Spasova, A. Trunova, K. Fauth, M. Farle, and H. Wende. Correlation of magnetic moments and local structure of fept nanoparticles. *Journal of Physics: Conference Series*, 190:012118, 2009.

[55] E. C. Stoner and E. P. Wohlfarth. A mechanism of magnetic hysteresis of heterogeneous alloys. *Magnetics, IEEE Transactions on*, 27(4):3475, 1991.

[56] R. W. Chantrell and E. P. Wohlfarth. Rate dependence of the field-cooled magnetisation of a fine particle system. *Physica Status Solidi*, 91:619–626, 1985.

[57] R. F. L. Evans, W. J. Fan, and R. W. Chantrell. Calculation of the thermoremanent magnetization induced by non-equilibrium cooling in the vicinity of the curie point, to be submitted.

[58] D. Suess, T. Schrefl, S. Fahler, M. Kirschner, G. Hrkac, F. dorfbauer, and J. Fidler. Exchange spring media for perpendicular recording. *Applied Physics Letters*, 87:012504, 2005.

[59] J. P. Wang, W. Shen, and J. Bai. Exchange coupled composite media for perpendicular magnetic recording. *Magnetics, IEEE Transactions on*, 41(10):3181, 2005.

[60] J. P. Wang, W. Shen, and S. Y. Hong. Fabreication and characterization of exchange coupled composite media. *Magnetics, IEEE Transactions on*, 43(2):682, 2007.

[61] H. Zeng, J. Li, J. P. Liu, Z. L. Wang, and S. Sun. Exchange-coupled nanocomposite magnets by nanoparticle self-assembly. *Nature*, 420:395, 2002.

[62] T. J. Zhou, B. C. Lim, and B. Liu. Anisotropy graded fept-tio2 nanocomposite thin films with small grain size. *Applied Physics Letters*, 94:152505, 2009.

[63] F. Wang, X. Xu, Y. Liang, J. Zhang, and H. Wu. FeAu/FePt exchange-spring media fabricated by magnetron sputtering and postannealing. *Applied Physics Letters*, 95:022516, 2009.

[64] A. Breitling, T. Bublat, and D. Goll. Exchange-couled $L1_0$-FePt/Fe composite patterns with perpendicular magnetization. *Physica Status Solidi*, RRL 3(5):130–132, 2009.

[65] H. Wang, H. Zhao, T. Rahman, Y. Isowaki, Y. Kamata, T. Maeda, H. Hieda, A. Kikitsu, and J. P. Wang. Fabreication and characterization of fept exchange coupled composite and graded bit patterned media. *Magnetics, IEEE Transactions on*, 49(2):707, 2013.

[66] R. H. Victora and X. Shen. Exchange coupled composite media. *Proceedings of the IEEE*, 96(11):1799, 2008.

[67] A. Y. Dobin and H. J. Richter. Domain wall assisted magnetic recording. *Journal of Applied Physics*, 101:09K108, 2007.

[68] B. Livshitz, A. Inomata, H. N. Bertram, and V. Lomakin. Precessional reversal in exchange-coupled composite magnetic elements. *Applied Physics Letters*, 91:182502, 2007.

[69] Z. Xu, S. M. Zhou, J. J. Ge, J. Du, and L. Sun. Magnetization reversal mechanism of perpendicularly exchange-coupled composite $L1_0$-FePt/CoCrPt bilayers. *Journal of Appled Physics*, 105:123903, 2009.

[70] E. Girt, A. Y. Dobin, B. Valcu, H. J. Richter, X. Wu, and T. P. Nolan. Experimental evidence of domian wall assisted switching in composite media. *Magnetics, IEEE Transactions on*, 43(6):2166, 2007.

[71] T. Deakin and K. O'Grady. Magnetic characterization of exchange-coupled composite media. *Journal of Applied Physics*, 103:07F503, 2008.

[72] H. Kronmuller and D. Goll. Micromagnetic theory of the pinning of domain walls at phase boundaries. *Physica B*, 319:122–126, 2002.